



Faculty of Technology

Evaluation of Constraint Effects on the T_0 Temperature of Miniature SE(N)T Specimens

Timo Veijola

Mechanical Engineering

Master's thesis

December 2022

TIIVISTELMÄ

Constraint-efektin vaikutusten arvio T_0 lämpötilaan miniatyyri SE(N)T murtovetosauvoilla

Timo Veijola

Oulun yliopisto, konetekniikan tutkinto-ohjelma

Diplomityö 2022, 129 s. + 6 liitettä

Työn ohjaajat: Sakari Pallaspuro (Oulun yliopisto), Sebastian Lindqvist (VTT)

Tässä diplomityössä selvitetään miniatyyrikokoisten SE(N)T tyyppin murtovetosauvojen sitkeysarvoja käyttäen ASTM E1921 standardissa kuvattua Master Curve -menetelmää. Työn JRQ-nimetystä ASTM A533B materiaalihiosta aikaisemmin teetettyjen kokeiden tuloksiin vertailemalla tutkitaan koon ja erityisesti constraint-efektin vaikutusta murtositkeystuloksiin.

Kokeellinen osuus koostuu 12 a/W 0.5 ja 11 a/W 0.2 SE(N)T-murtovetosauvoista, joiden välillä verrataan constraint-vaikutusta T_0 lämpötilaan. Mittausdatasta voiman ja CMOD lukemien välille sovitetaan käyrä, jota analysoimalla johdetaan J , K_{Jc} ja T_0 lämpö Master Curve -menetelmällä. Syväsröisen sauvan T_0 lämpötilaksi saatiin -54 °C, mikä on hauras kyseiselle materiaalille. Matalasäröisen sauvan T_0 lämpötila on sensurointimäärän mukaan -113 °C sensuroimattomalle sarjalle ja -98 °C sensuroidulle sarjalle. Tulos on sitkeämpi kuin vertailuaineisto samalle materiaalille. Ero T_0 lämpötilassa heijastaa sitkeyden muutosta, joka oli sauvatyypin välillä 44 °C. Constraint-ilmion Q-parametri johdettiin Abacus CAE FEM -mallin ja HRR-kentän avulla, minkä tulosten perusteella constraint-vaikutuksen ero sauvatyypin välillä oli 29 °C. Ero mallin ja kokeiden välillä on virhemarginaalin sisällä ja sauvatyypin todetaan olevan herkkä constraint-muutokselle särönsyvyyden suhteen. Koon vaikutusta sitkeysarvojen tilastolliseen hajoamaan ei pystytty määrittämään pienen datamäärän vuoksi. Mittausten luotettavuutta arvioitiin osittaisderivointiin pohjautuvan menetelmän ja Sobolin indeksien kautta ja tuloksia täydennettiin mikroskopiolla ja kovuusmittauksilla.

Asiasanat: JRQ-referenssiteräs, SE(N)T, T_0 lämpötila, Constraint, Master Curve

ABSTRACT

Evaluation of Constraint Effects on the T_0 Temperature of Miniature SE(N)T Specimens

Timo Veijola

University of Oulu, Degree Programme of Mechanical Engineering

Master's thesis 2022, 129 pp. + 6 Appendixes

Supervisors: Sakari Pallaspuro (University of Oulu), Sebastian Lindqvist (VTT)

The thesis explores the fracture toughness values derived using miniature SE(N)T specimens using the Master Curve method as described in the standard ASTM E1921. By comparing the results to previous experiments conducted on the ASTM A533B Class 1 pressure vessel steel designated JRQ, the effects of size and especially the constrain effect on fracture toughness are investigated.

The experimental section consists of 12 a/W 0.5 and 11 a/W 0.2 crack depth SE(N)T tests. The effect of constraint on the T_0 temperature is investigated by comparing the toughness values between the two crack depths. The CMOD and force are measured, and the area under the graph they form is analyzed to derive J-integral, K_{Jc} and the T_0 temperature using the Master Curve method. The a/W 0.5 specimens produced a T_0 temperature of -54 °C which is on the brittle side for the reference material. Depending on the level of censorship the 0.2 a/W specimens had an uncensored T_0 temperature of -113 °C and a censored T_0 temperature of -98 °C. Both are tougher than the comparison values used. The difference in T_0 temperature reflects a change in toughness which was 44 between the specimen types. The constraint effect was evaluated with an Abaqus CAE FEM model from which Q-parameters were derived using the HRR field as a reference. The modelled difference between the specimen types was 29 °C which is within the margin of error of the experimental results. The SE(N)T specimens were observed to be sensitive to constraint effects with respect to the crack depth. The effect of specimen size could not be evaluated due to the limited number of experiments. The reliability of the measurement results was estimated using a partial derivatives method and Sobol's indices. The results were supplemented with microscopy and hardness analysis.

Keywords: JRQ reference steel, SE(N)T, T_0 temperature, Constraint, Master Curve

FOREWORD

This thesis work was conducted as a part of the larger Advanced materials characterization for structural integrity assesment (AMOS) project. One of the main goals of the project is to reduce structural integrity related uncertainties by providing data for nuclear surveillace programs. Miniature test tehniques are investigated in pursuit of this goal and the thesis focuses on downscaled SE(N)T specimens. Especially constraint effects on these reduced scales were studied.

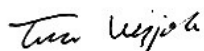
The work was started in April of 2022, and during the eight months it took to complete, nuclear safety reached the headlines due to the war in ukraine and the issues with Olkiluoto 3. The topic of nuclear safety seems now more relevant than ever. The topic was ideal for me, as it combined my major, materials science and engineering, to another focus of my optional courses, strength of materials. The empirical nature of the thesis complimented my curiosity towards practical work. Another goal of the AMOS project is to educate new experts in the field of fatigue and fracture mechanics, and the thesis work has shown me, how much I still have to learn.

I would like to extrend my gratitude to the people of BA4510 who assisted me in many ways, the team leader Tommi Seppänen, who often solved administrative problems before I had even asked, and Juha Kuutti for his help with Abaqus modelling.

Finally, aspecial thank you to my supervisors Sebastian Lindqvist and Sakari Pallaspuro for the support and insight they provided.

In conclusion: ”Työ opetti tekijälleen paljon väsymisestä ja murtumisesta.”

Oulu 5.12.2022



Author

TABLE OF CONTENTS

TIIVISTELMÄ

ABSTRACT

FOREWORD

TABLE OF CONTENTS

SYMBOLS AND ABBREVIATIONS

| | |
|---|----|
| 1 BACKGROUND AND MOTIVATION FOR THE THESIS RESEARCH | 10 |
| 2 LITERATURE REVIEW | 14 |
| 2.1 Fracture Mechanics and fracture | 14 |
| 2.1.1 Plasticity and dislocations | 15 |
| 2.1.2 Concentration of stress | 17 |
| 2.2 Fracture mechanisms | 20 |
| 2.2.1 Void nucleation and coalescence | 21 |
| 2.2.2 Brittle cleavage fracture | 22 |
| 2.3 The Master Curve method | 24 |
| 3 CONSTRAINT | 29 |
| 3.1 Factors affecting constraint | 31 |
| 3.2 Quantifying constraint | 32 |
| 3.2.1 Elastic T-Stress | 33 |
| 3.2.2 Q-parameter | 35 |
| 4 DESIGN OF THE SE(N)T SPECIMEN | 37 |
| 4.1 General SE(N)T specimen dimensions | 37 |
| 4.2 Crack and knife edge depth | 38 |
| 4.3 Knife edge geometry | 43 |
| 4.4 Side grooves | 44 |
| 5 MATERIALS AND METHODS | 45 |
| 5.1 Test material | 45 |
| 5.1.1 Hardness measurements | 47 |
| 5.1.2 Material composition | 48 |
| 5.1.3 Material strength | 48 |
| 5.2 Sample detachment | 53 |
| 5.2.1 Naming convention | 55 |
| 5.2.2 Pre-cracking | 55 |

| | |
|--|-----|
| 5.2.3 Side grooving..... | 55 |
| 5.3 Test equipment..... | 56 |
| 5.3.1 Load cell..... | 56 |
| 5.3.2 Clamping..... | 56 |
| 5.3.3 Temperature measurement and control..... | 58 |
| 5.3.4 Procedure followed..... | 61 |
| 5.4 Qualification requirements..... | 62 |
| 5.4.1 Screening criterion..... | 62 |
| 5.4.2 Pre-crack qualification..... | 62 |
| 5.4.3 Quasistatic load-rate qualification..... | 63 |
| 5.5 Fracture toughness calculations..... | 63 |
| 5.5.1 Derivation of the T_0 temperature..... | 68 |
| 5.5.2 Master curve graphs..... | 68 |
| 5.6 Abaqus CAE..... | 69 |
| 5.6.1 Material model..... | 70 |
| 5.6.2 Features, load, and constraint..... | 71 |
| 5.6.3 Mesh..... | 73 |
| 5.7 Result uncertainty evaluation..... | 74 |
| 5.7.1 Measurement uncertainty..... | 75 |
| 5.7.2 Global sensitivity analysis..... | 81 |
| 5.8 Post experiment inspections..... | 83 |
| 6 RESULTS & DISCUSSION..... | 84 |
| 6.1 Results..... | 84 |
| 6.1.1 HV10 hardness results..... | 84 |
| 6.1.2 Microstructural characterization..... | 85 |
| 6.1.3 Fractography..... | 88 |
| 6.1.4 Uncertainty calculation results..... | 96 |
| 6.1.5 Sobols indices..... | 97 |
| 6.1.6 Experimental results..... | 97 |
| 6.1.7 High Constraint HC-Series..... | 98 |
| 6.1.8 Low Constraint LC-Series..... | 99 |
| 6.1.9 Abaqus model results..... | 101 |
| 6.2 Comparison to previous results..... | 107 |
| 6.3 Discussion..... | 109 |
| 7 CONCLUSION..... | 120 |
| 8 REFERENCES..... | 122 |

APPENDIXES:

Appendix 1 Technical drawings and instructions

Appendix 2 MATLAB Code

Appendix 3 Uncertainty variance components

Appendix 4 Python script used for the sensitivity analysis

Appendix 5 CMOD-Force graphs for all the samples

Appendix 6 Calculation values

SYMBOLS AND ABBREVIATIONS

| | |
|--------------|--|
| A | Material factor for determining the T_0 shift through the T-stress |
| A_e | Elastic area under the CMOD_Force graph |
| A_p | Plastic area under the CMOD-Force graph |
| Area | Area under the CMOD-Force graph |
| B | Width of the specimen/crack front |
| B_0 | A chosen reference width, usually one inch (1T) |
| B_N | Notched width of the specimen |
| C_0 | Elastic slope reciprocal |
| C_2 | Material coefficient |
| $CMOD_{max}$ | The largest CMOD opening value |
| E | Young's modulus |
| F | Load/Force |
| F_m | Load at CMOD maximum |
| G | Shear modulus |
| HV | Hardness (Vickers) |
| I_n | Strain hardening related Q-parameter constant |
| J | J-integral |
| J_c | Elastic-plastic J-integral at the onset of cleavage fracture |
| J_e | Elastic portion of the J-integral at the onset of cleavage fracture |
| J_p | Plastic portion of J-integral at the onset of cleavage fracture |
| K | Stress intensity factor |
| K_0 | The normalizing fracture toughness corresponding to a 63.2% cumulative failure probability |
| K_e | Elastic stress intensity factor |
| K_I | Mode I loading stress intensity factor |
| K_{Ic} | Fracture toughness of a material under mode I loading (ASTM E399) |
| K_{Jc} | Elastic-plastic equivalent stress intensity factor derived from the J_c integral at the onset of cleavage fracture |
| K_m | The lower limit fracture toughness |
| N | The number of initiators |
| \bar{N} | The mean number of initiators |
| Nu | Number of uncensored specimens |

| | |
|--------------------|--|
| P | Three point bending force |
| P_f | The probability of failure |
| P_N | The probability of having N initiators in a sample |
| $\text{Pr}\{I\}$ | The probability of cleavage initiation |
| $\text{Pr}\{V/O\}$ | The conditional probability that no previous initiation has taken place |
| Q | Q-parameter |
| Q_{ref} | Reference Q-parameter value derived from a C(T) specimen |
| S | Support distance in three-point bending |
| T | Temperature |
| T_{corr} | A correction factor used in the estimation of Q-parameter effect on the T_0 temperature |
| T_s | T stress, a uniform stress in the crack growth direction |
| T_0 | Fracture toughness reference temperature, where median K_{Jc} is 100 $\text{MPa}\sqrt{\text{m}}$ |
| W | Thickness of the specimen |
| \varnothing_s | Thread diameter |
| | |
| a | Crack length or half of the crack length depending on specimen |
| a_0 | Pre-crack measured average length used as initial crack length |
| a_1 | Pre-crack length |
| a_j | Crack length with summation index |
| a/W | Crack length to specimen thickness ratio |
| b | Crack width |
| b_0 | Remaining initial ligament length |
| b_V | Burger's vector |
| d_s | Thread distance from crack center plane |
| f | Geometric factor related to the stress intensity factor |
| l | The specimen length |
| n | Number of specimens or experiments |
| n_{RO} | Ramberg-Osgood strain hardening exponent |
| pr | Particle radius |
| p | Polynomial coefficient for the fir function |
| \bar{q} | Mean of measured values |
| q_j | Indexed measured observation |

| | |
|--------------------|--|
| q_k | Measured observation' |
| r | Distance in front of the crack tip |
| r_p | Plastic zone radius at the crack tip |
| $s(\bar{q})$ | Experimental standard deviation |
| ν | Poisson's ratio |
| νT | Stress in the z direction in relation to the T_s stress. |
| α' | Coefficient for the KTH stress model |
| α_c | Coefficient between 0.14 and 0.33 |
| α_{RO} | Ramberg-Osgood yield offset coefficient |
| $\alpha\Delta T$ | The thermal expansion coefficient |
| β' | Coefficient for the KTH stress model |
| β_{uc} | Sample size uncertainty factor |
| β_x | Biaxiality ratio |
| γ | Glide |
| γ' | KTH model coefficient |
| γ_{lld} | Coefficient for the plastic area load line correction |
| δ | Crack opening displacement |
| $\Delta\sigma_d$ | Dislocation stress |
| Δl | Change in overall specimen length |
| ΔT_0 | Shift in T_0 temperature |
| ΔT_s | Change in T-stress conditions |
| ε | Strain |
| ε_1 | Maximum remote normal strain |
| ε_p | Plastic strain |
| ε_{ys} | Strain at material yield |
| η_{CMOD} | Eta factor for CMOD plastic correction |
| θ | Angular direction in front of the crack tip |
| ρ_r | Crack tip curvature |
| μ | Shear modulus |
| σ | Stress |
| σ_{1-3} | Principal normal stresses |
| σ_A | Crack tip stress |
| σ_c | Critical interphase cohesion stress |
| σ_e | Effective von Mises stress |

| | |
|---------------------------------------|---|
| σ_{flow} | Flow stress of the material |
| σ_{ij} | Stress in the i-j direction |
| $\sigma_{yy\text{FEA}}$ | Actual stress in the crack opening y direction from a FEM model |
| $\sigma_{yy\text{HRR}}$ | The HRR reference stress in the crack opening y direction |
| σ_m | Mean hydrostatic stress |
| σ_{meas} | Measurement standard uncertainty |
| σ_{stdev} | Standard deviation of the T_0 margin uncertainty |
| σ_{ys} | Yield strength |
| $\tilde{\sigma}_{ij}(n_{RO}, \theta)$ | An angular dependence constant for the Q-parameter |
| τ | Shear |
| | |
| ANOVA | Analysis of Variance |
| ASTM | American Society for Testing and Materials |
| BSI | British Standards Institution |
| BCC | Body Centered Cubic lattice |
| CMOD | Crack Mouth Opening Displacement |
| EBSD | Electron Backscatter Diffraction |
| EDM | Electric Discharge Machining |
| HAZ | Heat Affected Zone |
| HRR | Hutchinson-Rice-Rosengren model/field |
| HV10 | Vicker's hardness measured with a force equivalent of 10 kilograms |
| IAEA | International Atomic Energy Agency |
| KTH | Kungliga Tekniska högskolan, KTH Royal Institute of Technology |
| OES | Optical Emission Spectrometry |
| SEB | Single Edge (notched) Bend specimen |
| SEM | Scanning Electron Microscope |
| SE(N)T | Single Edge (Notched) Tensile specimen |
| VTT | Teknologian tutkimuskeskus VTT Oy, Technical Research Centre of Finland |
| STUK | Säteilyturvakeskus, Nuclear and Radiation Safety Authority of Finland |

1 BACKGROUND AND MOTIVATION FOR THE THESIS RESEARCH

Finland aims to be carbon neutral by 2035 (Paavola et al., 2021; Paloneva & Takamäki, 2021). Electricity consumption is predicted to rise heavily if carbon neutrality is to be met, and nuclear power plays a major role in the transition away from fossil fuels (Paloneva & Takamäki, 2021). There are four energy producing nuclear power plants operating in Finland with a fifth expected to join power production in 2022 (Työ- ja Elinkeinoministeriö, 2022). The extension of service lives for the nuclear power plants built from the late 1970's to early 1980's is suggested as a means towards achieving carbon neutrality. (Paloneva & Takamäki, 2021)

One factor limiting the lifespans is the accumulation of wear and fatigue in the form of cracks and other faults. Failure of a critical component is not an option as the harms of a nuclear accident can be extremely severe reaching international scale. As a consequence, the International Atomic Energy Agency [IAEA] technical safety principle states: *“take all reasonably practicable measures to prevent accidents in nuclear installations and to mitigate their consequences should they occur”* (Petrangeli, 2020 p. 117, 249-260) What is reasonable is determined through research and different standards, and in the case of Finland, the Finnish nuclear safety legislation appoints the Radiation and Nuclear Safety Authority [STUK] to set compliance requirements with the Nuclear Energy Act (Ydinenergialaki, 2021). STUK specifies that a brittle fracture analysis is conducted

“on the most stressed ferritic steel parts of the nuclear power plant's Safety Class 1 pressure equipment. Most important are the core area of the reactor pressure vessel, its largest pipe nozzles and the flanged joint of its head. Other possible items requiring a brittle fracture analysis are the secondary side of a pressurised [sic] water reactor plant's steam generator, the steel containment, and the shafts and flywheels of the main circulating pumps.” (Säteilyturvakeskus, 2020.)

The chosen method for the brittle analysis is fracture mechanics and comparison of the stress intensity factor K_I to the material fracture toughness K_{Ic} determined through suitable standards listed in the STUK Guide YVL E.4 (Säteilyturvakeskus, 2020).

Much of the fracture data on which the service life calculations are based on, are produced using bending type specimens. Large datasets for relevant materials in these configurations can be found, for example, in the monograph by Wallin (2011) and his publications preceding it. Current test methods are also primarily focused on highly constrained specimens as their behavior is less random and the literature around them more comprehensive. This however may lead to over conservative maintenance and monitoring programs of nuclear power plants. Too stringent test conditions are unlikely to reflect real-world applications where the crack geometries are more diverse and almost never under perfectly perpendicular stress fields. Setting toughness estimates based on these results can lead to premature, costly maintenance or even decommissioning of components where there is still lifetime left. (Ruggieri, 2017; Sarzosa et al., 2018) A more realistic low-constraint test regime is needed to determine new limits on allowable fault sizes, which are more applicable to the actual operational life expectancy of reactors.

This thesis explores the fracture toughness values of an IAEA nuclear correlation material A533B Class 1 pressure vessel steel produced by less conservative Single Edge (Notched) Tensile (SE(N)T) specimens and evaluates the effect of constraint on the T_0 temperature representing the magnitude of the material's toughness. The effect of constraint is studied through the use of a relatively high testing temperature resulting in more plasticity, -85 °C, and two crack depth- sample thickness ratios (a_0/W), 0.5 representing higher and 0.2 lower constraint conditions.

The high-energy neutron radiation in nuclear reactors proposes a unique challenge from a fracture mechanics perspective. The neutrons collide with steel's crystal lattice with sufficient energy to cause radiation embrittlement. This transits the T_0 temperature, and the exact shift is required to be determined through empirical experimentation. (Säteilyturvakeskus, 2020) The rarity of operationally radiated reactor material increases the difficulty of surveillance through experimentation and miniature test cases are needed

to conserve the scarce reference material. For safety reasons, it is also beneficial to handle smaller amounts of radioactive material.

The SE(N)T specimens tested as a part of this thesis are not radiated, but the melt that produced the steel described in the report by Brumovsky et al. (2001) is used as a reference material for radiated samples. The specimens have a miniature 10 mm sided square cross section in contrast to the standard one-inch (1T) reference thickness. The absolute effect the sample size has on the T_0 temperature is not deduced from these tests, rather, the applicability of theory on miniaturized specimens is assessed. The data produced can nevertheless be used for future research quantifying the effect specimen size has on the T_0 temperature and the variance of measurement results. In addition, previous results from bend specimens for the same material are used as a point of reference for the T_0 temperature. The measurement and method related uncertainties in the results are quantified using a partial derivatives method and a global sensitivity analysis. Relevant literature is reviewed concerning the Master Curve method, constraint, metallography, fracture mechanics, and previous studies around the same topics. A cursory glance at the tests performed is presented below in Table 1.

Table 1 Test series and their differences

| Series | Temperature [°C] | Number of specimens | a₀/W ratio | Load rate [mm/min] | Type |
|-----------------------|-----------------------------|--------------------------------|------------------------------|-------------------------------|--|
| LC-Calibration | - 85 | 3 | 0.2 | 0.1-0.2 | 10 x 10 mm ² SE(N)T BN 8.5 mm |
| HC-Calibration | - 85 | 2 | 0.5 | 0.1-0.2 | 10 x 10 mm ² SE(N)T BN 8.5 mm |
| HC | - 85 | 10 | 0.5 | 2 | 10 x 10 mm ² SE(N)T BN 8.5 mm |
| LC | - 85 | 9 | 0.2 | 2 | 10 x 10 mm ² SE(N)T BN 8.5 mm |

2 LITERATURE REVIEW

To form the foundation of the thesis research, theoretical background explaining the fracture phenomena is explored. Selected highlights from literature relevant to the design of the thesis experiments and the analysis of their results are presented below. Emphasis is placed on the metallurgical aspect of the fracture process, the statistical nature of fracture initiation sites, and the Master Curve method. Finally, a definition for constraint is formulated through the restriction of material flow and the corresponding stress triaxiality which follows. The SE(N)T specimens for the thesis research are then designed based on the information and standards reviewed in the following sections.

2.1 Fracture Mechanics and fracture

Fracture mechanics lays the foundation for almost all the relevant theories in this thesis. It is a relatively new field, with research taking off after the second world war following high-profile incidents such as the sinking of Liberty ships, and the crashing of early Comet- jet planes (Ikonen & Kantola, 1991; Anderson, 2005; Krishnaswamy, 2008; Wallin, 2011) It strives to find the connection between defects and fractures, quantify the phenomena behind fracturing events and discover mathematical formula describing the laws behind them. Combining fracture mechanics with other engineering disciplines allows the determination of conditions that lead to failure of components. (Ikonen & Kantola, 1991) In practice, fracture mechanics is used to scale structures to keep any stresses below critical loads which would lead to fracture growth for any presumed existing fault sizes (Ikonen & Kantola, 1991 p.236). Challenges to the practical approach arise from the unknown location and size of faults, difficult determination of actual stress states, and the stochastic nature of fracture initiation (Ikonen & Kantola, 1991 p. 235-237).

To fracture material, a number of bonds that hold its structure together need to be broken. Metal atoms stay together in the lattice through the Coulombic attraction between their positively charged cores and shared electron cloud. These bonds get weaker as the electron sea density decreases, for example through increased interatomic separation.

(Rohrer, 2001) Stress can stretch the distance between the atoms and displacing the atoms from their resting state introduces elastic energy. If this elastic energy created is greater than the lattice enthalpy, it is energetically advantageous for the material to form new surfaces through which elastic energy can be released. This new surface can be understood as a newly formed crack face. (Ikonen & Kantola, 1991)

Griffith's (1921) original model states, that if the surface energy of the crack is overcome by the elastic energy change due to incremental crack growth, the crack will propagate (Anderson, 2005). Transferring this mechanism to a macroscopic scale has proven difficult and traditional continuum models fail to take account effects of size and variable stress conditions as each lath and grain in metal can have different stress and strain fields. (Wallin, 2011 p.115-129)

2.1.1 Plasticity and dislocations

Steel deforms plastically through the movement of dislocations by slip, and the restriction of their movement increases the yield strength. Dislocation lines can be considered as the edge of an extra half plane in the atomic lattice. Breaking of atomic bonds along the movement of this line can happen one at a time instead of the whole plane shearing, lowering the energy requirements. (Hertzberg, 1976 p.43) Plastic deformation also absorbs energy through the movement and creation of dislocations allowing for increased toughness. Scaling down sample size does not directly increase the toughness through dislocation interactions, but it should be noted that at sample scales of $< 100 \mu\text{m}$ the dislocation interaction mechanisms would be affected, and toughness would be altered. (Uchic et al., 2004; Kaufmann, 2011)

The Body Centered Cubic, (BCC), lattice has 48 different glide systems due to the three types of planes with minimal, almost equal, packing densities. (Kaufmann, 2011) The interaction between dislocations can be observed in tensile tests through strain hardening. Before a material deforms plastically, it needs to exhaust its elastic strain. (Hertzberg, 1976) This can be seen in the transition from a linear to a curved stress-strain response in a tensile test, Figure 1. When the stress reaches the critical yield level in the weakest part of the specimen, it deforms locally. This local deformation will result in a lowered cross-

sectional area and hence higher stress. Instead of focusing all remaining deformation there, the material hardens, and the process of localized deformation transfers to the now newly weakest section along the gauge length.

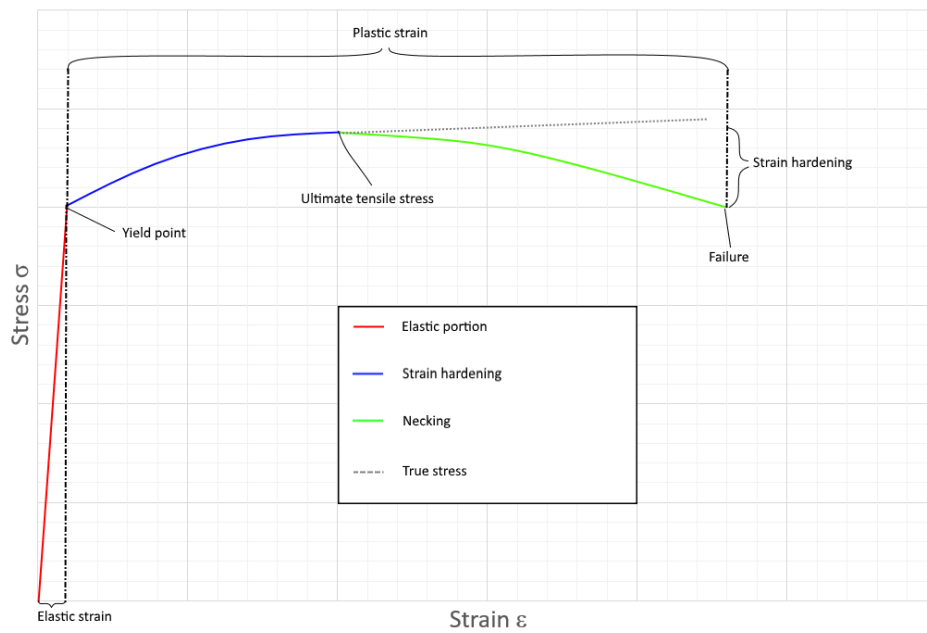


Figure 1 A typical Stress-Strain curve for a tensile test with highlighted elastic, plastic, and necking regions.

The hardening rate is strongly related to the creation of dislocations and their activation (Kaufmann, 2011), and as such, is not constant for the same material after different treatments. A way of modeling the strain hardening is through the Ramberg-Osgood relation, (1),

$$\frac{\varepsilon}{\varepsilon_{ys}} = \frac{\sigma}{\sigma_{ys}} + \alpha_{RO} \left(\frac{\sigma}{\sigma_{ys}} \right)^{n_{RO}} \quad (1)$$

where ε is strain,
 ε_{ys} is the strain at material yield,
 σ is stress,
 σ_{ys} is the material yield strength,

α_{RO} is the Ramberg-Osgood yield offset coefficient, and
 n_{RO} is the Ramberg-Osgood strain hardening exponent.

The first term provides the linear elastic response and the second a non-linear plastic approximation.(Kanninen & Popelar, 1985 p.299.) A different formulation of this equation is used in section 5.1.3 for the Abaqus material model.

As this process continues the material further hardens and the cross section decreases uniformly on a macroscopic scale as deformation is a constant volume process. At some point the strain hardening can no longer resist the increase in stress and the n^{th} local deformation is unable to harden enough to stop further plastic deformation. From this point onwards the region begins to neck as the elongation concentrates in it forcing the region to shrink in cross sectional area. (Hertzberg, 1976.) This can be seen in the lowered engineering stress required to increase the strain in Figure 1, and as the stresses are focused on a specific locus it becomes susceptible to failure.

In addition, a triaxial stress state rises in the area adjacent to the necked region due to Poisson's effect. The necked region under higher stresses compared to its surroundings tries to draft in adjacent material to accommodate the elongation, which results in radial and transverse stresses. These stresses need to be accounted for in the increased axial stress to induce further plastic flow facilitating new deformation and constrain the material plastically. (Hertzberg, 1976) The relation of stress triaxiality, Poisson's effect, and restricted material flow is explored further in section 3.

2.1.2 Concentration of stress

The stresses that force atoms apart and lead to fracture are concentrated by certain geometries, especially by sharp crack tips. Griffith's original model (2-5, example for an elliptical crack in an infinite plate under plane stress conditions)

$$\sigma_A = \sigma \left(1 + 2 \sqrt{\frac{a}{\rho}} \right) \quad (2)$$

$$\rho = \frac{b^2}{a} \quad (3)$$

$$\sigma_A = \sigma \left(1 + 2 \left| \frac{a}{b} \right| \right) \quad (4)$$

$$a \gg b, \sigma_A = 2\sigma \sqrt{\frac{a}{\rho_r}} \quad (5)$$

where a is the crack length,
 b is the crack width,
 ρ_r is the crack tip curvature, and
 σ_A is the crack tip stress,

highlights the increase in stress as a defect becomes sharper, but falls short for the plastic deformation these large stresses induce in steel (Anderson, 2005). As the crack tip radius decreases, the stress trends towards infinity, as curvature is the denominator in formulas (2) to (5). No material can withstand the infinite stresses proposed by the model, and any loading would cause breakage. In reality, the shared electron cloud of steel allows for malleability and the crack tip blunts.

For the most important loading modes I-III, a general formulation for the stress intensity factor K takes the form (6),

$$K = \sigma_0 \sqrt{a_0 \pi} f \quad (6)$$

where K is the stress intensity factor,
 σ_0 is the reference stress, usually the yield stress,
 a_0 is the crack length or half of the crack length, and
 f is a geometry and loading type factor

Substituting K with the critical stress intensity factor reveals the maximum load allowable. As the critical stress intensity can be higher when measured through SE(N)T specimens, the allowable fault size in the formula can be increased if other parameters stay constant. The stress intensity factor is only valid for linear-elastic conditions, but

additional corrections can be added to account for plasticity (Wallin, 2011 p. 11) For this thesis the J-integral is used for elastic plastic fracture mechanics. It is a route independent energy principle based on the work done by the external force in forming new fracture surfaces discovered by Rice (1968). It models the elastic and plastic stages of the crack expansion as a non-linear elastic process (Anderson, 2005). Wallin (2011 p. 17) states that as there exists a unique relationship between the J-integral and K_I in the linear elastic region, J can be quantified as a toughness measure expressed through K. This relationship can be extended to the plastic region if no unloading takes place. In addition, Rice and Rosengren (1968) found that in a power hardening material the stress contours around the crack tip and the J-integral correlates through what the authors designated as the Hutchinson-Rice-Rosengren (HRR) field (Wallin, 2011 p. 18). The HRR field is used later in this thesis to derive constraint parameters.

Another way stresses can concentrate are defects such as segregations and precipitates in the material. Under stress, dislocations are introduced They travel and pile up at high energy boundaries of precipitates, grains, and triple boundaries, where their stress fields superimpose. The number of dislocations that can pile up is dependent on the grain size. (Kaufmann, 2011; Wallin, 2011)

If a tensile yield specimen is considered to be a notchless sample, the behavior it exhibits can be generalized to represent the lowest crack-constraint for that specific geometry. However, depending on the strain hardening behavior, necking of the tensile specimen will introduce a variability to the specimen constraint (Hertzberg, 1976 p.24). The difference of continuum models and realistic materials with internal flaws and inhomogeneities is highlighted by the difference in necking between a single crystal flawless specimen and a normal grainy metallic material. A perfect crystal necks up to a very fine point compared to more conventional tensile specimens that neck to a certain degree demonstrating ductile behavior, before breaking off, Figure 2. (Anderson, 2005 p. 220)

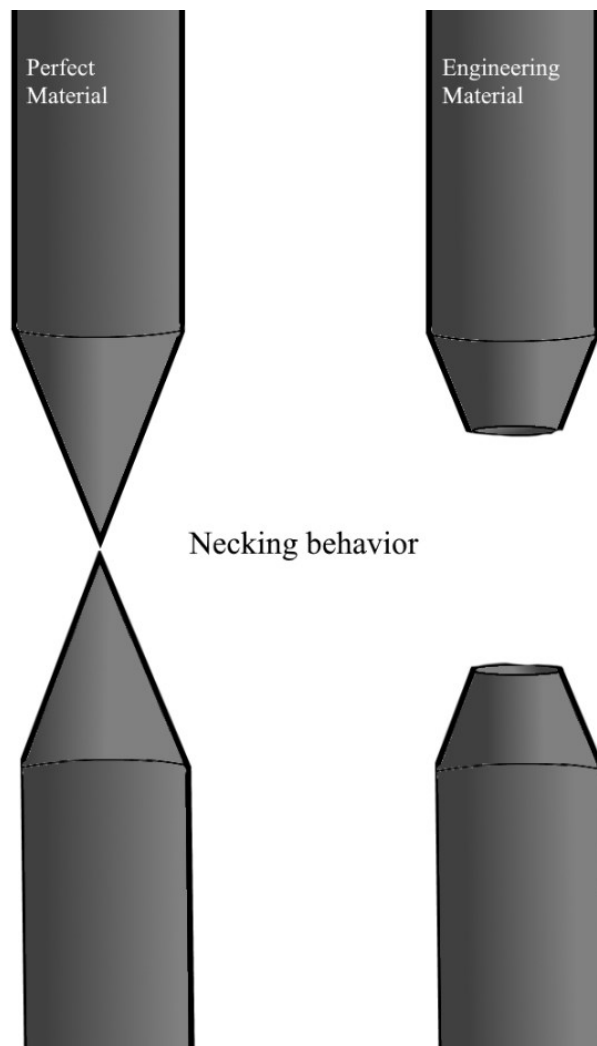


Figure 2 Hardening and necking behavior of perfect and engineering materials in tensile testing.

2.2 Fracture mechanisms

The thesis research mainly focuses on brittle fracture, but mixing of the fracture types in real world applications warrants examination of both ductile and brittle mechanisms. Ductile materials fail usually by nucleation and growth of voids that connect into a growing crack. Brittle fracture occurs by separation between crystalline planes, usually nucleating from a single point of origin from which it propagates. It can be trans granular when it passes through grains and intergranular when it cleaves through grain boundaries. Cleavage fracture can be preceded by large plastic deformation and ductile crack growth,

(Anderson, 2005) and the local crack tip conditions are especially important in determining the cleavage fracture resistance and initiation (Wallin, 2011).

2.2.1 Void nucleation and coalescence

In a similar way to the metallic matrix fracture formation summarized in 2.1, voids nucleate by breaking the bonds between phases after reaching a critical stress level. Non-metallic particles in the matrix can also crack and initiate a larger fracture process, but the common factor for both of these mechanisms is the formation of new free surfaces. The practical effect of inhomogeneities were highlighted in section 2.1.2 and Figure 2, but on a microscopic scale different mechanisms take place for different sized segregate particles and sub micrometer precipitates. According to Anderson (2005) the most commonly used continuum model for above micron particles is the Argon, Im and Safoglu model (1975) that combines the material critical interphase cohesion stress from the principal stresses and hydrostatic stress (7),

$$\sigma_c = \sigma_e + \sigma_m \quad (7)$$

where σ_c is the critical interphase cohesion stress,
 σ_e is the effective Von Mises stress, and
 σ_m is the mean hydrostatic stress.

The Von Mises and hydrostatic stresses are related to the principal stresses through (8 and 9)

$$\sigma_e = \frac{1}{\sqrt{2}} [(\sigma_1 - \sigma_2)^2 + (\sigma_1 - \sigma_3)^2 + (\sigma_3 - \sigma_2)^2]^{\frac{1}{2}} \quad (8)$$

$$\sigma_m = \frac{\sigma_1 + \sigma_2 + \sigma_3}{3} \quad (9)$$

where σ_{1-3} are the principal normal stresses.

The model indicates that as the triaxiality increases, void nucleation is more likely. There have been variations of this model developed through comparison to experimental data, but the main principle is the same between them.

The Goods and Brown (1979) model for sub-micron particles is based on dislocations increasing the interphase stresses in conjunction with maximum principal stress (10 and 11),

$$\sigma_c = \Delta\sigma_d + \sigma_1 \quad (10)$$

$$\Delta\sigma_d = 5.4\alpha_c\mu\sqrt{\frac{\varepsilon_1 b_V}{pr}} \quad (11)$$

where $\Delta\sigma_d$ is the dislocation stress,
 α_c is a constant between 0.14 and 0.33,
 ε_1 is the maximal remote normal strain,
 μ is the shear modulus,
 b_V is the Burger's vector, and
 pr is the particle radius.

The continuum model is insensitive of particle size, while the sub-micron model takes it into account. Experimental results deviate from both models with one explanation being the cracking of particles. Smaller particles (up to a certain point) make nucleation easier, but larger particles are more likely to crack. Softer and harder particles behave differently and the general shape and orientation of them can be manufacturing dependent. Manufacturing processes often transform or break these particles resulting in favorable conditions for void nucleation. The effect of void coalescence and nucleation around hard particles can be seen from Scanning electron microscope SEM images as dimples on the fracture surface. (Anderson, 2005)

2.2.2 Brittle cleavage fracture

If the energy principle through bond enthalpy and entropy is considered, certain crystallographic planes are more prone to cleavage fracture. The lower the packing

density, the fewer bonds need to be broken and the distances between atoms are larger lowering the bond strength in general. It was previously stated that the glide of dislocations prefers the tightest packed planes. Opposite to that, fracture favors the loosest packed planes. The combination of larger elastic energy and lower bond strength of low packed planes generally provide the most energetically efficient crack formation. If the plastic flow of the material is hampered, cleavage is more likely to occur. This produces a relation to the cleavage-ductile fracture mechanisms and available active slip planes. As temperature is lowered, BCC and Hexagonal Close Packed (HCP) metals lack the slip planes for adequate plastic deformation while Face Centered Cubic (FCC) is still able to flow. This makes BCC and HCP more likely to fracture by cleavage and they have a transition temperature range where the dominant mechanism changes from ductile to brittle fracture. (Anderson, 2005) There are multiple definitions for the ductile-brittle transition temperature, and it should not be confused with the reference temperature in the ASTM E1921 standard.

The two aforementioned mechanisms for brittle fracture were trans granular and intergranular, with the difference being propagation through (trans) the grain in trans granular fracture contrasted to propagation by grain boundaries in intergranular fracture. One reason for the occurrence of intergranular fracture is temper embrittlement, where impurities such as phosphorus segregate to prior austenite grain boundaries and weaken them when the steel spends extended periods at temperatures around 550 ± 50 Celsius (Yahya et al., 1998)

Wallin (2011) divides the cleavage fracture into three steps:

1. Cracking of a precipitate or inclusion which acts as a local initiation site
2. Propagation of the local initiation site into the surrounding matrix
3. Propagation of the now larger crack into neighboring grains

Which of the states are critical for the fracturing process depends on multiple factors such as geometry, available slip systems, and loading conditions. Whether initiation (step 1.) or propagation (steps 2. and 3.) is dominating, determines if the Master Curve method, which is used in this thesis in the calculation of the T_0 temperature, is valid.

2.3 The Master Curve method

If step 1 controls the fracture process, initiation leads to propagation and failure of the specimen. In other words, if stress conditions are sufficient to initiate a microcrack, they are sufficient to propagate it through the specimen. This weakest link assumption holds in the transition region and transforms the fracture process into a statistical event due to the local inhomogeneities in the material (Wallin, 2011 p.115-117). Master Curve applicability can be assessed from the fracture surfaces. If only one or a few initiation sites are present, the initiation phase was likely to control the fracture process, Figure 3.

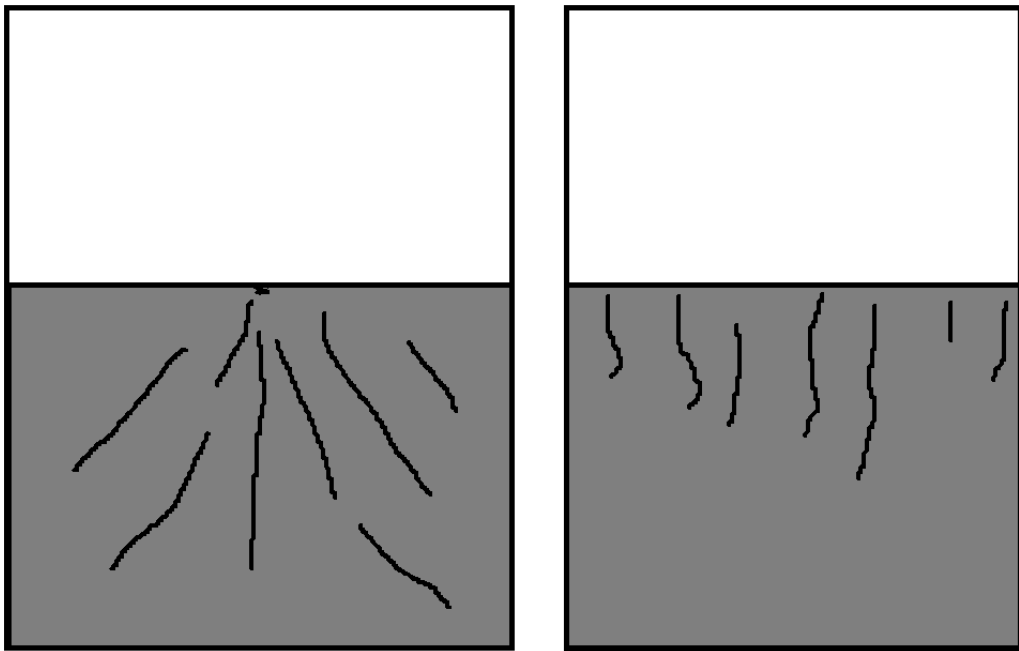


Figure 3 A single initiation source typical for the transition region on the left and multiple fracture initiation sites on the right (Mimicking Wallin, 2011 p. 117).

The Master Curve is a method which assumes that there exists a certain probability of an initiation site existing within the material in front of the crack tip stress field and assigns a probability distribution function for the occurrence of brittle fracture based on it. The

exact number of initiators in a given material volume is unknown, but can be assumed to follow Poisson distribution. If a critical stress is reached at a location susceptible to crack formation, the crack will propagate through the specimen with low resistance in cleavage fracture.(Wallin, 2011 p. 118-125)

In practice, the curve assigns the median K_{Jc} transition temperature and the shape of its lower and upper distribution over a variety of temperatures for 1T scaled sample sizes, Figure 4. (ASTM International, 2021).

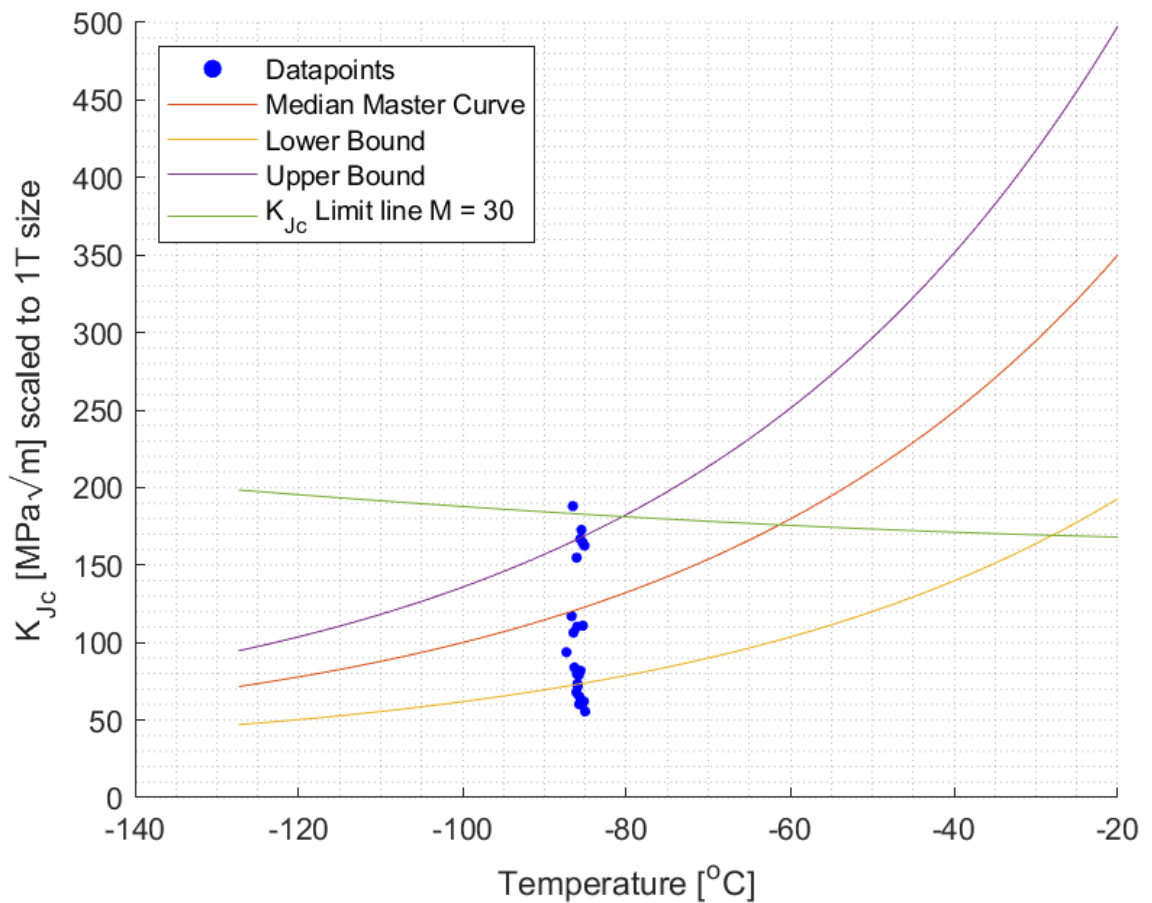


Figure 4 An example of a Master Curve with median, upper, and lower probability distribution lines. In addition, a $M = 30$ measuring capacity limit line is displayed.

A more thorough description with the different cumulative probability summations and extensive theoretical background behind the Master Curve probability distribution can be

found from literature,(Wallin, 2011 Chapter 4), from which key points relevant to the thesis are summarized below.

The exact derivation of the probability function is complicated, but the concept behind it can be simplified using a tree diagram, Figure 5, which lists the different outcomes and probability summations that lead to them.

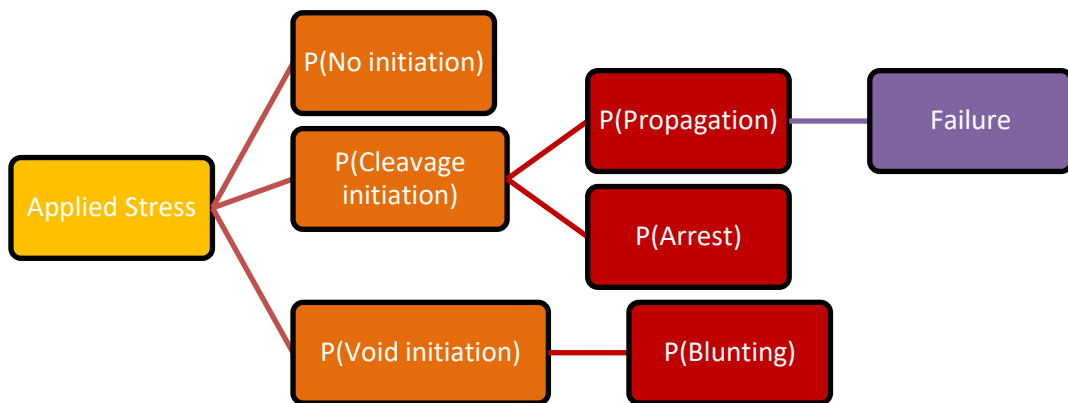


Figure 5 Probabilities of different outcomes for faults under stress mimicking (Wallin, 2011 p. 119).

The Poisson distribution of the initiators takes the form (12),

$$P_N = \frac{\bar{N}^N \exp(-\bar{N})}{N!} \quad (12)$$

where P_N is the probability of having N initiators in a sample,
 N is the number of initiators, and
 \bar{N} is the mean number of initiators.

This formulation allows simplification using the exponential equation (13),

$$e^x = \sum_{N=0}^{\infty} \frac{x^N}{N!} \quad (13)$$

and the probability function of a volume element transforms to (14),

$$P_f = 1 - \exp \left\{ -\bar{N} * Pr\{I\} \left(1 - Pr \left\{ \frac{V}{O} \right\} \right) \right\} \quad (14)$$

where P_f is the probability of failure,
 $Pr\{I\}$ is the probability of cleavage initiation, and
 $Pr\{V/O\}$ is the conditional probability that no previous initiation has taken place.

Summing all partial volumes gives the cumulative probability for failure.

For a sharp crack with small scale yielding, stress and strain distributions are assumed to be self similar and have angular dependence as stipulated by the HRR field. This allows the crack front to be divided into radial elements which can then be summed over the cleavage fracture process volume. The self similarity allows normalization through stress intensity factor and yield strength which produces a unit-less stress distribution descriptor, which can be substituted into the cumulative probability function. Additional normalization can be added through the crack front length resulting in the form (15),

$$P_f = 1 - \exp \left\{ -\frac{B}{B_0} \left(\frac{K_I}{K_0} \right)^4 \right\} \quad (15)$$

where B is the crack front width,
 B_0 is a chosen reference width, usually one inch (1T),
 K_I is the stress intensity factor for mode I loading, and
 K_0 is the normalizing fracture toughness corresponding to a 63.2% cumulative failure probability.

If propagation, conditions for starting at minimum fracture toughness, and a constant upper probability corresponding to the convergence value at infinite stress intensity are added, the final Master Curve probability is described by (16),

$$P_f = 1 - \exp \left\{ -\frac{B}{B_0} \left(\frac{K_I - K_m}{K_0 - K_m} \right)^4 \right\} \quad (16)$$

where K_m is the lower limit fracture toughness.

When a certain probability is converted to a specific fracture toughness value some additional assumptions are needed. The scatter for the results follows a three-parameter Weibull probability distribution function with a slope of 4 for ferritic steels (17),

$$\left\{ \ln \left(\frac{1}{1 - P_f} \right) \right\}^{\frac{1}{4}} = \frac{K_{Jc} - K_m}{K_0 - K_m} \quad \text{or} \quad P_f = 1 - e^{-\frac{(K_{Jc} - K_m)^4}{(K_0 - K_m)^4}} \quad (17)$$

where K_{Jc} is the elastic-plastic fracture toughness.

Experimentation by Wallin (2011) has shown that a value for K_m is difficult to obtain due to its scattered nature. A substitution of 20 MPa√m for macroscopically homogenous ferritic steels is used for the standard Master Curve and it should produce accurate results for the thesis research. Temperature adjustment based on empirical experimentations has produced the following relation to the K_0 values (18),

$$K_0 = 31 + 77 \exp\{0.019(T_0 - T)\} \text{ MPa}\sqrt{m} \quad (18)$$

where T is the test temperature, and

T_0 is the Master Curve fracture toughness reference temperature, where median K_{Jc} is 100 MPa√m.

Plotting the results of (18) over a range of temperatures produces the median Master Curve. Transforming the practical measurement data into toughness and T_0 values through the Master Curve is presented in section 5 with the method described in the standard ASTM E1921.

3 CONSTRAINT

A broad theoretical approach is needed as a basis for understanding the constraint effect. As a starting point, Hooke's study of springs leads to the following relations between stress and strain (19 and 20),

$$\sigma = E\varepsilon = \frac{F}{A} \quad (19)$$

$$\varepsilon = \frac{\Delta l}{l} \quad (20)$$

where E is the Young's modulus,
 A is the specimen cross sectional area,
 l is the specimen length, and
 Δl is the change in overall specimen length.

Generalizing these equations into three dimensions reveals that stress in one direction will cause strain in the other two as well (Hertzberg, 1976) as can be seen below in formulas (21-28)

$$\sigma_x = \frac{E}{(1+\nu)(1-2\nu)} [(1-\nu)\varepsilon_x + \nu(\varepsilon_y + \varepsilon_z)] \quad (21)$$

$$\sigma_y = \frac{E}{(1+\nu)(1-2\nu)} [(1-\nu)\varepsilon_y + \nu(\varepsilon_x + \varepsilon_z)] \quad (22)$$

$$\sigma_z = \frac{E}{(1+\nu)(1-2\nu)} [(1-\nu)\varepsilon_z + \nu(\varepsilon_x + \varepsilon_y)] \quad (23)$$

$$\varepsilon_x = \frac{1}{E} [\sigma_x - \nu(\sigma_y + \sigma_z)] (+\alpha\Delta T) \quad (24)$$

$$\varepsilon_y = \frac{1}{E} [\sigma_y - \nu(\sigma_x + \sigma_z)] (+\alpha\Delta T) \quad (25)$$

$$\varepsilon_z = \frac{1}{E} [\sigma_z - \nu(\sigma_y + \sigma_x)] (+\alpha\Delta T) \quad (26)$$

$$\tau_{xy} = G\gamma_{xy}, \tau_{yz} = G\gamma_{yz}, \tau_{xz} = G\gamma_{xz} \quad (27)$$

$$G = \frac{E}{2(1+\nu)} \quad (28)$$

where σ indicates the stress in the index direction,
 ε indicates the strain in index direction,
 $\alpha\Delta T$ is the thermal expansion coefficient,
 τ is the shear in the index directions,
 γ is the glide in the index directions,
 ν is the Poisson's ratio, and
 G is the shear modulus derived from the Young's modulus E .

for isotropic materials.

In order to keep the strain field planar, and the ε_{33} strain at zero, there needs to be a σ_{33} stress caused by the surrounding material resisting plastic flow or necking of the material. At free surfaces there is no surrounding material restricting the flow of matter to provide an opposing force as required by Newton's 3rd law (Newton, 2016) and the σ_{33} stress must be zero. This results in strain, as there is nothing constraining the geometry from outside the free surfaces. (Ikonen & Kantola, 1991.) From this, it can be further derived that there are plane stress conditions at the surfaces, which transform to more triaxial stresses and planar strains towards the center of the specimen, (29 and 30).

$$\begin{bmatrix} \sigma_{11} & \sigma_{12} & 0 \\ \sigma_{21} & \sigma_{22} & 0 \\ 0 & 0 & \sigma_{33} \end{bmatrix} \rightarrow \begin{bmatrix} \varepsilon_{11} & \varepsilon_{12} & 0 \\ \varepsilon_{21} & \varepsilon_{22} & 0 \\ 0 & 0 & 0 \end{bmatrix} \text{plane strain} \quad (29)$$

$$\begin{bmatrix} \sigma_{11} & \sigma_{12} & 0 \\ \sigma_{21} & \sigma_{22} & 0 \\ 0 & 0 & 0 \end{bmatrix} \rightarrow \begin{bmatrix} \varepsilon_{11} & \varepsilon_{12} & 0 \\ \varepsilon_{21} & \varepsilon_{22} & 0 \\ 0 & 0 & \varepsilon_{33} \end{bmatrix} \text{plane stress} \quad (30)$$

The relations between the three-dimensional stresses and strains are described by (21-30), but the exact gradient from plane stress to plane strain is difficult to determine.

Using the above formulations, constraint can be defined in the following way:

Constraint is the restriction on material flow, which through Poisson's effect would reduce the formation of triaxial stresses.

Constraint relates back to material toughness, as it is related to the ability of the material to deform plastically. As constraint increases, the material flow is further hampered, the fracture mechanism becomes more brittle, and plastic deformation cannot absorb energy. This leads to the lowered toughness typically observed in higher constraint specimens.

3.1 Factors affecting constraint

Load, geometry, and sample size can affect constraint depending on their permutations. For example, different attachment methods such as pin loaded or clamped introduce a varying moment force as a result of loading. Stress is also concentrated in a different manner between bending and tensile loading. The effects of load and geometry on stress concentration can be estimated through the f factor in (6) with different cases presented for example in the appendix of Ikonen and Kantola (1991). Different geometries also produce different sensitivities for constraint changes. The Single Edge Bend (SEB) specimen produces a large shift in constraint by varying the a/W crack depth ratio (Lindqvist & Boåsen, 2019). Different specimen and their constraint associated toughness results are presented below in Figure 6.

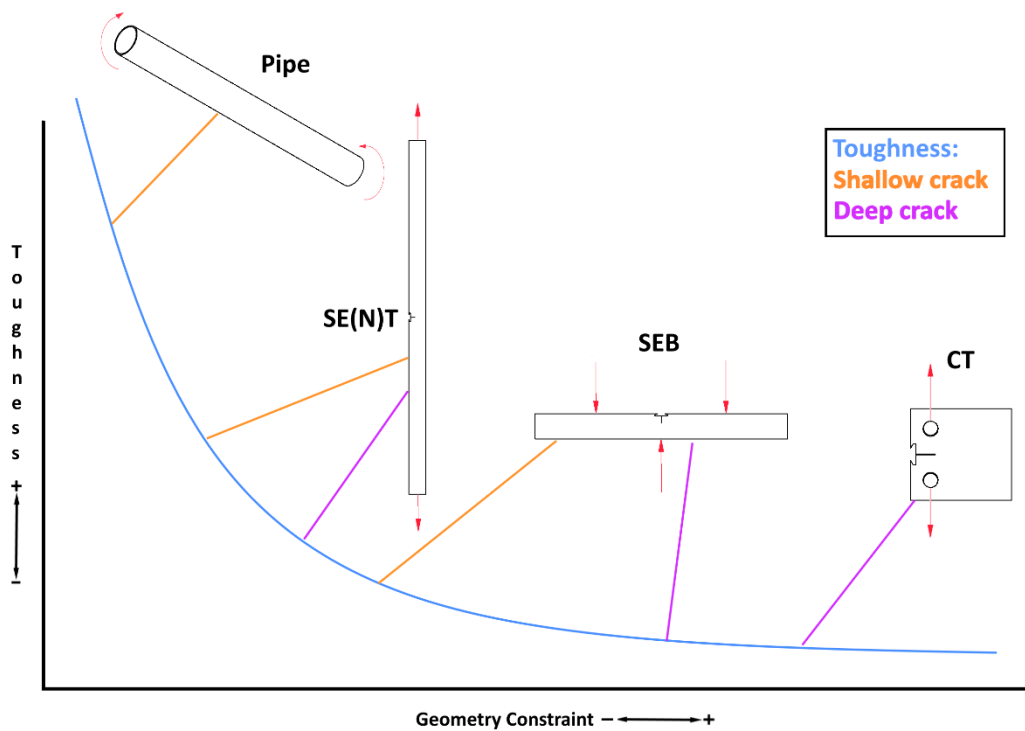


Figure 6 Toughness for the same material derived from varying specimen test configurations mimicking (Lindqvist & Boåsen, 2019).

3.2 Quantifying constraint

The aforementioned stress triaxiality can be understood as a manifestation of constraint (Lindqvist & Boåsen, 2019). Materials in the real world have inhomogeneities, boundary layers and non-uniform load distributions that affect the crack tip stress fields and the singularity dominated region that is the basis for single parameter stress field correlations to J and K . While the stress perturbations of these heterogeneities remain small compared to the overall geometry scale, J and K still “communicate” the effect of the disturbances, such as boundary layers or free surfaces to the crack tip. (Dodds et al., 1993) When the elastic portion through K and plastic deformation through J are no longer correlated one-to-one between the near tip field and the external conditions, the constraint is lost. (Dodds et al., 1993) In practice, the loss of constraint leads to less restricted material flow and tougher fracture results. As the single parameter assumption stops describing the crack tip stress-fields, the results become geometry and load dependent. To compliment the

lacking single parameter models, several additions have been developed to introduce additional terms describing the other factors effecting the crack tip conditions and there are multiple different models that can be used to estimate the constraint effect on the fracture toughness estimate.

3.2.1 Elastic T-Stress

Williams (1956) showed that the stress fields at the crack tip for isotropic elastic material can be described by an infinite power series, (31). Omission of terms other than the first leads to the single parameter crack tip stress expression of classical fracture mechanics, (6). Anderson (2005) highlights the importance of the second term as it can have “profound effect on the plastic zone shape and the stresses deep inside the plastic zone”. The first two terms of the Williams series under Mode I loading are as follow, (31)

$$\sigma_{ij} = \frac{K_I}{\sqrt{2\pi r}} f(\theta) + \begin{bmatrix} T_s & 0 & 0 \\ 0 & 0 & 0 \\ 0 & 0 & \nu T \end{bmatrix} + \dots \quad (31)$$

where T_s is an uniform stress in front of the crack in a direction parallel to it,
 σ_{ij} is stress in the i-j direction,
 θ is the angle in front of the crack tip,
 νT is the resulting z direction stress due to T_s , and
 r is the distance in front of the crack tip,

In the case that $T_s = 0$ single parameter conditions are satisfied. If T_s has highly negative values, it can lower the magnitude of the overall stress field.

Biaxiality ratio β_x is commonly used to describe the T-stress, (32)

$$\beta_x = \frac{T_s \sqrt{\pi a}}{K_I} \quad (32)$$

where β_x is the biaxiality ratio.

For SE(N)T specimens (and many other standard specimen geometries) under mode I loading, T-stress is represented by (33)

$$T_s = \frac{\beta_x F}{B\sqrt{\pi a W}} f \quad (33)$$

where F is the loading force, and
 W is the specimen thickness.

Depending on the chosen fracture toughness estimate, such as the master curve method, the T_0 temperature can be shifted as a result of changing constraint. Using the T-stress estimates, this shift is quantified by (34-36) for SEB and SE(N)T specimens. (Wallin, 2011)

$$\Delta T_0 = A \left(\frac{\Delta T_s}{\sigma_{ys}} \right) \quad A = 40^\circ C \text{ for } \sigma_{ys} < 600 \text{ MPa} \quad (34)$$

$$\text{for SET } \frac{\Delta T_s}{\sigma_{ys}} = -0.73 + 0.65 \left(\frac{a}{W} \right) + 1.76 \left(\frac{a}{W} \right)^2 - 1.37 \left(\frac{a}{W} \right)^3 \quad (35)$$

$$\text{for SEB } \frac{\Delta T_s}{\sigma_{ys}} = -1.13 + 5.96 \left(\frac{a}{W} \right) - 12.68 \left(\frac{a}{W} \right)^2 + 18.31 \left(\frac{a}{W} \right)^3 - 15.7 \left(\frac{a}{W} \right)^4 + 5.6 \left(\frac{a}{W} \right)^5 \quad (36)$$

where ΔT_0 is the shift in T_0 temperature,
 A is a factor dependent on material, and
 ΔT_s is the change in T-stress conditions.

As the constraint is lowered, the T-stress values become negative and have a reducing effect on the stress concentration amplitude. The T-stress relies on elastic assumptions and loses its capabilities as plasticity increases. The T-stress becomes undefined in fully yielded conditions, and its value saturates near the K-limit load. (Anderson, 2005; Moattari & Sattari-Far, 2017; Lindqvist & Boåsen, 2019.)

3.2.2 Q-parameter

O'Dowd and Shih (1991, 1992) discovered that for a power hardening material, the power-series which describes its small-scale yielding plane-strain fields can be formulated to have the HRR field as the first term. The rest of the higher order terms can then be considered as a difference field, which is highly independent from the distance forward of the crack. (Dodds et al., 1993; Anderson, 2005 p. 140-143.) This difference field corresponds to a uniform hydrostatic stress in the sector directly in front of the crack tip and quantifies the triaxial stress at the crack tip vicinity (Dodds et al., 1993). The magnitude of this difference field becomes the Q-parameter when the HRR stress is taken at a distance r normalized through a reference stress σ_0 , (37)

$$\delta \propto \frac{J}{\sigma_{ys}}, \quad \frac{r\sigma_0}{J} = 2, \quad \theta = 0 \quad (37)$$

where δ is the crack opening displacement, and
 J is the J-integral value.

The Q-parameter is theoretically independent of the distance, but the used normalization ratio of two for (37) should lie just beyond the blunting region of the crack tip (Dodds et al., 1993). While the J-integral scales the deformation at the crack tip, the Q-parameter quantifies the stress triaxiality within the radius of $1-8 \delta$ from the crack tip.

The Q-parameter starts to deviate from the T-stress estimations for large scale yielding conditions (Moattari & Sattari-Far, 2017). As the T-stress fails for a more plastic fracture, the Q-parameter is more robust for real world applications and remains dynamic over the whole yielding scale (Dodds et al., 1993). For this thesis, the Q-parameter is defined through the difference of the reference stress field and the actual stress at a location normalized by σ_{ys} , taking the form (38-39)

$$Q \equiv \frac{\sigma_{yyFEA} - \sigma_{yyHRR}}{\sigma_0}, \quad \frac{r\sigma_0}{J} = 2, \quad \theta = 0 \quad (38)$$

$$\sigma_{yyHRR} = \sigma_{ys} \left(\frac{EJ}{\alpha_{RO} \sigma_{ys}^2 I_n r} \right)^{\frac{1}{n_{RO}+1}} \tilde{\sigma}_{IJ}(n_{RO}, \theta) = 1626 \text{ MPa} \quad (39)$$

where Q is the Q-parameter,
 σ_{yyFEA} is the actual stress in the crack opening y direction from a FEM model,
 σ_{yyHRR} is the HRR reference stress in the crack opening y direction,
 I_n is a strain hardening related constant, and
 $\widetilde{\sigma}_{ij}(n, \theta)$ is an angular dependence constant.

and the r used in (39) is normalized with the ratio of two as presented in (37).

The shift in T_0 temperature through the Q-parameter can be estimated using formula (40),

$$\Delta T_0 = T_{corr}(Q - Q_{ref}) \quad (40)$$

where T_{corr} is a correcting factor, and
 Q_{ref} is the Q-parameter value for the same material from a reference C(T) type sample. (Anderson, 2005 p. 133170; Wallin, 2011 p. 820; Moattari and Sattari-Far, 2017.)

4 DESIGN OF THE SE(N)T SPECIMEN

Previous testing on SE(N)T specimens has mostly focused on J-R crack growth resistance curves, where the fracture resistance is evaluated with a procedure that forces the crack to open, grow, and through the unloading gradient evaluates the fracture toughness. A review on the different standards by Zhu (2017) compiles the differences and similarities between the most prominent and highlights how the different standards overlap with each other.

The SE(N)T is a specimen type suited especially for tests analogous of pipeline conditions with tensile loading, due to its constraint behavior (Park et al., 2017). The method and specimen are described in the British Standard Institution (BSI) standard BS 8571:2014 (British Standards Institution, 2014), CANMET (Park et al., 2017) implementation, a similar document by Exxon Mobil (Panico et al., 2017), and Det Norske Veritas Recommended Practice DNV-RP-F108 2006. The aforementioned standards alone are not enough for the desired combination of shallow notch, sub sized dimensions, and the Master Curve method, which the experiments of this thesis require. ASTM E1820-20b and E1921-21 are used to substitute their shortcomings while the various standards are applied for other best practices. Still, no ultimate guide exists, which would provide thoroughly validated methods for the type of SE(N)T testing conducted in this thesis, especially on the estimation of measurement and method uncertainty. It should also be noted that the BSI standard used for reference has been made obsolete by a new revision, which was unavailable.

4.1 General SE(N)T specimen dimensions

The different standards demand a free, unconstrained length that is ten times the width of the specimen combined with sufficient grip allowance depending on the test apparatus. Many aspects of the design for this thesis are limited by the available equipment. For example, the load cell uses special mechanical grips that wedge the vises shut as tension increases. This is to allow low temperature testing unsuitable for hydraulic actuators. The test grips require 55 mm of material for attachment. The orientation of the grips and any

extra free sample length affect the rotational moment that arises due to the notched geometry. The total length of the specimens is thus rendered at 210 mm, two times 55 mm for each grip and a 100 mm free surface between them.

The specimen width to thickness ratio W/B is set at one and the cross section is therefore a square. A square geometry was chosen in part as it results in a lower stress gradient over the specimen width under load (Anderson, 2005). Furthermore, Charpy V type notched impact specimens can be manufactured from the broken halves of a $10 \times 10 \text{ mm}^2$ SE(N)T specimen. Proven formulas and analysis methods for the square geometry with a length ten times the width have also been validated in the CANMET SE(N)T test method and the standard BS8571 (British Standards Institution, 2014; Park et al., 2017).

4.2 Crack and knife edge depth

As the general sample dimensions set the boundaries for the subsequent geometry parameters, it also determines the limits for the crack and knife edge dimensions. The crack length is chosen as the variable which is changed to reveal the effect of constraint phenomena. Since only a single knife edge configuration is considered, only the J-integral can be determined from the measurements. A two-clip system could be used to estimate the C(T)OD based on the COD values and trigonometry. A common $0.5 a/W$ ratio is chosen to represent high constraint conditions, and $0.2 a/W$ to represent lower constraint as it still has relevant datapoints for comparison. It is also the lower limit ratio for many other experiments found in the literature. The ASTM standard E1820 (2020) X-appendixes give guidelines for shallow notches and knife edges for the CMOD gauges. The smallest available 3 mm clip gauge requires 0.72 mm of depth to allow for free rotation through the crack-opening motion, Figure 7. To accommodate condensation and thawing at the test temperatures, this space is increased to 0.8 mm.

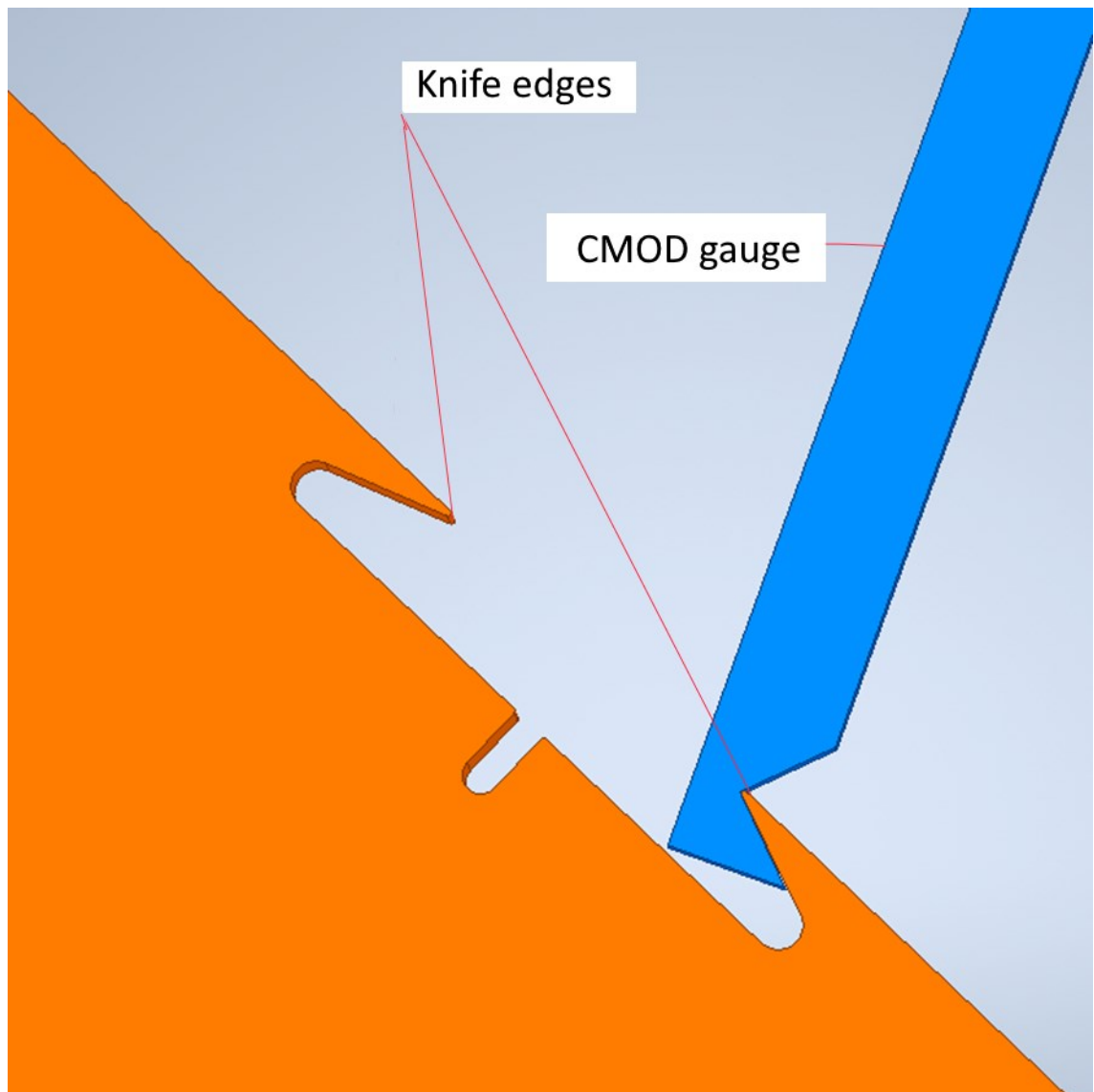


Figure 7. C(T)OD clip gauge arm (blue) and the knife edge it rotates around (orange) requires 0.72 mm of space.

Several options as the basis for the knife edge and pre-crack geometries were explored. One of the main downsides of the BSI standard (2014) is the strict minimum requirement of 1.3 mm for the fatigue crack extension. For a sample with a width of 10 mm and an a/W ratio of 0.2 this would leave 0.7 mm which is not enough even for the rotation of the CMOD gauge let alone the pre-crack in addition to it. External knife edges are proposed as an alternative, but their attachment becomes an issue. Machine screws or spot welds

are recommended in both BS 8571:2014 and ASTM E1820-20b, but they are only suitable for larger overall geometries. The Heat affected zone (HAZ) would be too large in such a small specimen rendering it unusable. The BSI standard (2014) demands that screws must be within a distance determined by equation (41),

$$d_s = \frac{W-2\phi_s}{4} \quad (41)$$

where d_s is the distance of the threaded hole center,
 ϕ_s is the thread diameter.

For standard metric threads M3 is too large intersecting the pre-crack and M2 would be 0.5 mm away from the notch, even M1 threads would be uncomfortably close and interfere with the stress fields formed during testing.

An alternative method for attaching the external knife edges by gluing was investigated. Glues used for strain gauges are assumed to pass the required scientific rigor and repeatability for accurate results. X60 formulation was considered as an option that can attach smooth metallic surfaces without needing a hot curing and has a reported operating range down to -200 °C (HBK, 2022). Gluing was abandoned for the thesis set of experiments due to time constraints. A test adhesion experiment would be too time consuming, and a separate jig would have to be constructed to assure consistent knife edge-specimen attachment. Nevertheless, gluing proposes an interesting avenue for future test configurations. There should be no strong strain fields near the surfaces where the knife edges would be glued to, and if a strong enough shear load formed breaking the adhesive bond, it would be an interesting result within itself.

After consideration, the internal knife edge geometries suggested for shallow cracks from ASTM 1820-20b were chosen and modified, as they allow for shorter fatigue pre-crack lengths leaving room for the CMOD gauge. Limitations instilled on the geometry ratios between different dimensions of initial and fatigue cracks are used to define the notch geometry. The width of the pre-crack must be less than 0.063W, which can be achieved by using an Electric Discharge Machining (EDM) wire cutter. The notch should also be as narrow as possible to minimize the elastic compliance of the specimen, especially for

narrow notches (ASTM International, 2020). A wire diameter of 0.2 mm will result in a notch with the width of around 0.3 mm. An EDM wire will also form the recommended “narrow-notch” geometry (ASTM International, 2020).

The standard (ASTM International 2020) demands that the ratio between the pre-crack and fatigue crack based on the stress intensity factor and the resulting plastic zone radius r_p , (42).

$$r_p = \frac{1}{3\pi} \left(\frac{K}{\sigma_{ys}} \right)^2 > 1.5a_1 \quad (42)$$

where r_p is the plastic zone radius,
 a_1 is the machined notch depth.

For this application the value for K is defined by equation (43),

$$K = \left[\frac{PS}{(BB_N)^{\frac{1}{2}} W^{\frac{3}{2}}} \right] f \left(\frac{a_1}{W} \right) \quad (43)$$

where P is the three-point bending force used for the pre-cracking (44),
 B_N is the notched thickness of the sample = B for the pre-cracking phase,

$$P = \frac{0.5B(W-a_1)^2 \sigma_{ys}}{S} \quad (44)$$

where S is the distance between supports

The geometric shape factor is found using the formula (45).

$$f \left(\frac{a_1}{W} \right) = \frac{\left(3 \left(\frac{a_1}{W} \right)^{\frac{1}{2}} \left[1.99 - \left(\frac{a_1}{W} \right) \left(1 - \left(\frac{a_1}{W} \right) \right) \left(2.15 - 3.93 \left(\frac{a_1}{W} \right) + 2.7 \left(\frac{a_1}{W} \right)^2 \right) \right] \right)}{2 \left(1 + 2 \left(\frac{a_1}{W} \right) \right) \left(1 - \left(\frac{a_1}{W} \right) \right)^{\frac{3}{2}}} \quad (45)$$

As the r_p is affected by the machined notch depth a_1 , the fatigue crack limit forms a system of equations, and the desired geometry cannot be assumed to fulfill the requirements. An

easier solution than solving the system of dependent equations is to test a set ratio to see the range parameters that allow the set crack sizes. The following values were tested for the formulas (42-45), and they produced measures which could be manufactured:

The SEB specimen stress geometry factor (45) is appropriate for the SE(N)T specimen as the fatigue pre cracking is done with a bending load. The distance between the supports S is set at $4W$. As the a_1/W ratio is the adjusted factor for the experiment, it is set at 0.2 for the low constraint example and 0.5 for the high constraint example. From these a/W ratios the total crack length can be determined to be 2 mm for the low- and 5 mm for the higher constraint specimen.

An a/W 0.2 notch loses 0.8 mm to the knife edge cutout leaving 1.2 mm left for the pre and fatigue crack. Operators who conduct the pre-cracking stated the process to be difficult to control. Having a deeper machined notch will improve the result. A 0.7 mm machined notch in addition to the knife edge leaves 0.5 mm fatigue growth for pre-crackig and falls within the limits set by the standard.

The a/W 0.5 specimen has more leeway in notch depth design, and the geometry was set at 3.5 mm machined and 1.5 fatigue crack. The notch and knife edge geometries are presented below in Figure 8 and the only difference between the two specimen types is the notch depth.

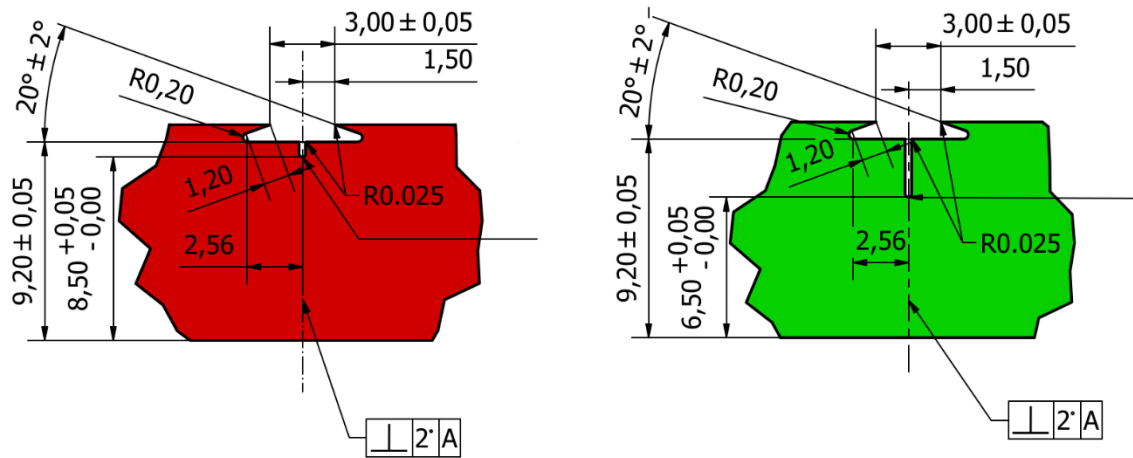


Figure 8. The two , a/W 0.2 (red) and a/W 0.5 (green),machined notch and knife edge geometries, dimensions in [mm].

4.3 Knife edge geometry

Another factor considered was the rounding of the knife edge base. Their investigation was motivated by the concern that the threading for the external attachment of knife edges would interfere with the test stress fields. As the knife edge is close to the shallow pre-crack of the a/W 0.2 sample, the stress concentration caused by the crack was feared to extend to the knife edge area and be affected by it. Rudimentary Finite Element Method (FEM) analysis was conducted using Abaqus CAE (Dassault Systemes SIMULIA corp., 2022), (described in section 5.6) and varying the rounding. To lower the computational cost and stay within the limits of the available license, the piece specimen was modelled as 2D planar model. The material was set to have a Poisson's ratio of 0.3, Young's modulus of 210 GPa, yield strength of 580 MPa with an elastic portion of 0.2% and density of 7.8 kg/dm³.

The constraints were set at the clamp surfaces on one end preventing U_{1-3} movement and rotation. The other end was set to load the specimen with a linearly ramping force close to the yield point of the material as the model was not configured properly to take into account large plastic deformation. The mesh density was locally increased around areas of interest and the formation was unmapped and the element type was a linear triangular

element. As a result of the investigation 0.2 mm roundings were chosen for the knife edges.

4.4 Side grooves

After fatigue pre-cracking, the specimen sides are grooved by the crack, to steer the fracture into a straighter growth during testing, Figure 9. The groove specifications are adopted from the recommendations of ASTM E1820 and CANMET. The final groove geometry is limited by the available machinery, and a Charpy V impact specimen notch profile was chosen due to its convenience. The final notch depth is set to 0.75 mm on each side amounting to 15% reduction in the specimen width B by the standard recommendations. This rather shallow depth also reduces the milling forces and flex of the machining bit, resulting in a more reproducible process. The angle of the notch is 45 degrees with a rounding of 0.25 mm. The rounding is sharper than recommended in the standards, but this could not be avoided due to the limitations of the manufacturing method.

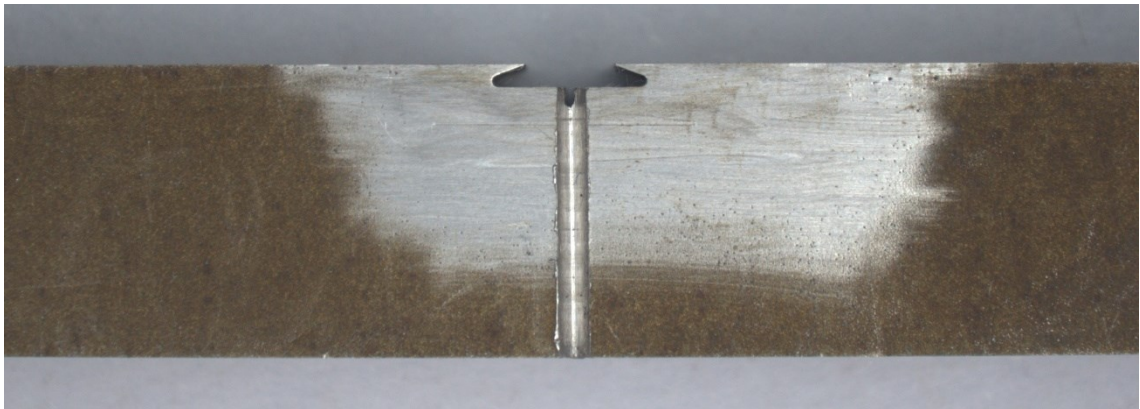


Figure 9 A SE(N)T specimen with a side groove machined into it.

All of the design aspects (excluding side grooves) of the SE(N)T specimens used for the thesis experiments can be seen in Appendix 1, which contains the technical drawings used for their manufacturing.

5 MATERIALS AND METHODS

5.1 Test material

The testing is conducted on an IAEA correlation monitor material designated JRQ (Brumovsky et al., 2001). It was melted, cast, and rolled in Japan during the 80's as an ASTM A533 B Class 1 steel plate formed into a 225 x 2500 x 3000 mm³ slab, which was heat treated and flame cut into 225 x 1000 x 1000 mm³ pieces (Wallin et al., 1995; Brumovsky et al., 2001). The plate was normalized at 900 °C, quenched from 880 °C and tempered at 665 °C for twelve hours followed by a 40-hour stress relieving at 620 °C (Brumovsky et al., 2001). Wallin and colleagues (1995) also noted that there is a “rather large toughness gradient in the thickness direction”. Further internal studies at VTT, such as the one by Lindqvist and Peltonen (2021), have confirmed this observation and further characterized the material properties.

While the original slab has mostly been used in previous experiments, a remaining 15 - 41 - 3 cm³ plate was chosen since it did not show any markings from the original surfaces indicating a more central origin. Figure 10 illustrates the chosen sample material piece., A slice was removed from it and five 50 mm sample buttons were manufactured to compare the sample material properties to those reported previously, Figure 11. At least six uncensored measurement results are needed to form the master curve at the test temperature range,(Wallin, 2011; ASTM International, 2021) and the remaining material allowed the manufacturing of 24 specimens with the chosen outer dimensions.

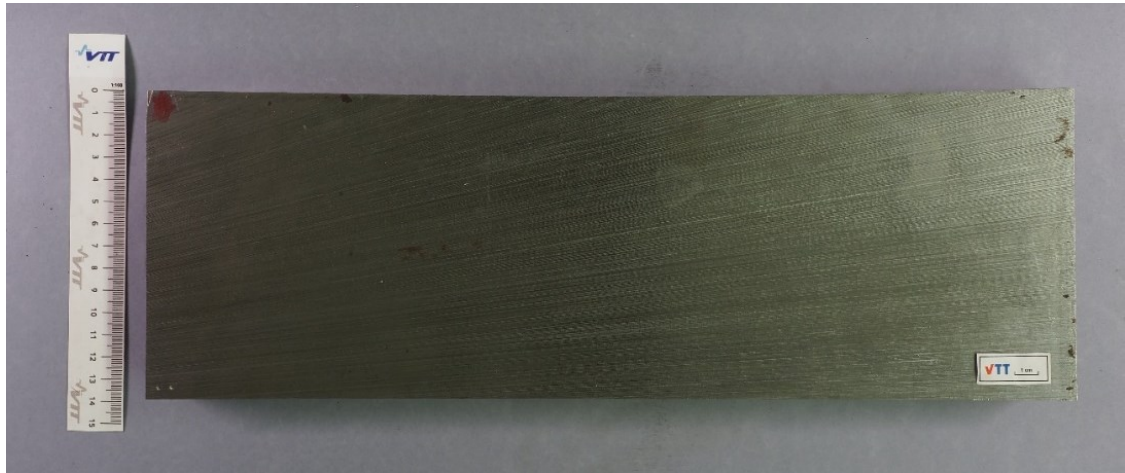


Figure 10. The chosen sample material piece.

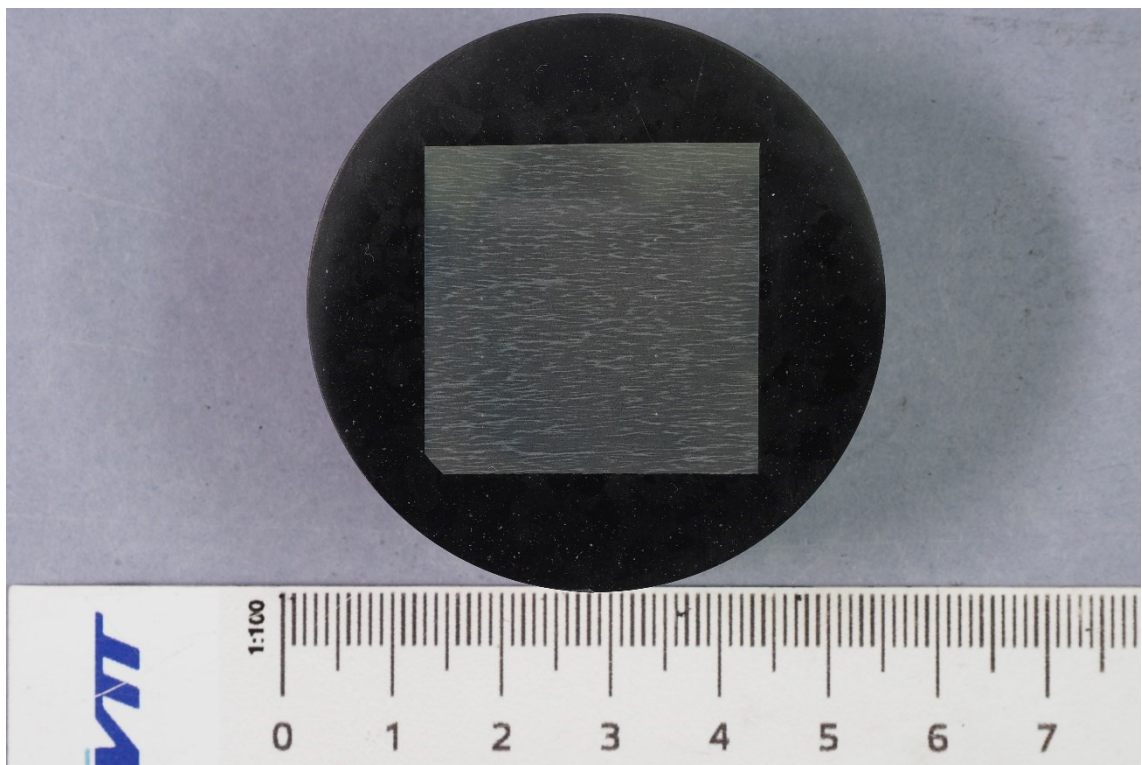


Figure 11. 50 mm sample button manufactured from the sample material. The rolling direction is visible as left to right and the notch indicates the orientation in relation to the parent material, dimples from the HV10 measurement can also be seen upon closer inspection.

A Zeiss Axiom Observer microscope was used to determine the orientation from a Nital-etched sample, Figure 11, and compared to previous similar images, but the rolling direction is visible to the unaided eye from the etched surface as well.

5.1.1 Hardness measurements

The Vicker's hardness (HV10) varies from roughly 220 HV at the surfaces and decreases to 185 HV in the center based on an earlier study (Lindqvist & Peltonen, 2021). To verify the previously measured mechanical properties and locate the sample material in relation to the original slab, 45 new HV10 tests were conducted across the sample plate geometry. The measuring device was calibrated with five calibration measurements into a calibration piece of known hardness before the test piece was examined.

The hardness and microstructural appearance match those of quarter thickness measurements from the original slab, and this information combined with documentation from previous experiments leaves only two possible locations from which the sample material could originate, as illustrated in Figure 12.

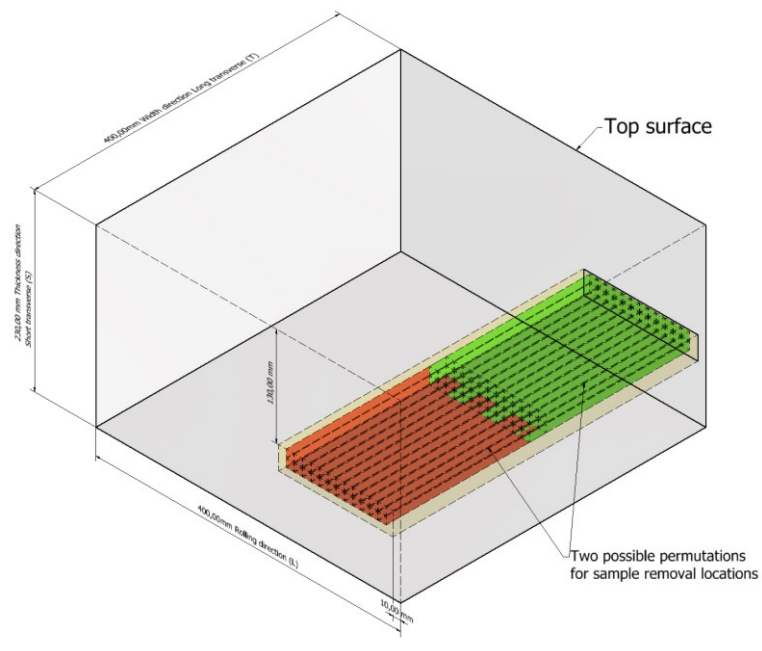


Figure 12 Sample material location in relation to the original slab, the two possible permutations are presented in red and green.

5.1.2 Material composition

The composition of the material was determined previously from three different depths using optical emission spectrometry (OES) in the study by Lindqvist and Peltonen (2021), Table 2, and this data is used for the thesis investigation. There is no major gradient in the elemental distribution through the measured thickness and it is almost identical throughout the slab. These composition measurements are also consistent with the values reported by Brumovsky and colleagues (2001).

Table 2. Chemical composition of the sample material through its thickness determined with OES (Lindqvist and Peltonen, 2021)

| Distance from plate surface | Chemical composition [w %] | | | | | | | | | | | | | | | |
|--------------------------------|----------------------------|------|------|-------|-------|------|------|------|------|-------|-------|-------|-------|-------|-------|---------|
| | C | Si | Mn | S | P | Cr | Ni | Mo | Cu | Al | W | V | Ti | Co | Nb | B |
| OES1 20 [mm] | 0,17 | 0,24 | 1,43 | 0,006 | 0,017 | 0,13 | 0,84 | 0,50 | 0,15 | 0,017 | <0,01 | 0,005 | 0,002 | 0,006 | 0,003 | <0,0005 |
| OES2 55 [mm] | 0,18 | 0,24 | 1,42 | 0,007 | 0,017 | 0,13 | 0,85 | 0,49 | 0,16 | 0,017 | <0,01 | 0,005 | 0,002 | 0,006 | 0,003 | <0,0005 |
| OES3 95 [mm] | 0,18 | 0,24 | 1,42 | 0,006 | 0,016 | 0,13 | 0,83 | 0,50 | 0,15 | 0,018 | <0,01 | 0,006 | 0,002 | 0,006 | 0,003 | <0,0005 |

The microstructure was previously characterized as mostly lower bainitic with local regions of upper bainite. Lath like structures were found near segregates, which were speculated to be martensitic. Some large segregations suspected to be manganese sulfite were also reported present. Lindqvist and Peltonen (2021) determined the average grain size to be between 20 and 45 μm (depending on the sample location) using Electron backscatter diffraction (EBSD). The EBSD analysis also revealed possible texture components and previous austenite grain boundaries. A new inspection to verify the characteristics was conducted using a Zeiss Sigma Field Emission Scanning Electron Microscope (FE-SEM).

5.1.3 Material strength

Previous tests have set the yield strength between 480 and 560 MPa at the test temperature. The varying estimates for the comparison data strengths are derived from hardness measurements and formulas (46-48),

$$\sigma_{flow} * \frac{3.5}{9.8} = HV \quad (46)$$

$$\sigma_{flow} = \sigma_{ys} \left[1 + \left(\frac{C_2}{\sigma_{ys}} \right)^2 \right] \quad (47)$$

$$HV = \frac{3.5\sigma_{ys}}{9.8} * \left[1 + \left(\frac{C_2}{\sigma_{ys}} \right)^2 \right] \quad (48)$$

where σ_{flow} is the flow stress of the material,
 HV is the hardness and
 C_2 is a material coefficient.

and actual tensile specimens from the sample material. The hardness derived strength formula is less relevant for the thesis samples as the hardness gradient is not present to the same extent in the sample piece. However, it is used for the comparison values produced by previous experiments (Lindqvist and Peltonen, 2021). The tensile tests were conducted by the Kungliga Tekniska högskolan (KTH) for a previous publication. Three tensile specimens were used for each testing temperatures, except four for 25 °C and two for -160 °C, Figure 13. (Boåsen, 2021.)

There is some unexpected deviation in the elastic region of specimen 804, which should be linear. The elongation was measured using a virtual extensometer and a proprietary TensileUn software not available for review for the thesis. The room temperature samples were measured using two sets of extensometers, but the build-up of frost at lower temperatures prevented their use for the – 85 °C samples reported by Boåsen (2021). The room temperature data was used to calibrate the virtual extensometer used for the cold test, which could explain the strange tensile behavior. Boåsen (2021) also discusses the uncertainties related to the measurements but concludes they should be reliable enough for the application (FEM material model) used in this thesis. In addition the elastic modulus value determined in the KTH report was used for the thesis calculations (213 GPa).

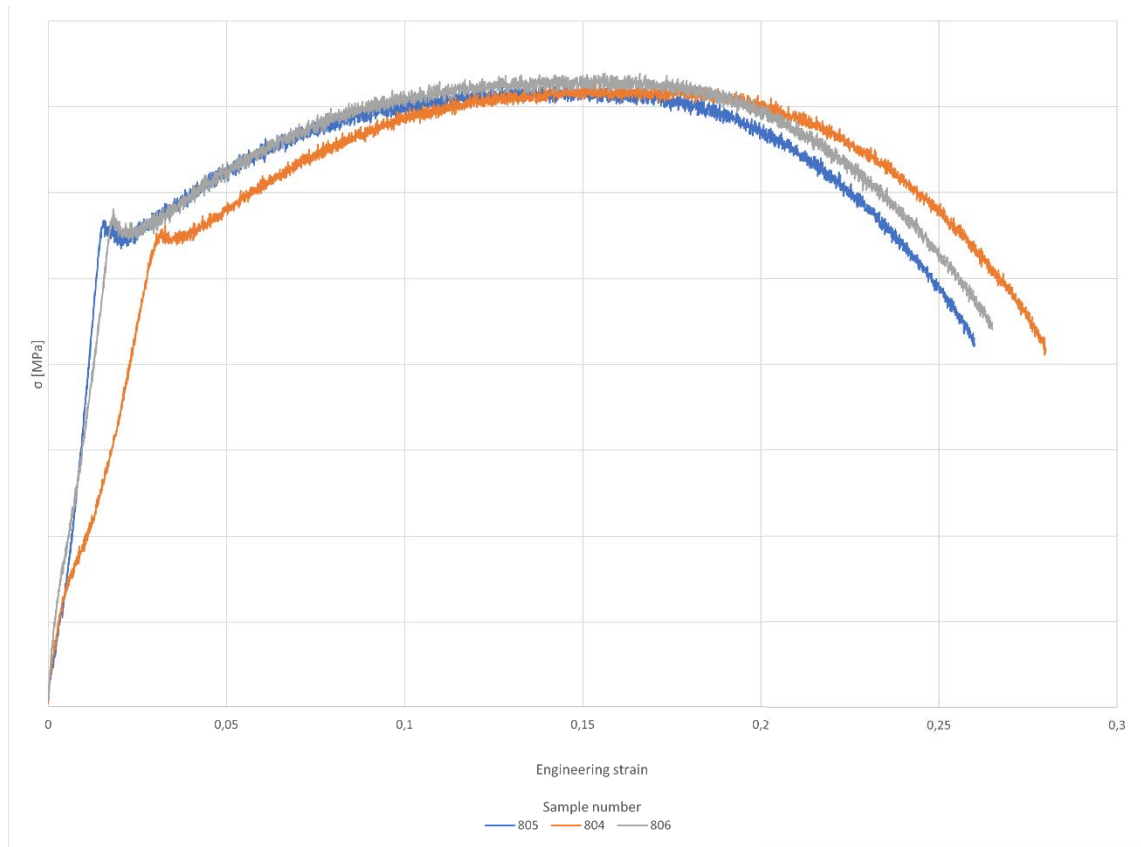


Figure 13 Stress-Strain curves for the tensile tests conducted at -85 °C.

The strain hardening behavior can be deduced from the tensile stress-strain graphs and KTH derived a hardening model for different temperatures by fitting an equation to the true stress-logarithmic strain data using the least squares method (49)

$$\sigma = \sigma_{ys} \left(1 + \alpha' \varepsilon_p + \beta' (1 - \exp(-\gamma' \varepsilon_p)) \right) \quad (49)$$

where α' , β' , and γ' are temperature related coefficients, and ε_p is the plastic strain.

with the coefficients according to temperature presented in Table 3.

Table 3 KTH stress formula temperature coefficients

| T [°C] | σ_{ys} [MPa] | α | β | γ |
|--------|---------------------|----------|---------|----------|
| 25 | 371,43 | 1,02 | 0,83 | 32,23 |
| -70 | 488,55 | 1,19 | 0,58 | 21,73 |
| -85 | 489,72 | 1,01 | 0,66 | 17,59 |
| -100 | 495,28 | 1,03 | 0,68 | 17,40 |
| -120 | 537,79 | 0,93 | 0,68 | 12,97 |
| -160 | 695,12 | 0,90 | 0,43 | 11,13 |

From the Swedish model, the Ramberg-Osgood relation (1) was used to deduce the strain hardening exponent n_{RO} for the plastic region of material behavior.

The Ramberg-Osgood formulation accepted by Abaqus CAE takes the following form:
(50),

$$\varepsilon = \frac{\sigma}{E} + \alpha_{RO} \frac{\sigma}{E} \left(\frac{\sigma}{\sigma_{ys}} \right)^{n_{RO}-1} \quad (50)$$

where $(n_{RO} = 9, \alpha_{RO} = 2.5)$.

The KTH model was plotted on a log-log scale where the linear fit slope represents the strain hardening exponent. The slope is not constant and the linear section which produced the best agreement between the simulation models and experimental data was chosen, Figure 14. The yield offset is determined using the same method. The results were also checked against the engineering stress-strain curves of the tensile experiments, Figure 15.

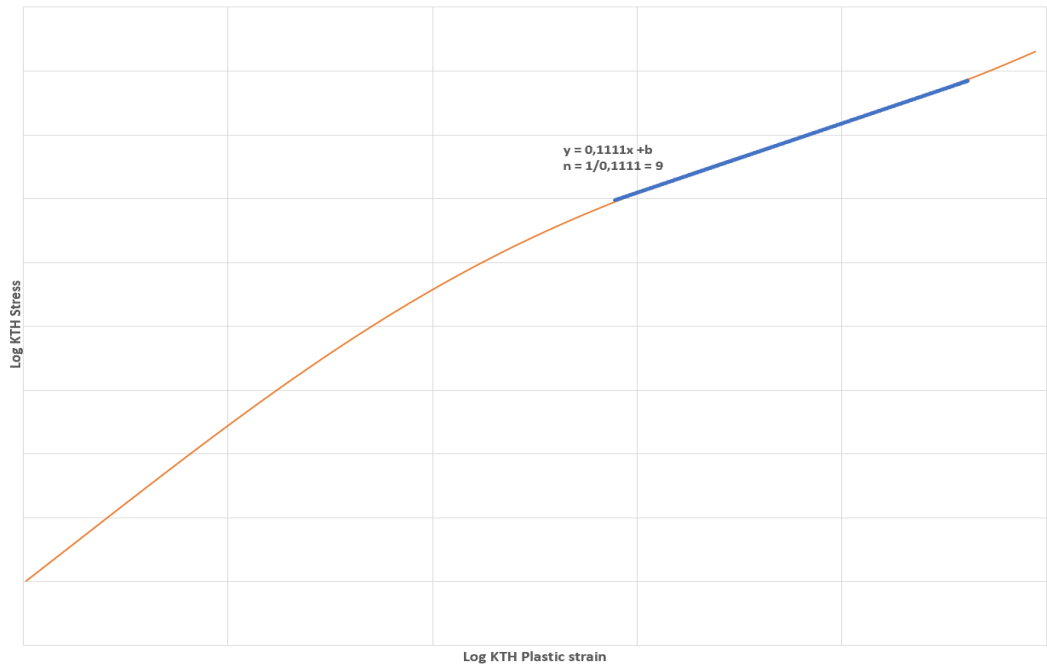


Figure 14 Log-Log True Stress-Strain graph for the determination of the Ramberg-Osgood strain hardening exponent.

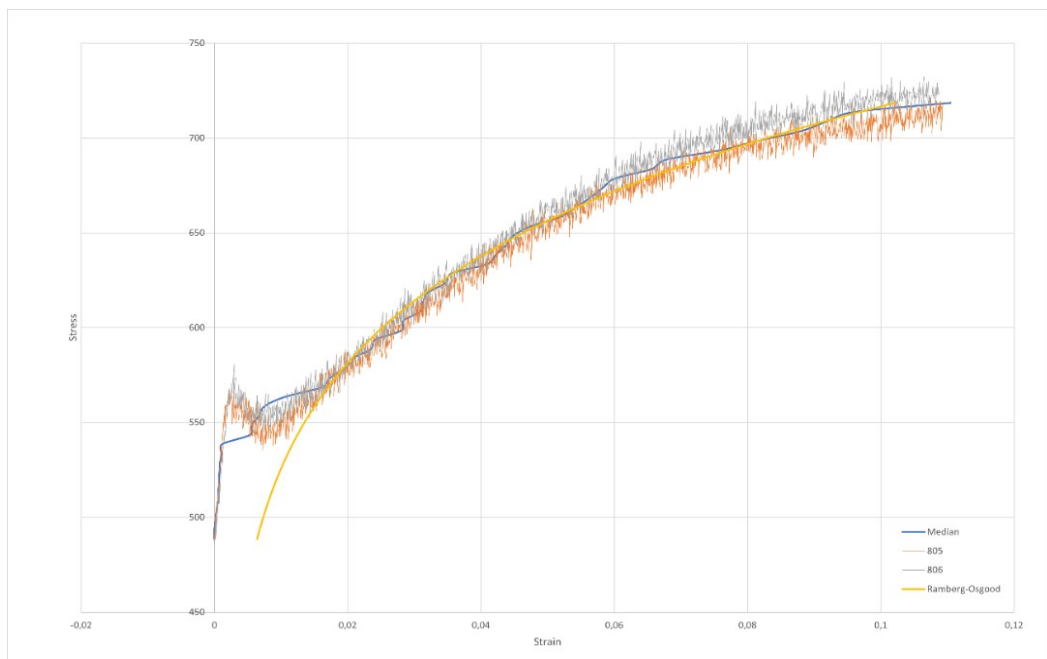


Figure 15 Ramberg-Osgood material model fitted through the plastic region of two tensile test experiments on an engineering stress-strain curve.

5.2 Sample detachment

Based on the aforementioned characterizations the sample piece was accepted and the detachment planned accordingly. The geometry parameters are inflexible which limited the extraction of the samples from the larger piece. The determining factor was the total length of 210 mm allowing only one direction for the sample longitude orientation. This left only the T-X directions available. As previous data is available from the T-L orientation and it is recommended in the JRQ manual (Brumovsky et al., 2001), it was chosen over T-S, Figure 16.

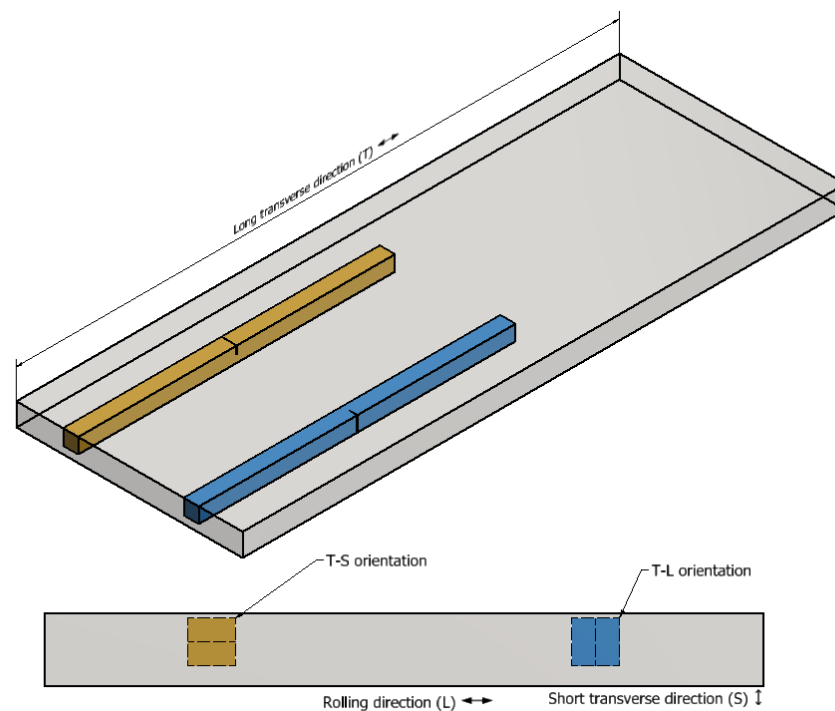


Figure 16. The sample material piece orientation and directions with the available sample examples, T-S in orange and T-L in blue.

EDM wire cutting was used to detach the samples. As there are two types of specimens, their removal order is altered to allow for the statistical evaluation compensation of the material inhomogeneity, Figure 17 and Figure 18.

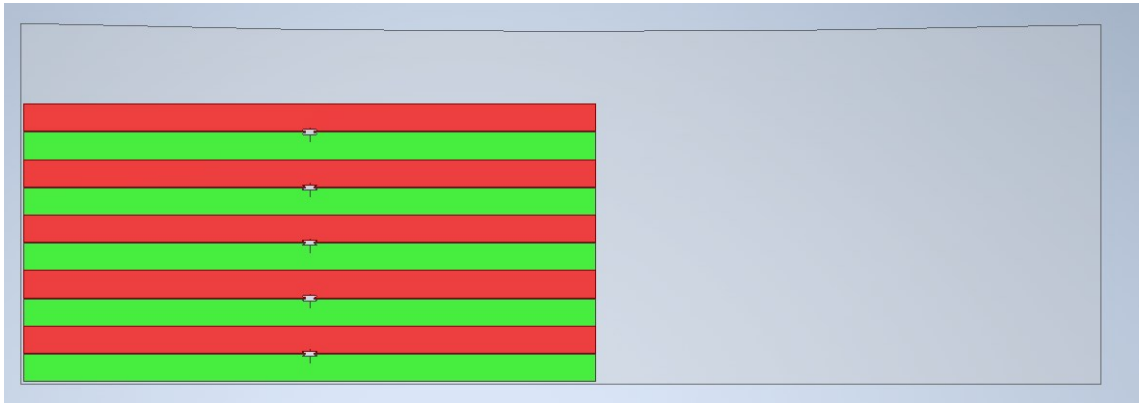


Figure 17. The sample removal from the same perspective as Figure 7, a/W 0.2 (Red), a/W 0.5 (Green).

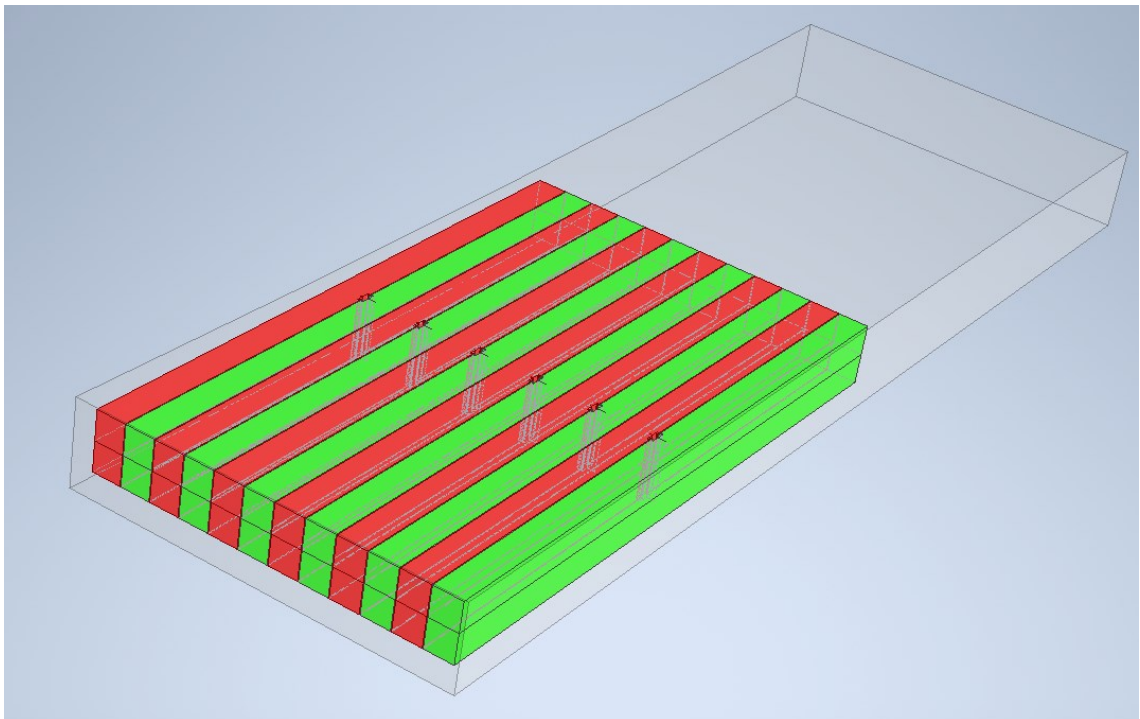


Figure 18. SE(N)T specimens in their removal locations from the larger material slab a/W 0.2 (Red), a/W 0.5 (Green).

5.2.1 Naming convention

The goal of the sample identification label is to tell where from the slab the sample was originally from, which sample is its pair and what type of sample it is. The samples were labeled on both sides of the crack with running numbers combined to a HC High constraint prefix for the a/W 0.5 samples and an LC low constraint prefix for the a/W 0.2 samples. The numbers increase in the rolling direction and from top to bottom.

All the sample labels and geometries can be seen from Appendix 1. The sample manufacturing was subcontracted to a specialized machine shop MEC(T)ALENT Oy.

5.2.2 Pre-cracking

To facilitate the use of fracture mechanics calculations, a sufficiently sharp crack is required (Anderson, 2017 p. 314). This was achieved through fatigue pre-cracking induced by cyclical loading. The pre-cracking was done by three-point bending where the distance between supports is $4W$ or 40 mm. Before the fatigue process was started, the sides perpendicular to the crack growth direction were polished to prevent any surface imperfections from growing during the pre-cracking. This can be seen in Figure 9. The loading ratio between the minimum and maximum forces was set at 0.1. The process was stress intensity controlled and as the crack grows the frequency resonance was used to estimate the progression. There are requirements set on the crack growth straightness that are evaluated from the fracture surfaces in section 5.4.2 as there were no gauges present during the fatiguing process. A recent study by Lindqvist and Kuutti (2022) indicates that the limitation set by the standards are not necessarily as critical as previously thought, but they were adhered to in the thesis experimentation.

5.2.3 Side grooving

Side grooves were machined using a Charpy V impact specimen notch profile tool, Figure 19. A Mitutoyo depth gauge was used to measure the depth of the side grooves, to ensure consistent machining process, but the measurement accuracy was lower than the machining precision. Ensuring that the gauge probe was perfectly at the bottom of the groove was inconsistent, but the manufacturing method appeared very repeatable.

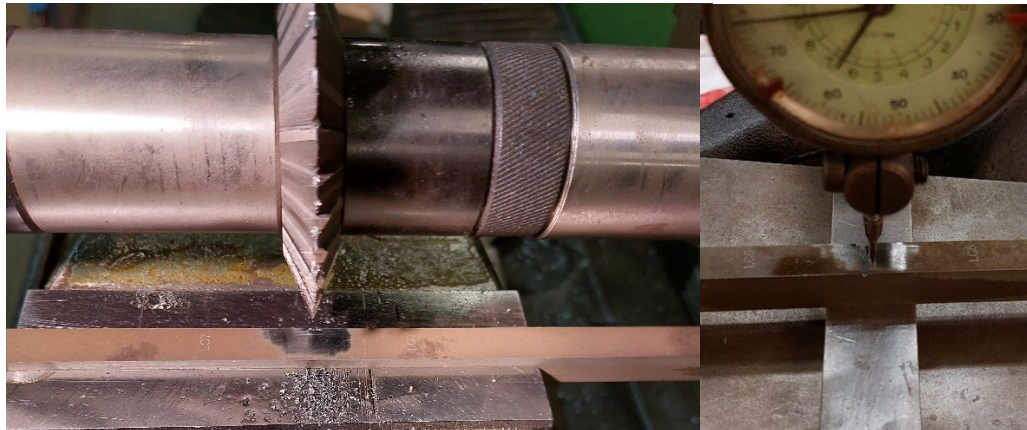


Figure 19 Side grooving equipment and a clock dial intended for Charpy V notch measurement used to guide the machining.

5.3 Test equipment

5.3.1 Load cell

If the limit load of the specimen is derived from the uncracked cross-sectional area and yield strength, around 50 -60 kN is needed to reach the yield stress. It is recommended that the load frame capacity exceed this value, even a few folds (CANMET, 2017). The 250 kN MTS-frame used in this thesis will suffice with this consideration in mind, but Weeks (2017) notes, that the best accuracy is received using a load cell close to the forces of the experiment.

5.3.2 Clamping

The clamps are wedge locking, and their compression increases with tensile load. The different methods for SE(N)T testing do not provide strict accuracy requirements for clamping as highlighted in a review by Weeks (2017), but the distance between clamps should be set as close as possible to $10W$. This was achieved by using the displacement controls of the load cell and driving the clamps to the exact correct displacement away from each other. The clamps are self-correcting and should align under tension, but any moments that arise from the alignment are unknown. A digital angle level was used to ensure the parallel attachment between the clamps, Figure 20. The crack was oriented to

cause opening moment in the stiffer rotational axis of the load cell, so that the machine flex would not allow for additional rotation.

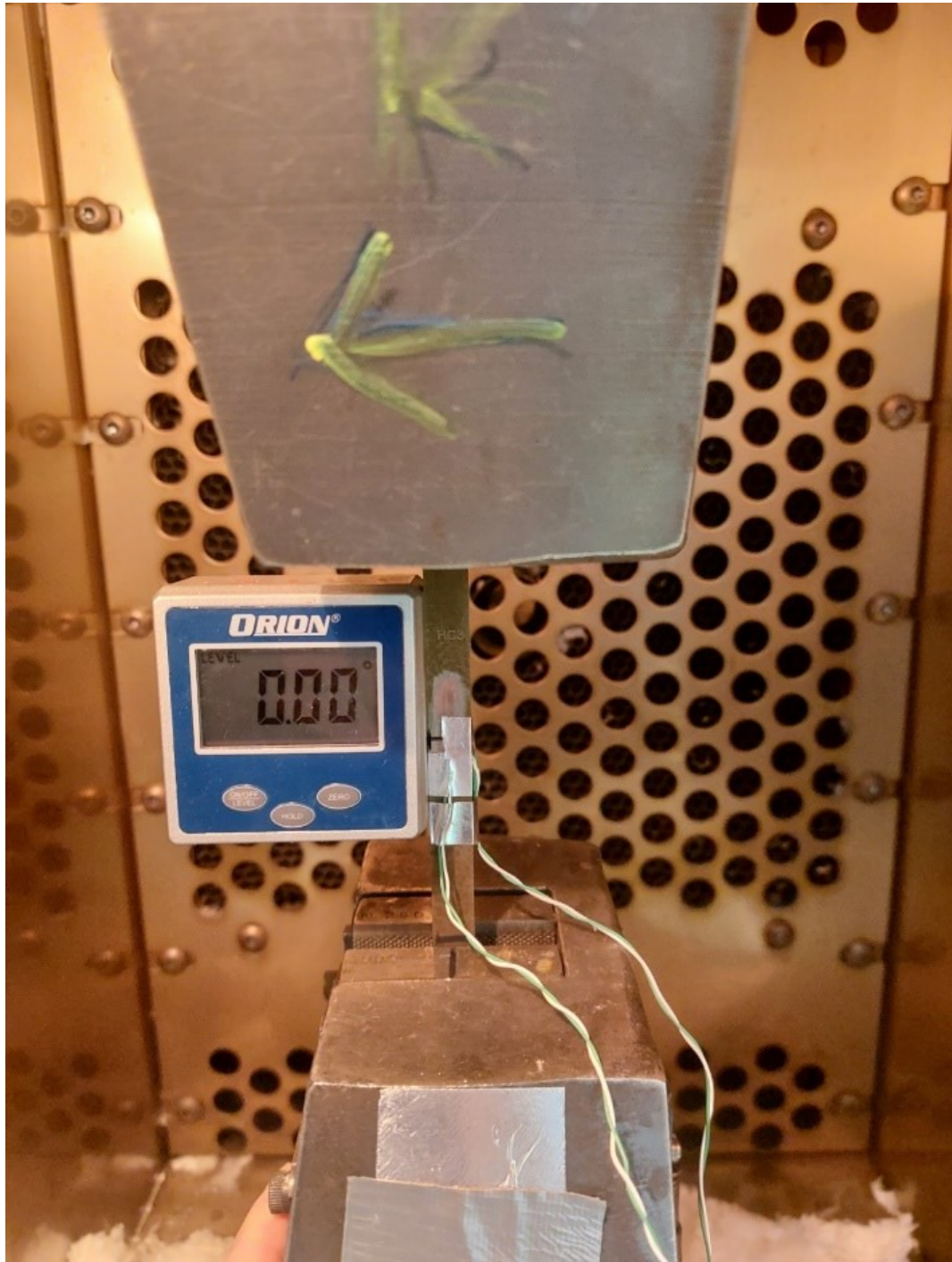


Figure 20 Example of the sample alignment using a digital level.

5.3.3 Temperature measurement and control

The standard ASTM E1921 recommends that the experimental temperature is set close to a temperature where the K_{Jc} is $100\text{MPa}\sqrt{\text{m}}$. For comparable SEB specimens, this temperature was determined to be close to $-80\text{ }^{\circ}\text{C}$. The test temperature was set at $-85\text{ }^{\circ}\text{C}$ as it provides a new datapoint from the more ductile region, where the effects of constraint are expected to be stronger (Sarzosá et al., 2018), but also contains ample comparison data and information of the material's physical behavior. The standard also dictates, that the fluctuations in temperature must stay within $\pm 1\text{ }^{\circ}\text{C}$ of the average during the experiment. To achieve this, the experiment was conducted in an environmental chamber cooled with liquid nitrogen. The chamber encloses the specimen and the attaching grips.

Temperature was measured with a type K thermo-couple connected to a data logger and software provided by MTS. The thermocouples are in contact with the sample material surface and were taped on rather than spot-welded to avoid the resulting HAZ from influencing the results. Additional non-logging thermo couples were used for verification and monitoring purposes. One probe was attached to the sample and the other to the clamp. The large metallic load cell is a massive heatsink and the clamp temperature was used to indicate the state of temperature equilibrium inside the chamber. The other two sensors were located near the crack. The logged temperature was taken from the side facing away from the cooler to avoid nitrogen plumes from blowing towards the thermocouple. This orientation was mostly for redundancy as the effect of the cooling flow was only present when the environmental chamber settings were changed, and a large flow of coolant was introduced, which was not done during ongoing measurements.

The chamber is insulated, but the hydraulic tension mechanism produces some heat. Therefore, the cooling temperature was set slightly below the target temperature to achieve equilibrium close to it. During cooling a small tensile force in the magnitude of 0.15 kN was applied to ensure good grip in the vise clamps. When the temperature of the machine and specimen were within five degrees Celsius the sample was assumed to have reached the target temperature. The samples were kept at the target temperature for around 30 minutes before experimentation to ensure the temperature gradient between the specimen surface, where measurements are taken, and the core was even. Another method

applied to verify consistent temperature, was to switch from load to displacement control at the final stages of cooling. When cooling from room temperature to $-85\text{ }^{\circ}\text{C}$ the thermal shrinkage would cause a stress of several kN if the machine was left on displacement control. With this in mind, if the machine was left on displacement control and the sample core was still warmer, a tension would arise as it cooled. As there was no thermal shrinkage during the hold period evident by the constant tension forces during displacement control, it can be assumed that the core surface matches that of the surface. This displacement control method was not repeated on all experiments, but it is assumed to validate the cooling procedure since the material and overall dimensions are the same.

The effect of the light on temperature was considered, but deemed insignificant. It is an incandescent bulb which would convert large amounts of its input energy of 220 W into heat, but reaching equilibrium would take this into account. The environmental chamber around the grips is pictured below in Figure 21.



Figure 21 A sample placed in the load cell grips with the CMOD gauge and temperature probes attached, and their locations revealed by wires.

5.3.4 Procedure followed

The progression of experiments was as follows:

1. The pre-cracked sample was cleaned with alcohol
2. The two temperature gauges were taped on next to the crack
3. Clamps were driven to a correct displacement
4. The sample was aligned and tightened in the clamps
5. Cooler was turned on and the load cell on force control with small tension
6. The machine and samples cooled and were kept at equilibrium for a minimum of 30 minutes
7. The gauges were reset
8. The sample was pulled apart at a rate of 2 mm/min
9. Sample was removed and submerged in alcohol to avoid condensation
10. Procedure was repeated for a new specimen

The first samples were used to find faults in the test procedures and evaluate any need for adjustment. It was noted that the samples slipped in the grips when placed there cold, so the clamped surfaces were roughed, Figure 22. Based on the first few specimens for each series the load rate was increased, but the temperature was kept at the preplanned -85 °C.

Many of the standard methods recommend an unloading compliance test to verify the stiffness of the machine. The loading-unloading forces should be lower than those used at the final phase of pre-cracking to prevent crack growth, but as they were applied, no tangible results were obtained. This was due to the small magnitude of forces used, and the unloading compliance loading cycle was therefore abandoned. For future reference it should be noted, that the machine tolerances do not scale with different sample sizes.



Figure 22 Roughing of the clamped region of the specimen to prevent slip.

5.4 Qualification requirements

5.4.1 Screening criterion

The number of uncensored results required is determined through the formula (51),

$$\sum_{i=1}^3 r_i n_i \geq 1 \quad (51)$$

where r_i is the number of uncensored valid specimens in a temperature range and n_i the weighing factor for the temperature range. The weighing factor is given in the standard ASTM E1921-21 Table 6. The thesis range requires six uncensored specimens.

5.4.2 Pre-crack qualification

The pre-crack straightness is measured through 9 points evenly placed, centered from the specimen centerline, and extending to 0.01 B from the notched free surface. The two edge measurements are averaged and then a second average is taken from this combined value and the 7 innermost measurements. This average value is the initial crack depth a_0 . The pre-crack is invalid if any of the inner seven measurements deviate more than the formula

(52) allows or if the pre-estimate of the pre-crack length differs from the average value by more than 5%.

$$a_i \neq a_0 \pm 0.1\sqrt{b_0BN} \quad (52)$$

where a_i is the crack the innermost seven measurement 2-8 value, and a_0 is the average crack depth.

An example of the measurement can be seen in Figure 35.

5.4.3 Quasistatic load-rate qualification

As the load rate effects the resulting toughness with slower rates resulting in tougher results, a limit is set on the allowable speeds. Anything between 0.1 and 2 is allowed with 1 producing ideal results. As the load rate is expressed as a function of the stress intensity over time it can only be found out after testing. First a few samples were pulled at a rate of 0.1 mm/min which was too slow. To keep comparison between the different specimens consistent, a single higher rate was chosen at 2 mm/min for all the tests which results in the a/W 0.2 specimens in having a loading rate of ~ 0.2-0.3 while the a/W 0.5 were closer to 1.

5.5 Fracture toughness calculations

All the fracture toughness and Master Curve calculations are done using the MATLAB script (MATLAB, 2022), truncated in Appendix 2.

For this thesis, the J-integral was interpolated from the load-displacement curve produced by fracture toughness testing, using the area under a curve fit of the CMOD and force data. A linear elastic material rebounds and forms a line on a stress-strain graph with a slope theoretically matching the Young's modulus of the material. However, a plastically deformed material is irreversibly changed and a strain can have different load conditions behind it, which means the conditions behind crack formation cannot be implicitly derived from the displacement. (Anderson, 2005.)

With this limitation in mind, the graph was divided into plastic and elastic portions using the assumption that the elastic portion is (mostly) linear in its load-displacement behavior, Figure 23.

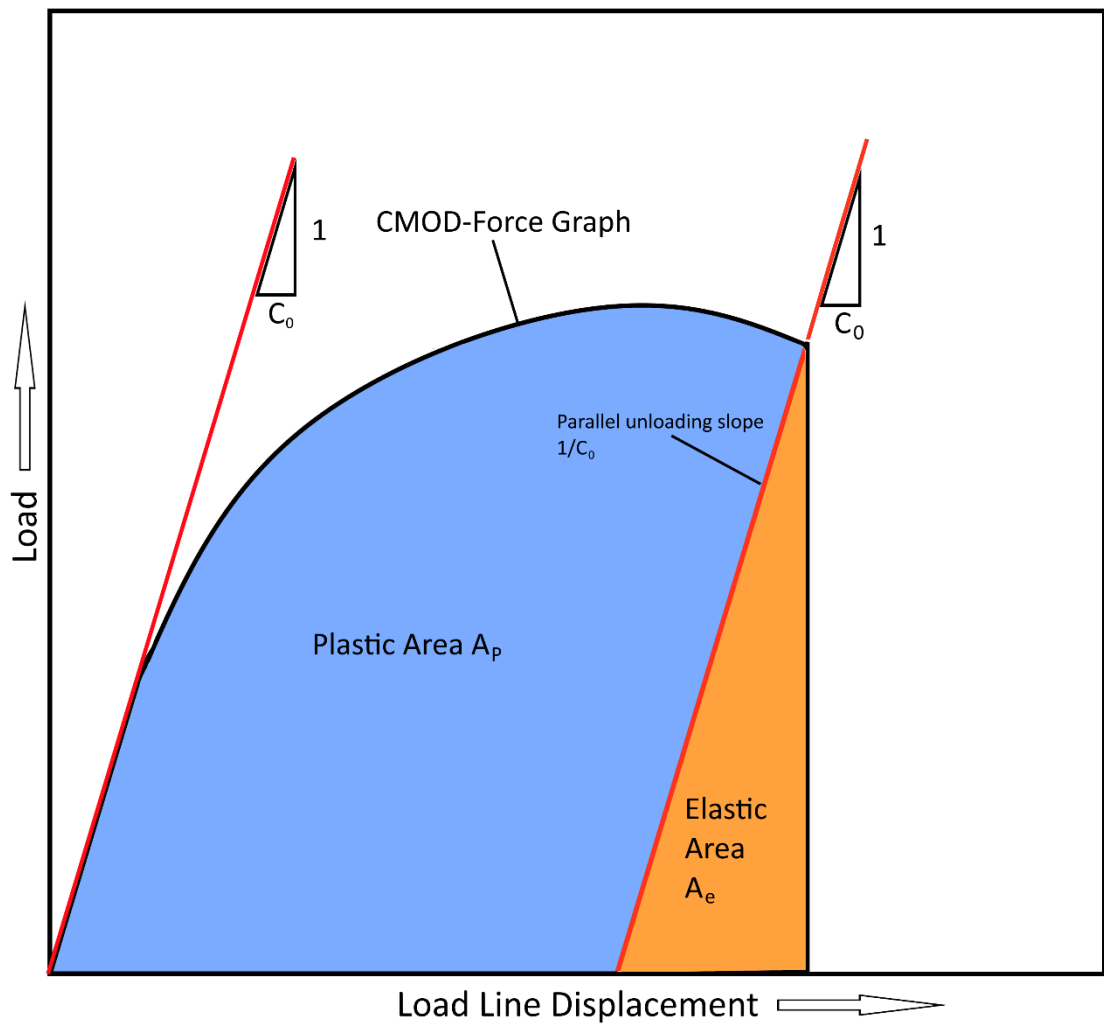


Figure 23 Illustration of the plastic and elastic areas under a CMOD-Force graph.

The J at the onset of critical failure is defined in the standard ASTM E1921 as presented below, (53-55)

$$J_c = J_e + J_p \quad (53)$$

$$J_e = \frac{(1-\nu^2)K_e^2}{E} \quad (54)$$

$$J_p = \frac{\eta A_p}{B_n b_0} \quad (55)$$

where J_c is the J-integral at cleavage fracture initiation,
 J_e is the elastic portion of the J-integral,
 J_p is the plastic portion of the J-integral,
 K_e is the elastic stress intensity factor,
 A_p is the plastic area under the CMOD-Force graph,
 b_0 is the remaining ligament,
 η is the Eta factor.

The plastic component of the J-integral J_p relies on the eta factor η , which is a nondimensional parameter conveying the plastic proportion of the J-integral independent of loading and quantify the plastic work done by the strain energy. (Ruggieri, 2012.)

Using this method requires accurate η estimates and there are many sources for different experimental configurations available. The different FEM analysis used to produce eta values often come with their own corresponding J_p formulas. In his paper, Ruggieri (2017) compared many of these different results for SE(N)T specimens. CANMET has also produced its own recommended procedure and values, which are used in this thesis, as it is the method previously used to produce the comparison data, (56)

$$\eta_{CMOD} = \sum_{j=0}^{10} \phi_j \left(\frac{a_j}{W}\right)^j = 1 - 1.089 \left(\frac{a_0}{W}\right) + 9.519 \left(\frac{a_0}{W}\right)^2 - 48.527 \left(\frac{a_0}{W}\right)^3 + 109.225 \left(\frac{a_0}{W}\right)^4 - 73.116 \left(\frac{a_0}{W}\right)^5 - 77.984 \left(\frac{a_0}{W}\right)^6 + 38.487 \left(\frac{a_0}{W}\right)^7 + 101.401 \left(\frac{a_0}{W}\right)^8 + 43.306 \left(\frac{a_0}{W}\right)^9 - 110.770 \left(\frac{a_0}{W}\right)^{10} \quad (56)$$

where η_{CMOD} is the CANMET Eta factor.

The values for the eta parameters were validated using the reference results for a/W 0.2 and 0.5 provided in the CANMET recommended practices which were an exact match. Ruggieri (2017) also notes that eta values based on CMOD are stable across different Ramberg-Osgood strain hardening exponent.

The elastic stress intensity and geometric factors were also provided by CANMET, (57 and 58), and are valid for the specimen a/W regions.

$$K_e = \frac{F\sqrt{\pi a_0}}{W\sqrt{BB_N}} f\left(\frac{a_0}{W}\right) \quad (57)$$

$$f\left(\frac{a_0}{W}\right) = 1.197 - 2.133 \left(\frac{a_0}{W}\right) + 23.886 \left(\frac{a_0}{W}\right)^2 - 69.051 \left(\frac{a_0}{W}\right)^3 + 100.462 \left(\frac{a_0}{W}\right)^4 - 41.397 \left(\frac{a_0}{W}\right)^5 - 36.127 \left(\frac{a_0}{W}\right)^6 + 51.215 \left(\frac{a_0}{W}\right)^7 - 6.607 \left(\frac{a_0}{W}\right)^8 - 52.322 \left(\frac{a_0}{W}\right)^9 + 18.574 \left(\frac{a_0}{W}\right)^{10} + 19.465 \left(\frac{a_0}{W}\right)^{11} \quad (58)$$

where f is a geometric factor of the specimen,

F is the load, and

B is the initial specimen width.

The fit function used for the area calculations is produced with an eight-degree polyfit through the measurement data, which produces a polynomial function that describes the datapoints through the least squares method, (59)

$$fit = p_1x^8 + p_2x^7 + p_3x^6 + p_4x^5 + p_5x^4 + p_6x^3 + p_7x^2 + p_8x + p_9 \quad (59)$$

where the p's are the polynomial coefficients.

The area under the fit function (59) represents the energy required for the cracking and was found by integrating the fit function, (60 and 61).

$$Area = \int_0^{CMOD_{max}} fit \frac{dy}{dx} \quad (60)$$

$$A_p = Area - A_e = \int_0^{CMOD_{max}} fit \frac{dy}{dx} - \frac{F_m^2 C_\theta}{2} \quad (61)$$

where Area is the total are under the CMOD-Force graph,
 A_e is the elastic area under the CMOD-Force graph,
 F_m is force at maximum CMOD,
 C_θ is the slope reciprocal for the elastic gradient, and
 $CMOD_{max}$ is the largest opening value and upper boundary.

Several methods were considered to determine the linear portion slope (C_θ) which was used to calculate the plastic and elastic proportions under the fit function The best agreement was found using the assumption that the strain must initially be elastic before plastic deformation. Therefore, the strain-stress slope should be the highest before yielding, as the force required for the same strain increment will be lower after plasticity is reached. Using this assumption, the highest strain-stress relations must be from the elastic part. Removing deviations from the load initiation and extreme values to remove outliers the 90th to 98th % quintile average produced gradients that closely matched the slopes observed from plotting the datapoints. This range was adjusted and validated visually to find the greatest degree of agreement between the calculation and measured data and then used for the thesis fracture toughness calculations.

The J-Integral was converted to a toughness value through formula (62)

$$K_{Jc} = \sqrt{J_c \left(\frac{E}{1-\nu^2} \right)} \quad (62)$$

and normalized to a 1T size with formula (63)

$$K_{Jcx} = 20 + [K_{Jc} - 20] \left(\frac{B}{25.4} \right)^{0.25} \quad (65)$$

Where K_{Jcx} is the median K_{Jc} toughness.

Alternatively, (66)

$$K_{Jcx} = 20 + \left[\sqrt{\left(\frac{\eta \left(\frac{A - C_0 P^2 m}{2} \right)}{BN(W - a_0)} \left[1 - \frac{\gamma l l d a_0}{W - a_0} \right] + \frac{(1 - \nu^2) \left(\frac{P \sqrt{\pi a_0}}{W \sqrt{B B N} f} \right)^2}{204 - \frac{T}{16}} \right) \left(\frac{204 - \frac{T}{16}}{1 - \nu^2} \right) - 20 \right] \left(\frac{B}{25.4} \right)^{\frac{1}{4}} \quad (66)$$

which was tested to produce the same value as the substitute parts separately. The combined formula is used in the uncertainty and sensitivity analysis in section 5.7.

5.5.1 Derivation of the T_0 temperature

The standard recommends iteration to find the T_0 temperature by balancing the following sum formula in respect of T_{0Q} , which is a preliminary value used to substitute the unknown T_0 , but a symbolic solver was used in the thesis calculations, (67)

$$\sum_{i=1}^n \left(\frac{\exp[0.019(T_i - T_{0Q})]}{(11 + 77 \exp[0.019(T_i - T_{0Q})])^5} \right) - \sum_{i=1}^n \frac{(K_{Jci} - 20)^4 \exp[0.019(T_i - T_{0Q})]}{(11 + 77 \exp[0.019(T_i - T_{0Q})])^5} = 0 \quad (67)$$

T_{0Q} is accepted as T_0 if the number of tests produced within an acceptable range between the test and T_0 temperature set in 5.4.1.

5.5.2 Master curve graphs

The Master Curve K_0 was calculated using formula (68),

$$K_0 = \left[\sum_{i=1}^N \frac{(K_{Jcx(i)} - 20)^4}{Nu} \right]^{\frac{1}{4}} + 20 \quad (68)$$

where N_u is the number of uncensored specimens and N is the number of specimens. Substituting the resulting K_0 into (69) produces the median toughness value,

$$K_{Jc(med)} = 20 + 0.91(K_0 - 20) \quad (69)$$

and graphing this over a range of temperatures was used to produce the median Master Curve (70)

$$T_{0med} = T - \left(\frac{1}{0.019}\right) \ln \left(\frac{K_{Jc(med)}^{-30}}{70}\right) \quad (70)$$

The probability ranges were set by substituting xx in (71) with the desired range,

$$K_{Jc(0.xx)} = 20 + \left[\ln \left(\frac{1}{1-0.xx}\right)\right]^{\frac{1}{4}} \{11 + 77 \exp [0.019(T - T_0)]\} \quad (71)$$

and plotting the results over a range of temperatures was used to produce the confidence interval graphs.

5.6 Abaqus CAE

Compared to the simple, almost linear relation of the T_0 shift and T-stress, the Q-parameter requires a Finite Element Method (FEM) analysis of the actual crack tip conditions, and for this thesis, Abaqus CAE 2022 was used (Dassault Systemes SIMULIA Corp., 2022).

The magnitude of the Q-parameter was derived by comparing the models S_{22} stress to the HRR reference stress at the distance normalized with formula (37), and substituting the values into formulas (38) and (39).

Approximations for the coefficients I_n and $\tilde{\sigma}$ for formula (39) were calculated with formulas found in (Wallin, 2011 p. 18), (72 and 73)

$$I_n \approx 4.35 + 2.7 \exp \left(-\frac{n_{RO}}{3.6}\right) \quad (72)$$

$$\tilde{\sigma}(\theta = 0, n_{RO}) \approx 2.66 - 1.457 \exp\left(-\frac{n_{RO}}{4.295}\right) \quad (73)$$

for plane strain conditions.

The shift in T_0 temperature between the specimens was quantified using a refined version of formula (40) by. (Moattari & Sattari-Far, 2017) adjusted by Lindqvista and Kuutti (2022), (74).

$$\Delta T_0 = T - 40(Q - Q_{ref}) \quad (74)$$

where the Q_{ref} parameter is the Q from a a/W 0.5 C(T)-specimen modelled from the same material.

The exact values needed can be picked from the Abaqus history and field outputs in tabular form after each case has been computed.

Two new models, one for each specimen geometry, were constructed for the Q -parameter comparison and the Q_{ref} reference C(T) model was derived from a pre-existing simulation compiled by Juha Kuutti. The geometry was limited to two dimensions to avoid any stress gradient related variations which would be present in a model of finite thickness. The geometries of the models follow the ones presented in the technical drawings of Appendix 1.

, with the exception of being mirrored on the crack plane through a symmetry constraint and extended crack depths to match the average measured for each specimen type. The modelling was conducted with the theoretical crack depths of 2 and 5 mm as well, but the remodeling with measured values greatly improved the agreement with the test results, especially for the a/W 0.5 model.

5.6.1 Material model

The material was modelled as deformation plastic with a Poisson's ratio of 0.3, Young's modulus of 213 GPa, strain hardening exponent of 9, and yield offset of 2.5. The strain

hardening parameters were derived from the KTH model presented in section 5.1.3. The yield strength used was 488 MPa, which is from the KTH material model. This number corresponds to the lower yield point for the material and smooths the stress strain curve by removing the spike caused by an upper yield point, Figure 15. Abaqus does not have units within itself, and the variables were scaled to match the use of mm with all geometry lengths. An elastic, and a von Mises material model were also evaluated as comparison results. The elastic model deviated significantly, while the von Mises followed the deformation plastic results quite closely, only deviating at larger plasticity displacements.

5.6.2 Features, load, and constraint

The loading was done through a forced displacement conveyed through a reference point to the clamp surfaces, Figure 24. The displacement was ramped from zero to one in a linear fashion in the Y direction. Use of the reference point also allows for a single point source for the force derivation.

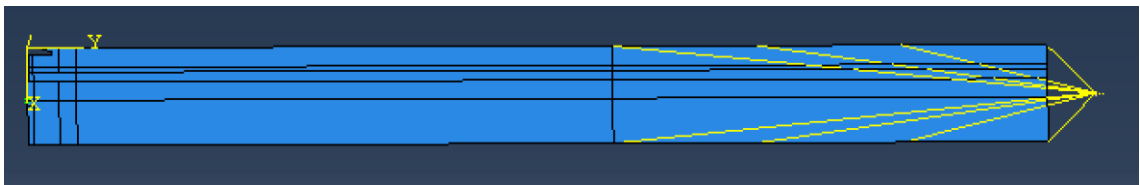


Figure 24 Yellow lines extending from the clamp surfaces to a reference point used for the displacement control.

The specimen was “mirrored” through an Y symmetry constraint along the remaining ligament. The constraint reflects the geometry on a plane with Y as its normal, restricts Y direction displacement, and rotation around the X and Z axes. In addition, a point constraint at the corner restricting movement in the X direction was used to prevent the part from leaving its starting origin, Figure 25.

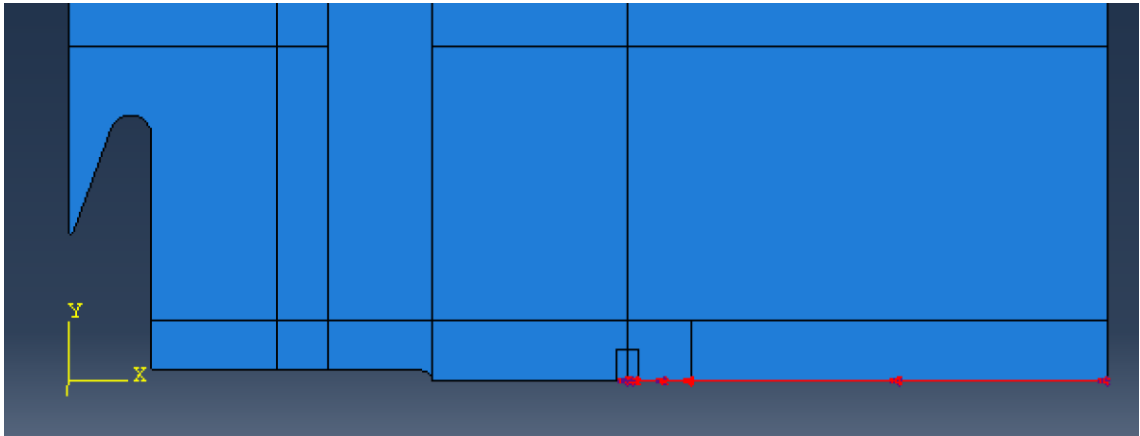


Figure 25 The Y-symmetry constraint and point constraint shown in red.

The J-integral was calculated using a crack-engineering feature which was placed at the edge of the Y-symmetry constraint. The crack growth direction was defined with a q-vector (1,0,0) and assumed to follow the symmetry plane.

The CMOD values were taken from the tip of the knife edge, and the X and Y components summed using Pythagoras theorem. The result was doubled as the model represents only half of the displacement, (75), Figure 26

$$CMOD = 2\sqrt{U_1^2 + U_2^2} \quad (75)$$

where U_1 is the X and U_2 the Y displacement.

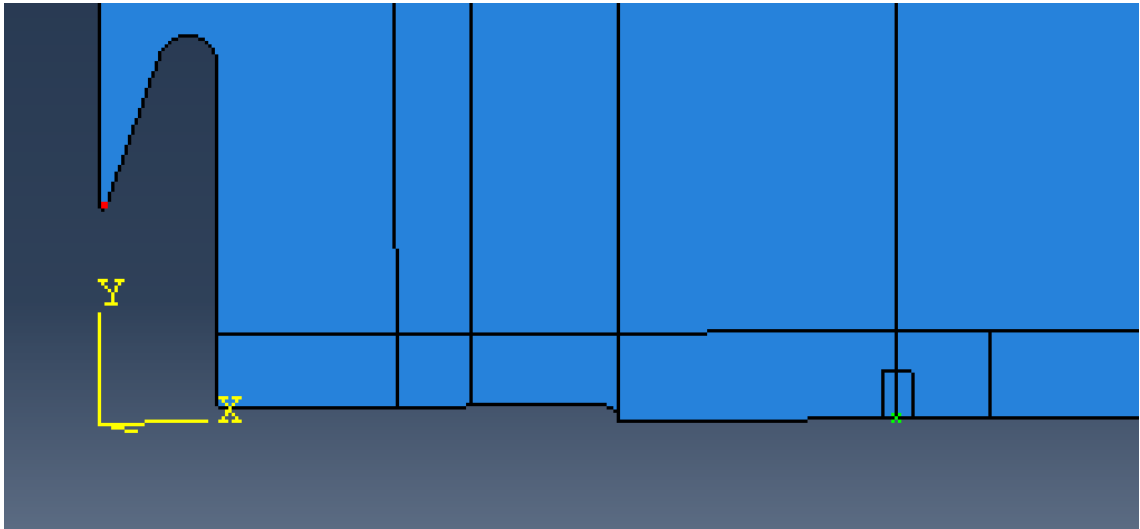


Figure 26 Red point illustrates the CMOD reference point and green X the Crack feature.

5.6.3 Mesh

Different meshes were experimented with, and a local refinement around the crack tip was used to improve the model accuracy. Mesh refinement resulted in earlier crashing of the model, and when the results were overlaid to those produced by a rougher mesh, no significant difference was found. As the rougher mesh allowed the model to function further, it was deemed acceptable. The results from elements in the immediate vicinity of the crack tip are suspect, as the mesh deformation was strong there. The elements at the crack tip had a size of 0.01 while the largest on the shaft of the specimen had a size of 0.5. A square aspect ratio was used for the elements at the crack tip, while more elongated rectangles were accepted for the shaft section, Figure 27.

The element type used was a plain strain CPE4R: A 4-node bilinear- plane strain- quadrilateral- reduced integration- hourglass controlled element. Different elements were experimented with, but no significant differences relevant to the study were observed. As the elements distort heavily, the locking prevention of reduced integration was considered beneficial. The possible stiffness singularities were prevented by using hour-glassing control. Better results could be obtained using adaptive remeshing which would replace and eliminate highly distorted elements at the crack tip. However, this was beyond the

scope of this thesis, and the J-integral was calculated from a contour outside the heavy distortion. The normalized radius for the S_{22} stress in front of the crack tip resulting from the J-values seen in the experimented results was also large enough to bypass the distorted regions.

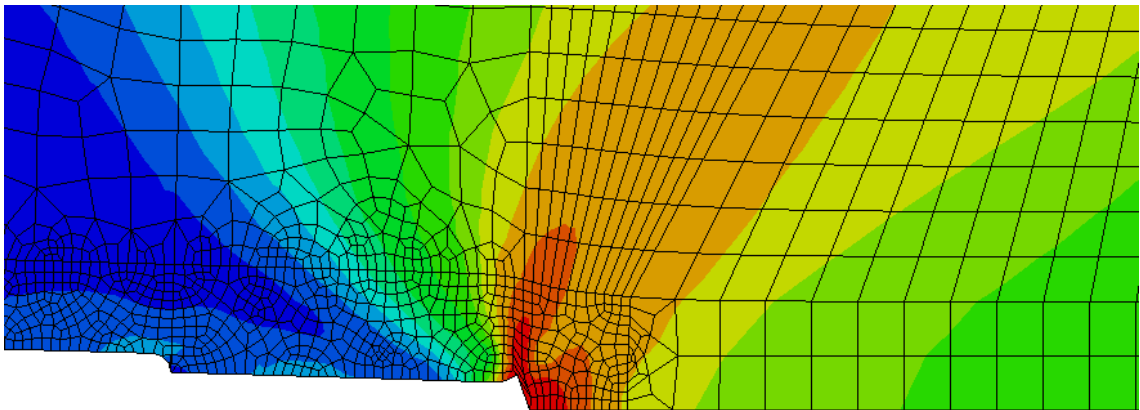


Figure 27 Distorted mesh at the crack tip displaying von Mises stress contours.

The maximum step size was set at 0.01 and minimum was 10^{-8} . This was done to achieve high enough resolution to use linear interpolation to correlate stress and J-integral values between the model's calculation points.

5.7 Result uncertainty evaluation

In his review on the SE(N)T techniques and procedures, Weeks (2017) states that uncertainty values for fracture toughness values are rarely reported due to the complex calculations and measurements behind them. In this thesis the following attempt is made to give the reader estimations on the reliability of the results presented, but further studies are needed to produce and evaluate an authoritative method for fracture toughness uncertainties produced by SE(N)T specimens. The uncertainty sources for the toughness values presented in this thesis can be roughly divided into the experimental measurement

uncertainties and the uncertainties related to the assumptions behind the Master Curve method. The effect on the T_0 bounds is done with a margin adjustment following equation (76),

$$\sigma_{stdv} = \sqrt{\frac{\beta_{uc}^2}{n} + \sigma_{meas}^2} \quad (76)$$

where σ_{stdv} is the standard deviation of the T_0 margin uncertainty,
 β_{uc} is a sample size uncertainty factor related to the method,
 n is the number of experiments, and
 σ_{meas} is the measurement uncertainty.

The standard's calibration requirements allow for the substitution of 4 for the measurement uncertainty.(ASTM International, 2021.) However, in this thesis the method used to derive T_0 from the measured CMOD and force values is not strict to any single standard. As such, the uncertainty ranges guaranteed by the methods described by the standards were estimated separately. A widely recognized estimation for measurement uncertainty and sensitivity analysis is the method detailed in the report by the Joint Committee for Guides in Metrology (JCGM) (2008) and its supplement 1, (Working Group 1 of the Joint Committee for Guides in Metrology, 2008b). This reference is commonly known as GUM 2008 in related literature, for example Weeks (2017) hints at a future publication reviewing such methods, but none could be found at the time of writing.

5.7.1 Measurement uncertainty

All measured results are estimates of the actual measurand and incomplete without the uncertainty accompanying that estimate (JCGM, 2008). Faults in measurement give rise to errors. The error can be random or systematic. Both types can be lowered through increased experiment counts, and the standard uncertainty through calibration. All the measurement devices used in this thesis have been calibrated by accredited parties to minimize bias in their reported results. In addition to the types of errors inherent to the measuring process, there is an additional uncertainty associated with the estimated results due to random effects and imperfect corrections of the aforementioned errors.

Each of the different measurements have their own associated uncertainties and distributions. These uncertainties and distributions can be evaluated either empirically through the measured datapoints if they are sufficient in quality and quantity or by experience on the measurement devices and its capabilities. Previous data can also be used as a basis of measurement uncertainty assessments if they are produced by a reasonably similar test set-up. (Dally, 2008; JCGM, 2008) The following formulas (77 and 78) for estimating the different types of uncertainty can be found in (Working Group 1 of the Joint Committee for Guides in Metrology, 2008a)

$$s^2(q_k) = \frac{1}{n-1} \sum_{j=1}^n (q_j - \bar{q})^2 \quad (77)$$

$$s^2(\bar{q}) = \frac{s^2(q_k)}{n} = \frac{\sigma_{stddev}^2}{n} \quad (78)$$

where $s(\bar{q})$ is the experimental standard deviation,
 q_k is the measured observation,
 q_j is the indexed measured observation, and
 \bar{q} is the mean of measured values

were used in the thesis uncertainty estimation.

In addition, the random type B uncertainty of the measuring devices must be added to the experimental uncertainty and was obtained from the calibration documents of the measurement devices. For the thesis estimates, the independence of the uncertainties per the law of propagation of uncertainty was assumed, and the simplified solution which is to add the random uncertainty divided by the square root of the trial count n was used. (JCGM, 2008)

Unlike the different types of uncertainties for the same measurement, uncertainties of different measurands cannot simply be added to each other as they have varying overall effects on the final output calculated. If an output is derived through a model and multiple measured input parameters, which is the case for the fracture toughness values, the

combined standard uncertainty can be estimated through the use of partial derivatives. The following formulation was developed for the thesis estimations:

Let

y be an estimate of the measured Y

where Y is a combination of measured x_1, x_2, \dots, x_n through a functional relationship

$$Y = f(x_1, x_2, \dots, x_n)$$

The functional relationship for fracture toughness measurements was condensed into a single formula as follows, (79)

$$K_{jcx} = \sqrt{\left[\left(\frac{\eta \left(A - \frac{C_0 P^2 m}{2} \right)}{BN(W-a_0)} + \frac{(1-\nu^2) \left(\frac{P \sqrt{\pi a_0}}{W \sqrt{BBN}} f \right)^2}{204 - \frac{T}{16}} \right) \left(\frac{204 - \frac{T}{16}}{1-\nu^2} \right) \right]} \quad (79)$$

, $Y = f(x_1, x_2, \dots, x_n)$ can be understood as K_{jcx} and

$$f(x_1, x_2, \dots, x_n) = f(A, C_0, P, W, B, BN, a_0, T, \nu,)$$

The combined standard uncertainty of y , $u_c(y)$, is the positive square root of the combined variance (80)

$$u_c^2(y) = \sum_{i=1}^n \left(\frac{\partial f}{\partial x_i} \right)^2 u^2(x_i) \quad (80)$$

where $u^2(x_i)$ is either a type A or B uncertainty for each variable derived from the methods described in 4.2 and 4.3 sections of the JCGM (2008) report, formulas (77 and 78).

The partial derivatives

$$\frac{\partial f}{\partial x_i}$$

are called sensitivity coefficients, and they reflect the sensitivity of output Y to changes in any particular x_i in question. As the system is nonlinear to a significant degree, higher order terms and interactions were considered. The following formula contains the most important terms for normally distributed input variables. The increased complexity (f') required the reduction of the number of variables considered for this type of uncertainty and the remaining measurement values used are presented in the combinations, (81-85)

$$\sum_{i=1}^n \sum_{j=1}^n \left[\frac{1}{2} \left(\frac{\partial^2 f}{\partial x_i \partial x_j} \right)^2 + \frac{\partial f}{\partial x_i} \frac{\partial^3 f}{\partial x_i \partial x_i \partial x_j^2} \right] u^2(x_i) u^2(x_j) \quad (81)$$

and $count f' = nCr_k^n + n * (n - 1) \quad (82)$

$$\sum_{i=1}^n \sum_{j=1}^n \left[\frac{1}{2} \left(\frac{\partial f}{\partial x_i} \left(\frac{\partial f}{\partial x_j} \right) \right)^2 + \frac{\partial f}{\partial x_i} \left(\frac{\partial f}{\partial x_i} \left(\frac{\partial^2 f}{\partial^2 x_j} \right) \right) \right] u^2(x_i) u^2(x_j) \quad (83)$$

with the combinations of parameters i and j being

$$\frac{1}{2} \left(\frac{\partial f}{\partial x_i} \left(\frac{\partial f}{\partial x_j} \right) \right)^2 : \begin{matrix} a_0' & W' \\ a_0' & B' \\ a_0' & T' \\ a_0' & A_p' \\ W' & B' \\ W' & T' \\ W' & A_p' \\ B' & T' \\ B' & A_p' \\ T' & A_p' \end{matrix} \quad (84)$$

$$\left(\frac{\partial f}{\partial x_i} \left(\frac{\partial f}{\partial x_j} \left(\frac{\partial f}{\partial x_k} \right) \right) \right) : \begin{matrix} a_0'W'' & a_0'B'' & a_0'T'' & a_0'A_p'' \\ W'a_0'' & W'B'' & W'T'' & W'A_p'' \\ B'a_0'' & B'W'' & B'T'' & B'A_p'' \\ T'a_0'' & T'B'' & T'W'' & T'A_p'' \\ A_p'a_0'' & A_p'B'' & A_p'T'' & A_p'W'' \end{matrix} . \quad (85).$$

The combined formula for standard uncertainty including higher order terms then takes the form (86)

$$u_c^2(y) = \sum_{i=1}^n \left(\frac{\partial f}{\partial x_i} \right)^2 u^2(x_i) + \sum_{i=1}^n \sum_{j=1}^n \left[\frac{1}{2} \left(\frac{\partial f}{\partial x_i} \left(\frac{\partial f}{\partial x_j} \right) \right)^2 + \frac{\partial f}{\partial x_i} \left(\frac{\partial f}{\partial x_i} \left(\frac{\partial^2 f}{\partial^2 x_j} \right) \right) \right] u^2(x_i) u^2(x_j) \quad (86).$$

The assumption of normal distribution is reasonable for the types of measurements being conducted, and for example a histogram of the temperature measurements follows a bell curve. The force measurements follow a linear distribution, but the individual force values are assumed to follow normal distribution. Similar assumptions were extended to the rest of the measurands.

To calculate all the combinations of different order interactions is challenging as the number of sums and terms within them increases in high dimensional systems.

Correlation between the variables further increases the complexity. To avoid the increased complexity and the lack of covariance data, some of the variables can be dropped or combined into a single parameter with a separate estimate of uncertainty. This lowers the accuracy of the uncertainty estimate, but a safety factor can be assessed and applied so that the resulting uncertainty will contain the effects of the dropped parameter by overestimating the overall uncertainty. For this thesis the uncertainty is magnified by an additional $\pm 10\%$. To give validity to this method, the uncertainties neglected should be small in magnitude and their effect assessed through complimentary analysis. When each of the higher order terms is evaluated, only a few have a significant effect on the overall uncertainty. The most significant factor seems to be the plastic area uncertainty. It is unfortunately also the most subjective uncertainty to evaluate since the magnitude

assigned depends on human interpretations of the plastic area slope and data filtering. The formulas (60 and 61) with which the plastic area is estimated is problematic for a multitude of reasons.

To give a liberal estimate of the plastic area (A_p) uncertainty, the many individual measurements which form the CMOD-Force graph are assumed to have a maximum reasonable cumulative uncertainty leading to an over estimation of the area under the graph. The area is estimated through integration of the polynomial fit function through the datapoints, which results in an averaging of the noise in measurement data. To validate the integrated area-estimate a second method of summing the incremental CMOD-Force slices between the datapoints is used to produce a “true” area under the datapoints which is incremental in nature. The two methods are demonstrated in a simplified manner below, Figure 28.

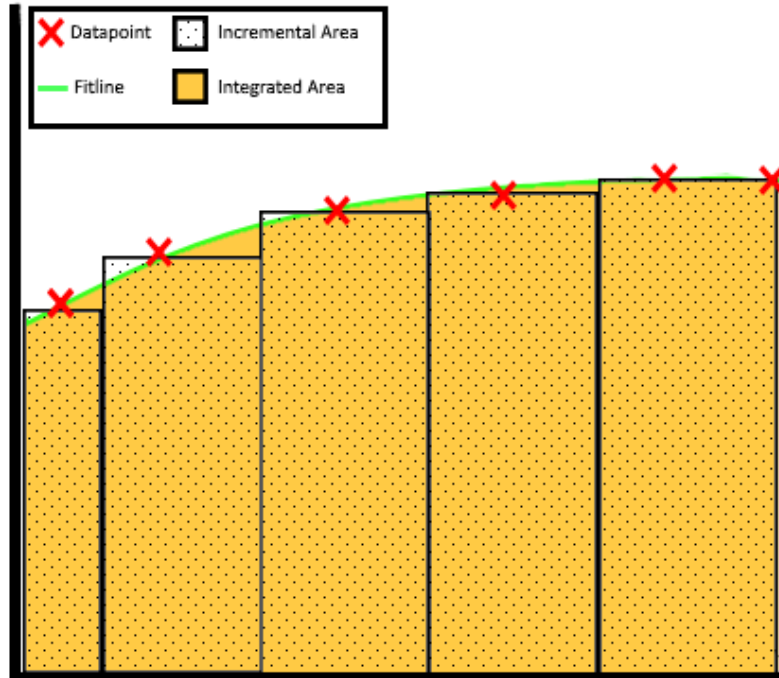


Figure 28 The two different methods for finding the area under the CMOD-Force graphs, the smooth orange area represents the integrated area while the dotted rectangles are summed to form the incremental area.

The difference between these two areas is then added as a systematic error to the area uncertainty estimate. The plastic area is what is left when the elastic portion is subtracted from the total area, but the elastic area is related to the gradient C_0 which is derived from a gradient fit under subjective estimation. Another problem with the gradient estimation is the covariance between the measurands it is derived from. A more thorough explanation of this covariance can be found in the review of Weeks (2017) Covariance factors increase the complexity of the error propagation significantly and the values needed for their accurate estimation are unknown. That is why the liberal estimation for the plastic area estimation is used as a substitute.

Even still, if the standard uncertainty function with the simplifying assumptions is evaluated using the MATLAB script, Appendix 2, due to the high order and large number of equations, the full expression would add ~70 000 characters, 250 pages, if included in this thesis as an additional appendix. This also makes the validation of the mathematics behind the uncertainty values challenging. As the propagated uncertainty is a summation, each part can be evaluated for reasonability e.g., no negative variance sums exist. The first and second order uncertainty values are included in Appendix 3, but it should be noted that the transition temperature is derived through a symbolic solving function of each K_{Jc} specific to specimens and hence the uncertainty added to the T_0 temperature from the measurement uncertainties is not symmetrical or explicitly correct. The method uncertainty for the margin correction is also only positive and adds a degree of conservatism to the estimated toughness range.

5.7.2 Global sensitivity analysis

Since there are many uncertainties related to the uncertainty analysis and the SE(N)T procedure in general, a global uncertainty analysis was conducted on the fracture toughness formulae. The global sensitivity analysis is an analysis of variance which covers a larger range of parameter values compared to the local region of partial derivatives. A Monte Carlo simulation goes through combinations of these parameters until convergence in the outcome is reached. In a sense, it answers the question: “If a parameter, or a combination of parameters are changed, what is the change in the end

result of the model?” The analysis reveals which inputs are most important with regards to the resulting output, the fracture toughness.(Chastaing et al., 2012; Tosin et al., 2020.)

The sensitivity analysis used was Sobol’s indices from the Python module SALib (Herman & Usher, 2017; Inagawa et al., 2022). The model is not concerned as much with uncertainty propagation and estimations on uncertainty distributions, (which are discussed in detail in GUM 2008 supplement 101), than with the effect on the output variance of the simulated system by each individual parameter (Tosin et al., 2020). Sobol’s indices work on the assumptions of Hoeffding decomposition, which states that the variance of the output can be decomposed into increasing order summands. The partitions can be equated to each input parameter or a combination of them, and their sums of the total variance reveal their relevant proportion of the overall variance. (Chastaing et al., 2012.)

The model used in the Sobol indices analysis is the same as the one used for the calculations for the propagation of uncertainty, (79), but the input parameters are more numerous and configured in a different way. This was done to avoid issues with parameter dependence as explored by Chastaing and colleagues (2012). To keep the range of parameter combinations within realistic limits, $\pm 10\%$ shifts to the minimum and maximum values from experimental results were set as the parameter bounds. For example, if the crack length and width of the specimen are given large ranges, the Monte Carlo simulation could try combinations where the crack is longer than the width. In addition, the stochastic nature of the fracture process makes it difficult to set realistic, correlating bounds between the tried values. Furthermore, the effect of each parameter was evaluated using a single range of experimental parameters and shifting them 1% to mimic equally large variance at a more local scale. All the modifications to the formulas can be seen in Appendix 4.

The models install-functionality was evaluated with the SALib reference functions and results. The number of Monte Carlo trials was increased as a power of two, until convergence was reached, and any negative variance values disappear. Simulation with a large number of trials can be computationally expensive, and the desktop used for the analysis with 32 Gb of DDR5 RAM and an Intel i7 12700 processor at 4.9 GHz took

roughly 12 minutes for each 2^{21} run and 34 minutes for 2^{22} trials. Increasing the complexity would demand unreasonable memory resources from consumer hardware.

5.8 Post experiment inspections

After the specimens were fractured, one half of each specimen was cut shorter to allow microscopy of the fracture surfaces. The samples were washed in ethanol, but no other treatments were made. The samples were stored in a desiccator to prevent oxidation. A Zeiss AXIO Zoom V16 optical microscope was used to measure the fracture surface dimensions and a Zeiss FE-SEM was used for a mode in depth fractographical analysis. The manufacturing orientation was also confirmed to match what was instructed for the sample detachment during the optical microscopy. A SE2 detector was used, since it produced the best image. The aperture size throughout the SEM analysis was 30 μm and the acceleration voltage was set at 15 kV. To improve the conduction between the sample and microscope, additional foil tape was used in conjunction with conductive clamps, but the samples were still charged during imaging, which caused drift and blurriness in the images. This issue was later assumed to be caused by insufficient cooling of the electrical components of the microscope.

6 RESULTS & DISCUSSION

6.1 Results

6.1.1 HV10 hardness results

The results of the hardness measurements used in the mechanical property verification are presented below in Table 4 and Figure 29.

Table 4 HV10 hardness measurement results

| HV 10 | Sample button | | | | | | | | | | | StDev 9 |
|----------------|---------------|-----|-----|-----|-----|-----|-----|-----|-----|-----|-----|------------|
| | L1 | | L2 | | L3 | | L4 | | | L5 | | |
| Location [mm] | 5 | 20 | 35 | 50 | 65 | 80 | 95 | 105 | 110 | 125 | 140 | Average |
| 5 | 185 | 189 | 207 | 190 | 214 | 195 | 184 | 196 | 192 | 185 | 193 | 194 |
| 10 | 188 | 181 | 197 | 208 | 198 | 184 | 213 | 193 | 207 | 196 | 210 | 198 |
| 15 | 220 | 183 | 185 | 193 | 192 | 192 | 212 | 192 | 197 | 192 | 187 | 195 |
| 20 | 187 | 189 | 189 | 185 | 191 | 188 | 196 | 194 | 196 | 191 | 200 | 191 |
| Average | 195 | 186 | 195 | 194 | 199 | 190 | 201 | 194 | 198 | 191 | 198 | 195 |

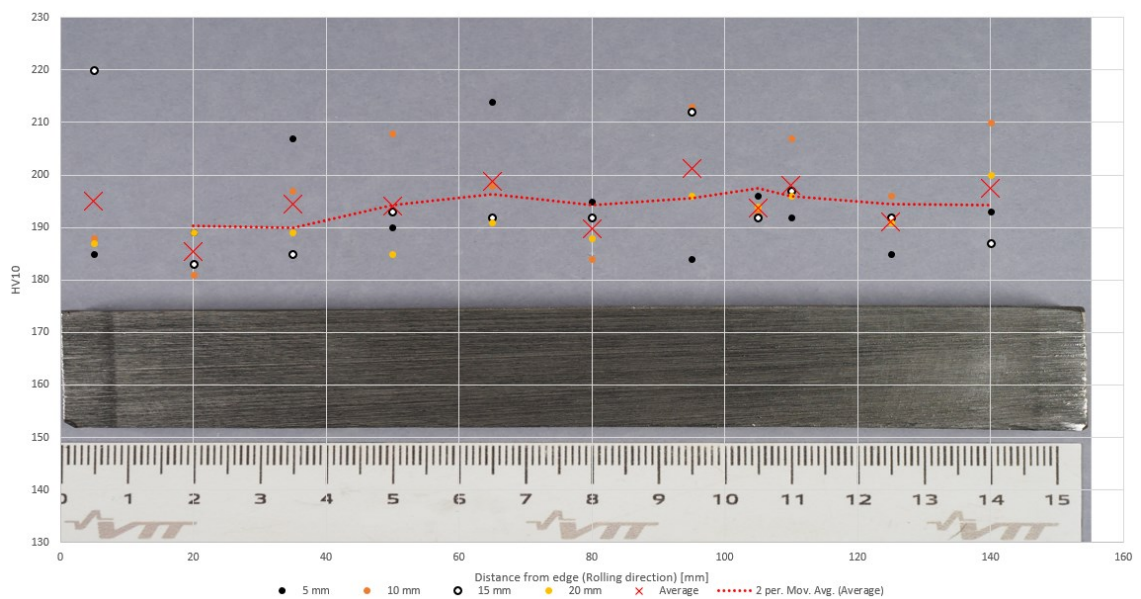


Figure 29 HV 10 hardness measurements overlaid on the sample piece.

6.1.2 Microstructural characterization

Some inclusions/precipitates were found in the new FE-SEM inspection. An energy dispersive spectroscopy analysis indicated that they were MnS, Al₂O₃, and possibly phosphorus impurities illustrated in Figure 30. The size of the impurities found ranged from 1 to 25 μm.

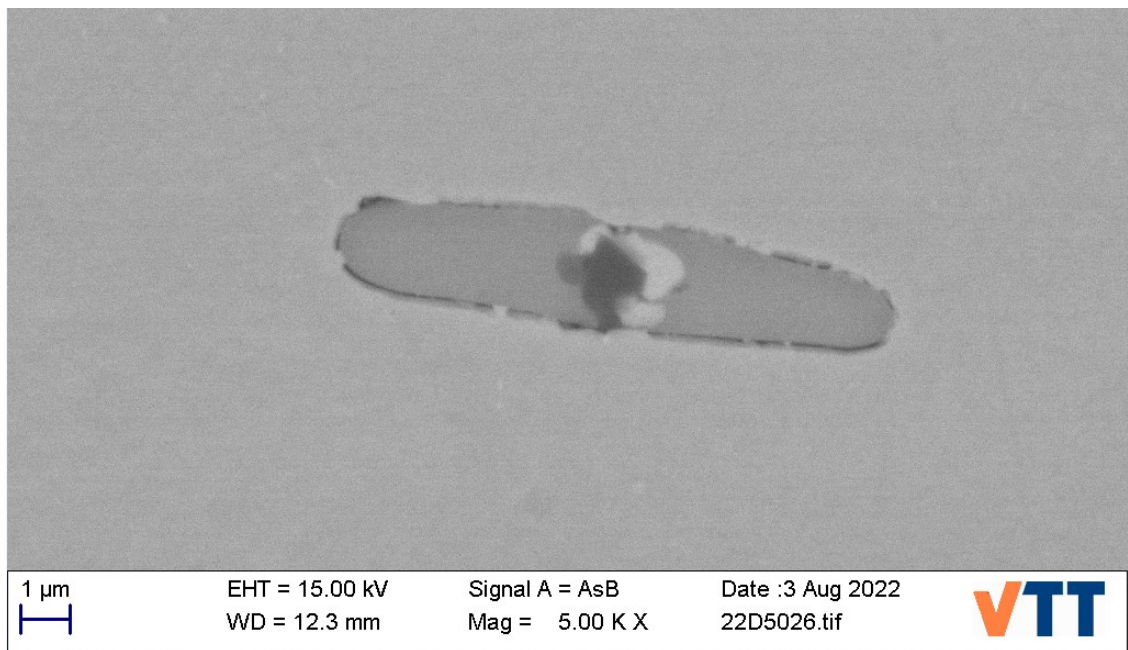


Figure 30 A round aluminum oxide inclusion around which an elliptical manganese sulfide particle has nucleated with traces of phosphorus or zirconium present.

Nothing deviating from the previous microstructural characterizations was discovered under optical microscopy. Darker banded regions were present, which were also reported by Brumovsky and colleagues (2001) who identified them as “ghost lines”.

Under magnification the banded regions seem darker and have a width of ~100 μm, Figure 31. Increasing magnification reveals that the darker color is the result of higher precipitate density, Figure 32.

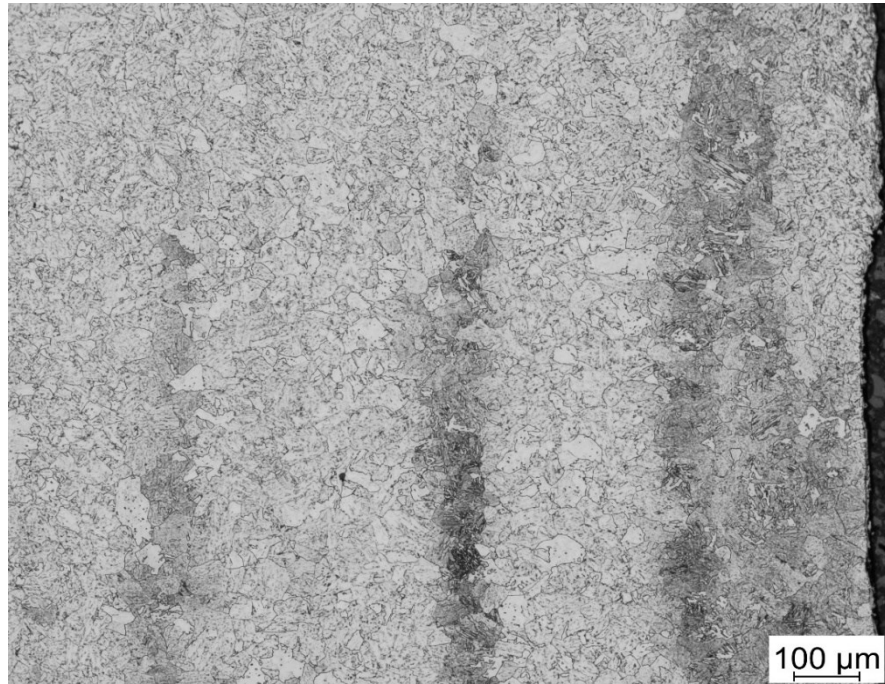


Figure 31 Ghost lines in the sample material, 10x magnification, light Nital- etching.

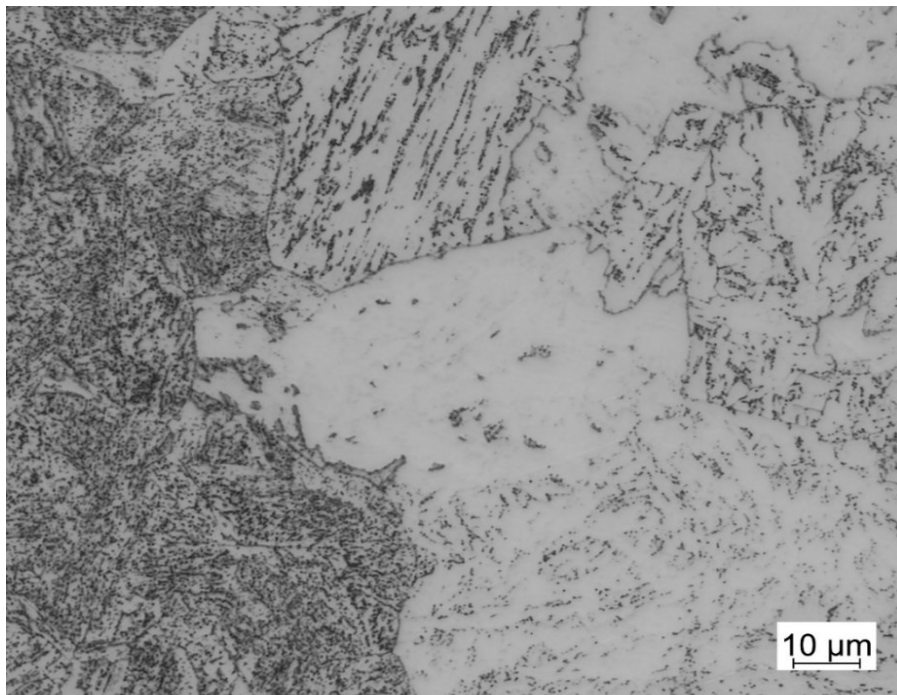


Figure 32 Boundary between the ghost line region (left) showing higher precipitate density and base material on the right, 100x magnification, light Nital- etching.

Lindqvist and Peltonen (2021) reported that lath like structures were found near segregates. In the optical microscopy inspection, laths were found to be more numerous at the darker ghost line regions, Figure 33.

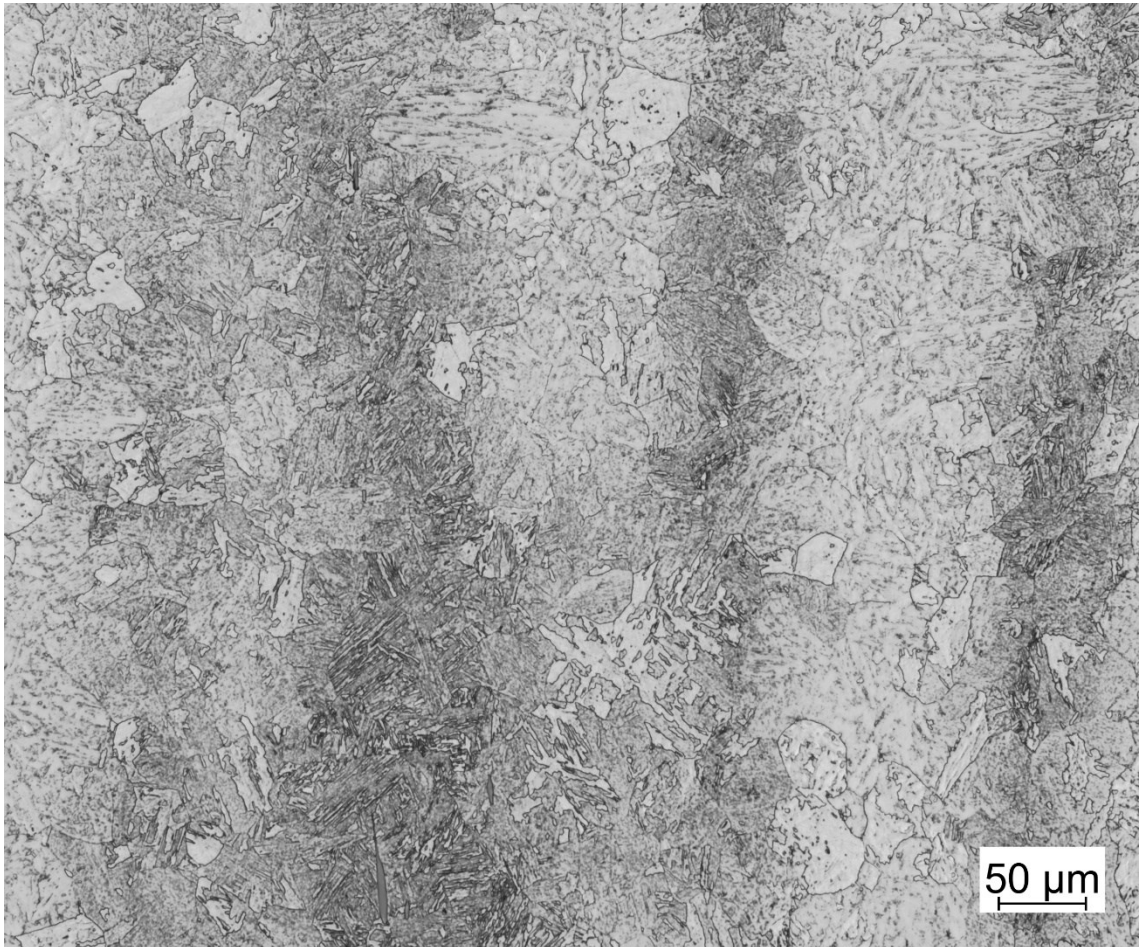


Figure 33 Laths are visible in higher concentrations in the ghost line regions, 20x magnification, light Nital etching.

An example of the manufacturing effects on possible initiation site as discussed in 2.2.1 can be seen in Figure 34, which is a line of inclusions. They could have nucleated on the previous austenite borders due to the rolling process.

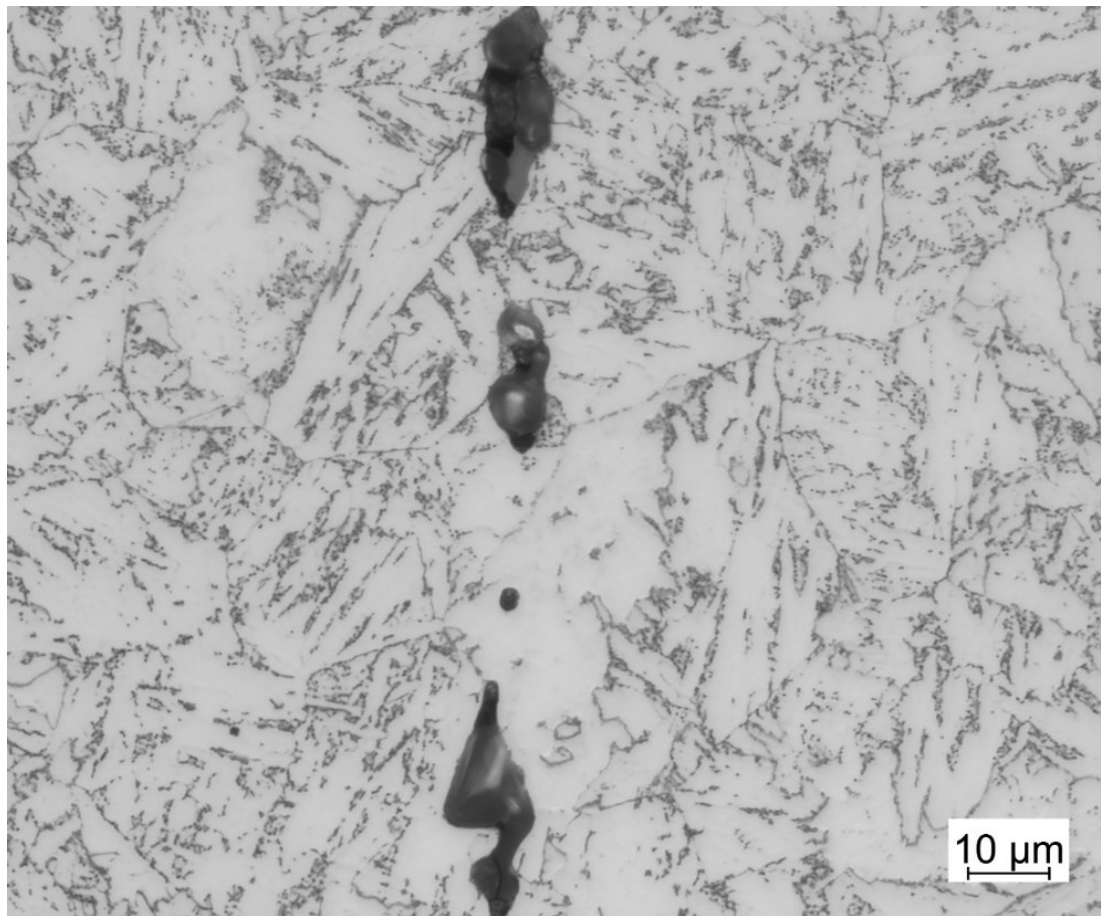


Figure 34 Inclusions possibly on prior austenite grain boundaries visible under optical microscopy.

6.1.3 Fractography

Both the 0.2 and 0.5 aW samples show brittle cleavage fracture. There is no necking present, and the fracture surfaces seem brittle throughout.

Looking with unaided eye the fracture surfaces appear shiny and the fatigued pre-crack can be clearly distinguished. All the pre-cracks seem straight with some having a slight curvature deepening the crack towards the center of the specimen. When measured, this curvature is well within the limit of the requirements set in ASTM E1820 and E1921, in fact, for many cases the straightness would pass ten times stricter limits, Table 5 and Figure 35.

Table 5 Crack depth measurements to verify crack straightness [mm]

| Sample | Location | | | | | | | | | a0 |
|--------|----------|-------|-------|-------|-------|-------|-------|-------|-------|-------|
| | 1 | 2 | 3 | 4 | 5 | 6 | 7 | 8 | 9 | |
| HC1 | 5,040 | 5,193 | 5,194 | 5,249 | 5,254 | 5,216 | 5,210 | 5,249 | 5,177 | 5,209 |
| HC2 | 5,233 | 5,383 | 5,474 | 5,483 | 5,496 | 5,425 | 5,507 | 5,451 | 5,326 | 5,437 |
| HC3 | 5,352 | 5,448 | 5,516 | 5,546 | 5,542 | 5,434 | 5,524 | 5,427 | 5,342 | 5,473 |
| HC4 | 5,237 | 5,337 | 5,420 | 5,448 | 5,554 | 5,456 | 5,561 | 5,485 | 5,299 | 5,441 |
| HC5 | 5,325 | 5,401 | 5,404 | 5,446 | 5,406 | 5,360 | 5,353 | 5,296 | 5,146 | 5,363 |
| HC6 | 5,325 | 5,438 | 5,424 | 5,455 | 5,419 | 5,444 | 5,452 | 5,411 | 5,304 | 5,420 |
| HC8 | 5,259 | 5,403 | 5,404 | 5,443 | 5,482 | 5,456 | 5,451 | 5,440 | 5,276 | 5,418 |
| HC9 | 5,308 | 5,374 | 5,468 | 5,385 | 5,352 | 5,413 | 5,468 | 5,309 | 5,222 | 5,379 |
| HC10 | 5,111 | 5,127 | 5,111 | 5,226 | 5,331 | 5,326 | 5,177 | 5,171 | 5,089 | 5,196 |
| HC11 | 5,264 | 5,414 | 5,459 | 5,471 | 5,494 | 5,445 | 5,424 | 5,446 | 5,238 | 5,426 |
| HC12 | 5,314 | 5,346 | 5,416 | 5,459 | 5,452 | 5,440 | 5,587 | 5,360 | 5,265 | 5,419 |
| LC1 | 1,887 | 2,008 | 1,997 | 2,058 | 2,047 | 2,085 | 2,030 | 2,036 | 2,030 | 2,027 |
| LC2 | 1,964 | 2,140 | 2,151 | 2,140 | 2,118 | 2,058 | 2,014 | 1,970 | 1,887 | 2,065 |
| LC3 | 1,942 | 2,074 | 2,118 | 2,140 | 2,195 | 2,212 | 2,261 | 2,223 | 2,107 | 2,156 |
| LC4 | 2,046 | 2,215 | 2,152 | 2,057 | 2,159 | 2,075 | 1,985 | 2,038 | 2,019 | 2,089 |
| LC5 | 2,002 | 2,099 | 2,192 | 2,228 | 2,299 | 2,193 | 2,330 | 2,130 | 2,174 | 2,195 |
| LC6 | 2,002 | 2,072 | 2,081 | 2,156 | 2,022 | 1,987 | 2,001 | 2,054 | 2,019 | 2,048 |
| LC7 | 2,179 | 2,282 | 2,348 | 2,418 | 2,341 | 2,268 | 2,295 | 2,212 | 2,179 | 2,293 |
| LC8 | 2,046 | 2,180 | 2,292 | 2,333 | 2,324 | 2,337 | 2,307 | 2,347 | 2,251 | 2,284 |
| LC9 | 2,146 | 2,342 | 2,373 | 2,464 | 2,440 | 2,488 | 2,453 | 2,500 | 2,372 | 2,415 |
| LC10 | 2,019 | 2,061 | 2,108 | 2,173 | 2,215 | 2,224 | 2,222 | 2,126 | 2,091 | 2,148 |
| LC11 | 2,079 | 2,093 | 2,101 | 2,099 | 2,146 | 2,192 | 2,157 | 2,121 | 2,042 | 2,121 |



Figure 35 Fracture surface viewed and measured with a Zeiss AXIO Zoom V16.

There is a varying degree of topography with the samples with more plasticity in the CMOD-Force graphs correlating to stronger surface contours. One exception to the plastic flow of the material is located at the very edge of the pre-crack by the notch bottom, as for some samples it exhibits minor necking in a localized region. The same phenomenon is visible in the Abaqus models as well, Figure 36. The region is so small that it is deemed insignificant. A closer inspection indicates that most of the cracks were initiated from the regions highlighted in Figure 37.

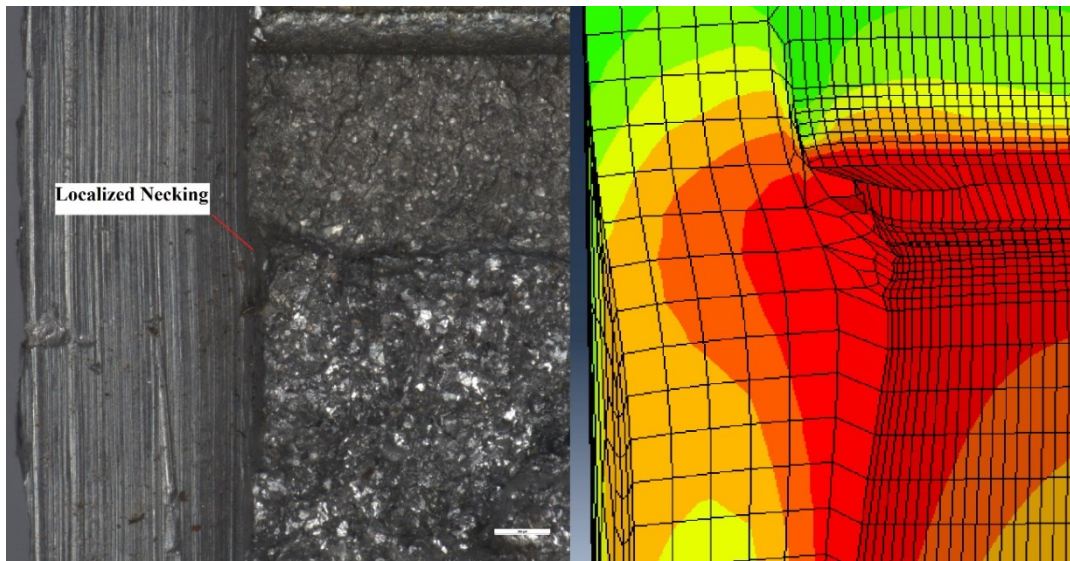


Figure 36 Localized necking observed in the LC4 specimen and Abaqus model.



Figure 37 Common locations for crack initiation highlighted in orange.

Under high magnifications viewed with a SEM, many fracturing features become visible, and they can be used to determine the initiation site more precisely. The fracture mechanism is mixed/quasi-cleavage based on the presence of tear ridges and other indicators of ductility during the cleaving process, such as slip traces and tongues (ASM Handbook Committee, 1999; Brooks & Choudhury, 1993), shown in Figure 38-Figure 41. Additionally, many secondary cracks with varying sizes can be found on the fracture surfaces.

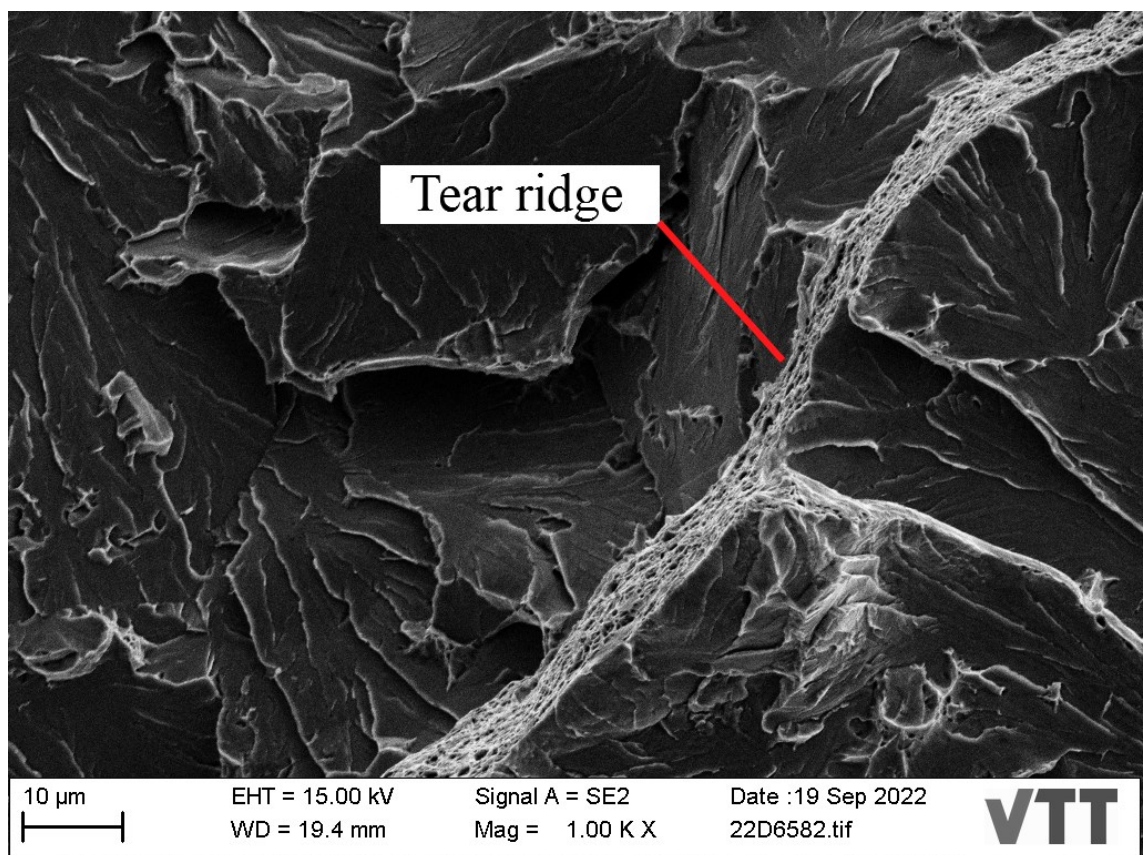


Figure 38 A large tear ridge flows through the center of the image with dimples typical of ductile fracture on otherwise brittle cleavage facets.

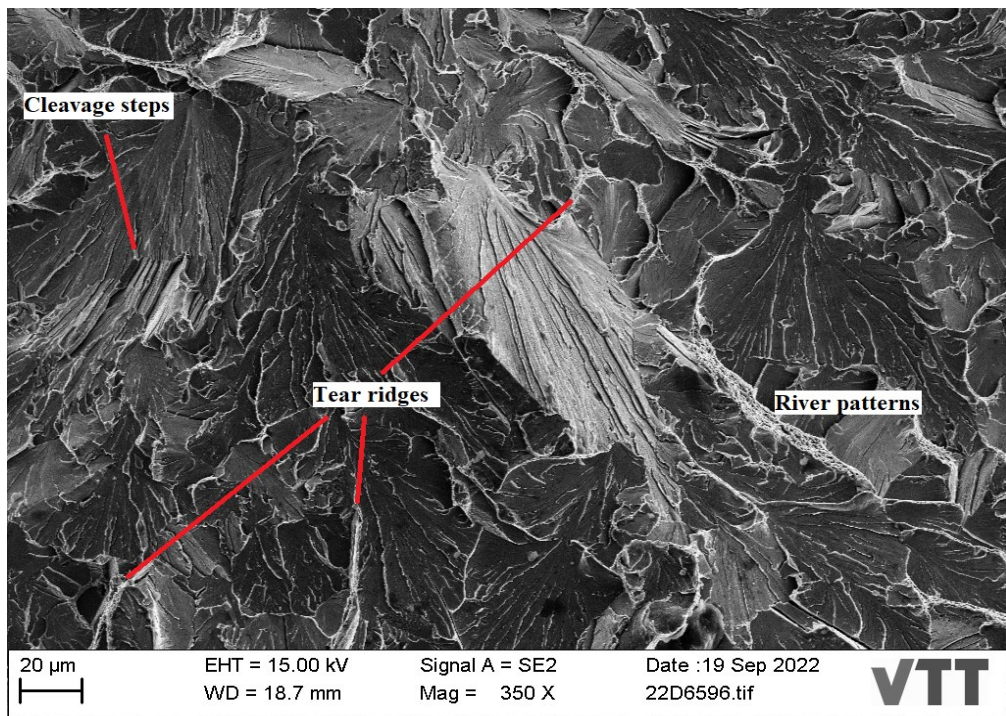


Figure 39 Tear ridges, cleavage steps, and river patterns highlighted on the fracture surface.

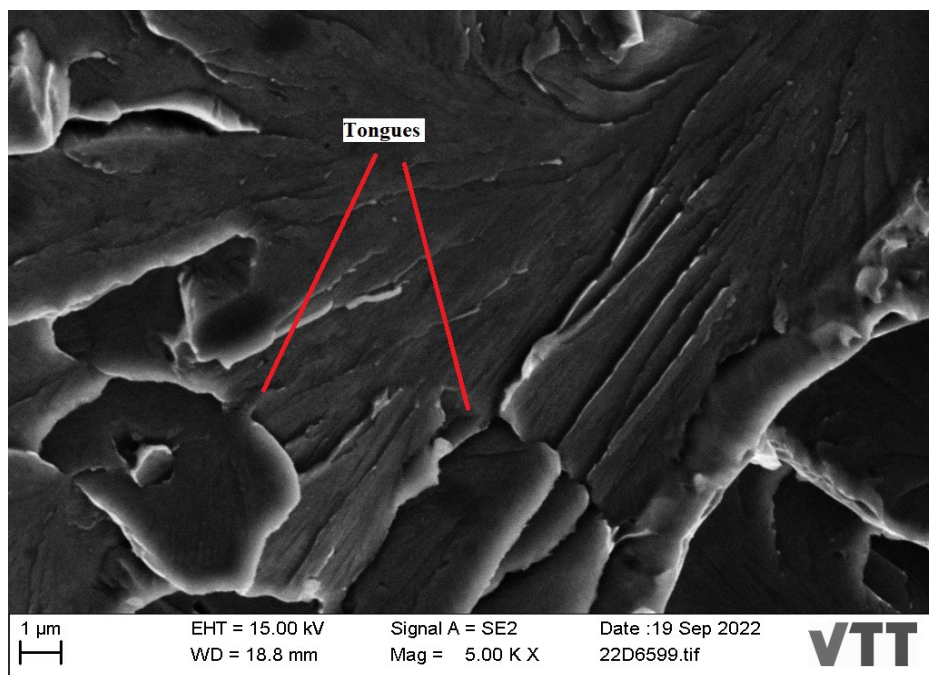


Figure 40 Tongues present on the cleavage surfaces.

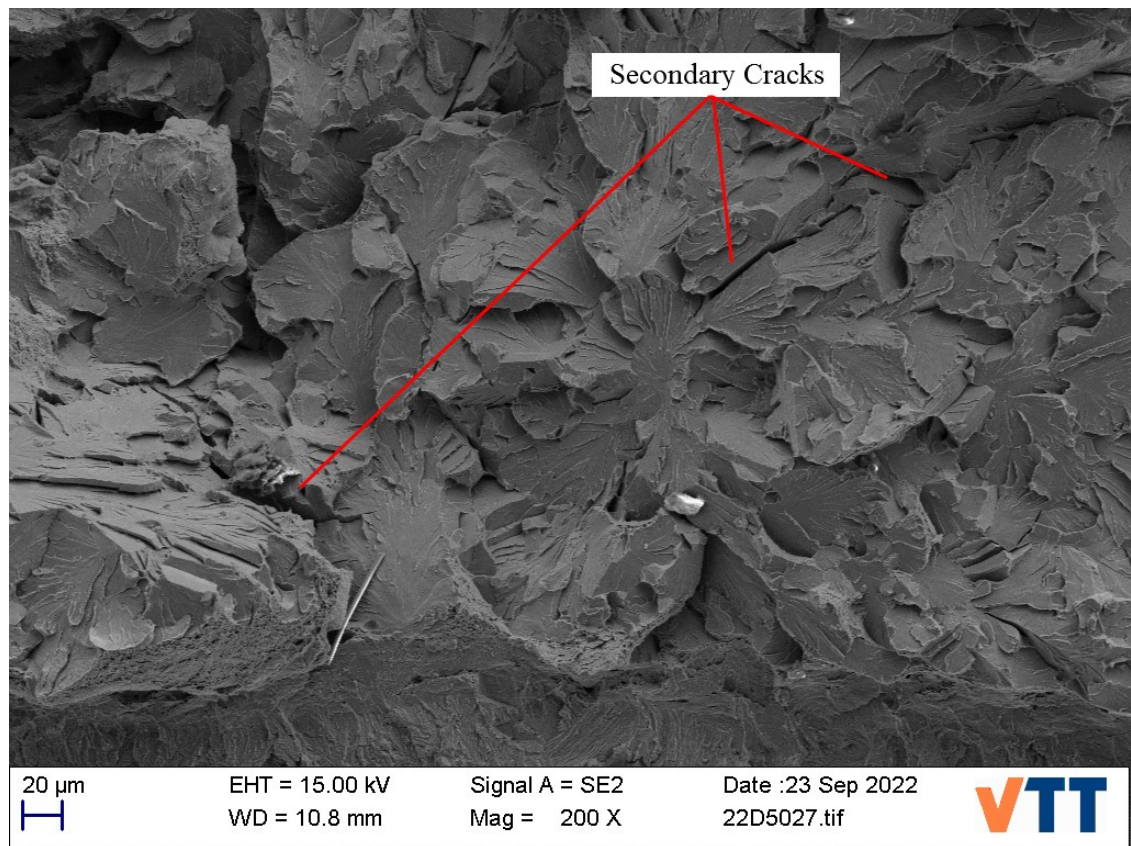


Figure 41 Secondary cracks highlighted with on the fracture surface, more are present but not indicated.

The river patterns point to single origin for initiation for most of the samples. The secondary cracks also give clues on the propagation direction of the fracture on a more macroscopic scale. The initiation site locating procedure is highlighted below in Figure 42 and Figure 43.

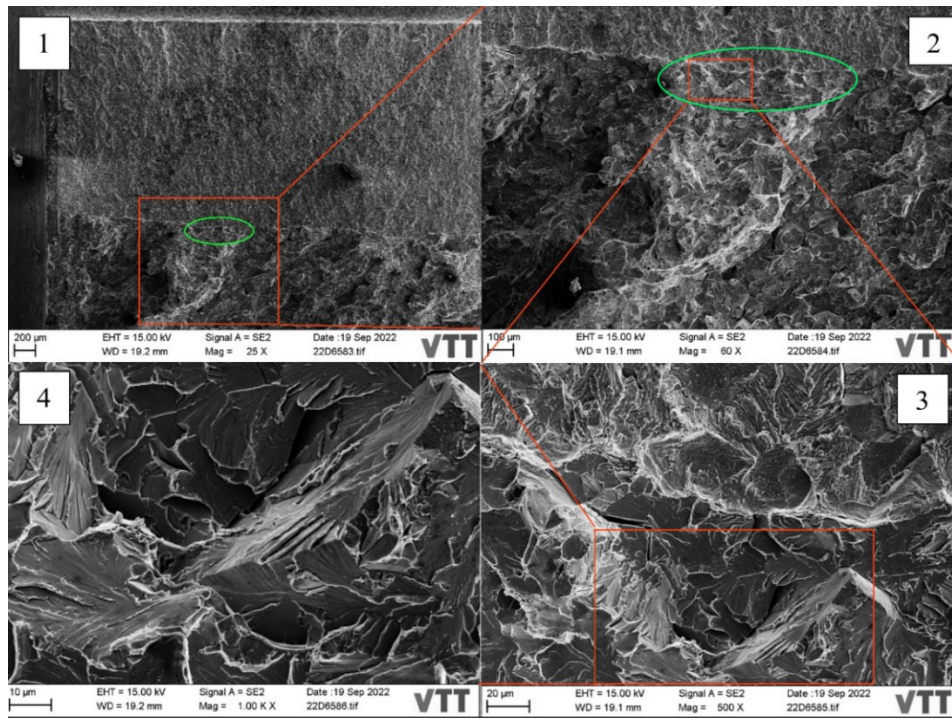


Figure 42 Nucleation site location process, initiation location highlighted in green.

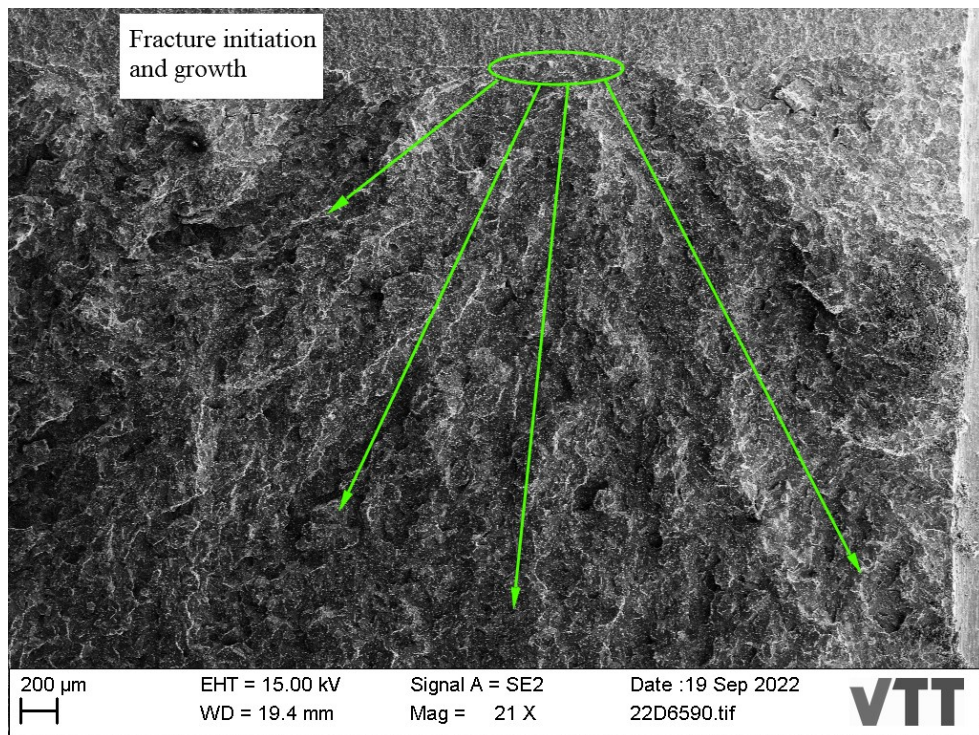


Figure 43 Initiation site and propagation of fracture highlighted in green.

6.1.4 Uncertainty calculation results

When the measurement uncertainties are calculated with the method described in 5.7.1 the following partial uncertainties and their propagation are obtained, Table 6.

Table 6 Measurement uncertainty components

| Sample | Magnitude of 1 σ uncertainty to K_{jc} | | | |
|--------|---|----------|-----------|-----------|
| | $\sigma +10\%$ | σ | 1st order | 2nd order |
| HC1 | 22,91 | 20,83 | 14,08 | 6,75 |
| HC2 | 22,99 | 20,90 | 17,29 | 3,62 |
| HC3 | 5,55 | 5,04 | 3,99 | 1,05 |
| HC4 | 5,98 | 5,44 | 4,22 | 1,22 |
| HC5 | 7,36 | 6,69 | 5,00 | 1,69 |
| HC6 | 7,17 | 6,52 | 4,91 | 1,61 |
| HC8 | 7,41 | 6,74 | 4,94 | 1,79 |
| HC9 | 7,33 | 6,66 | 5,14 | 1,53 |
| HC10 | 5,92 | 5,38 | 4,42 | 0,96 |
| HC11 | 6,96 | 6,33 | 4,72 | 1,61 |
| HC12 | 6,41 | 5,83 | 4,62 | 1,20 |
| LC1 | 61,46 | 55,88 | 34,23 | 21,65 |
| LC2 | 47,88 | 43,53 | 26,34 | 17,18 |
| LC3 | 23,39 | 21,27 | 13,32 | 7,94 |
| LC4 | 9,17 | 8,33 | 5,78 | 2,56 |
| LC5 | 8,43 | 7,66 | 5,44 | 2,23 |
| LC6 | 8,02 | 7,29 | 5,24 | 2,05 |
| LC7 | 12,10 | 11,00 | 6,09 | 4,91 |
| LC8 | 10,50 | 9,54 | 5,74 | 3,80 |
| LC9 | 7,97 | 7,24 | 5,26 | 1,99 |
| LC10 | 7,70 | 7,00 | 5,31 | 1,70 |
| LC11 | 10,92 | 9,93 | 5,86 | 4,07 |

The variances, σ^2 , broken down into each individual factor and their 2nd order combinations are presented in Appendix 3.

6.1.5 Sobols indices

The results of the sensitivity analysis are presented below in Table 7 where the total proportion of the variance is compared to the 1st order component, which covers most of the sensitivity.

Table 7 Sobol's indices global sensitivity analysis results

| Sobol's Indices | | | | | | |
|-----------------|-------------------|-------|--------------|-------|--------------|-------|
| Labels | 1% local variance | | a/W 0,2 ±10% | | a/W 0,5 ±10% | |
| | Total | 1st | Total | 1st | Total | 1st |
| a ₀ | 0,027 | 0,027 | 0,048 | 0,047 | 0,087 | 0,079 |
| W | 0,467 | 0,467 | 0,111 | 0,109 | 0,149 | 0,141 |
| A _p | 0,223 | 0,223 | 0,755 | 0,753 | 0,613 | 0,608 |
| B | 0,002 | 0,002 | 0,003 | 0,002 | 0,004 | 0,003 |
| BN | 0,271 | 0,271 | 0,062 | 0,061 | 0,027 | 0,026 |
| F | 0,009 | 0,009 | 0,024 | 0,023 | 0,137 | 0,126 |
| T | 0,000 | 0,000 | 0,000 | 0,000 | 0,000 | 0,000 |

6.1.6 Experimental results

In total 23 specimens were tested, 12 HC a/W 0.5 specimens and 11 LC a/W 0.2 specimens. Three first specimens of the LC series LC1, LC2 and LC3 are omitted from the final calculations as they were used to calibrate the testing procedure and had different loading rates. Three were omitted from the HC series as well, HC1 and HC2 as they were used for calibration (different load rate) and HC7 since it produced a divergent CMOD-Force graph indicating failed procedure, most likely due to poor clamping. All the CMOD-Force graphs are visible in Appendix 5. The calibration specimen results are included in the tabular presentation, but highlighted red, Table 8.

The ASTM standards used for the Master Curve calculations have several censoring criteria. There is no observed crack growth, issues with crack straightness or load rates, but ultimate tensile load and initial crack estimation could be used as basis for censoring certain specimens. Results based on different censoring criteria are presented below.

6.1.7 High Constraint HC-Series

When the values from HC3-HC11 are inserted to the formulas presented in 5.5 and scaled to 1T reference size the T_0 temperature is $-54\text{ }^\circ\text{C}$, if one standard deviation of measurement error is added or subtracted from the K_{Jc} values the range due to measurement uncertainty is from -62 to $-45\text{ }^\circ\text{C}$. A conservative method uncertainty presented in 5.7, formula (76) shifts the results upwards $\sim 7\text{ }^\circ\text{C}$. The datapoints are presented on the Master Curve graph below, Figure 44 and tabularly in Table 8. Additional values are presented in Appendix 6.

Table 8 HC-Series results

| LEGEND | HC1 | HC2 | HC3 | HC4 | HC5 | HC6 | HC8 | HC9 | HC10 | HC11 | HC12 |
|--------------------------------------|-------|-------|-------|-------|-------|-------|-------|-------|-------|-------|-------|
| T [$^\circ\text{C}$] | -85,3 | -85,8 | -85,7 | -86,1 | -85,8 | -86,0 | -86,3 | -85,9 | -85,1 | -86,0 | -85,2 |
| K_{Jc} [MPa $\sqrt{\text{m}}$] | 134,8 | 70,8 | 77,1 | 80,5 | 94,7 | 87,5 | 100,7 | 85,6 | 65,0 | 95,5 | 73,0 |
| K_{Jc} 1T [MPa $\sqrt{\text{m}}$] | 110,9 | 60,2 | 65,2 | 67,9 | 79,2 | 73,4 | 83,9 | 71,8 | 55,6 | 79,8 | 62,0 |

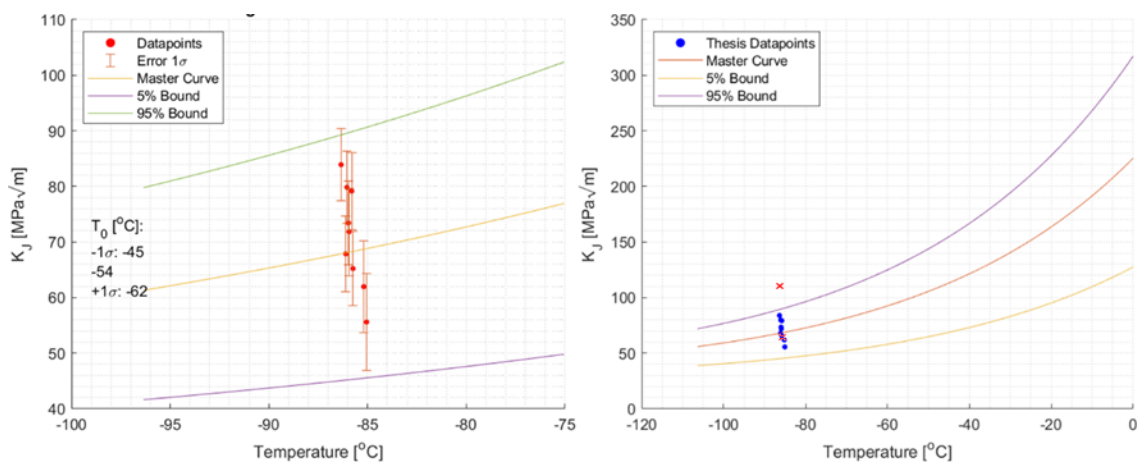


Figure 44 HC-Series Master Curve, censored HC1 and HC2 values are represented by red crosses.

6.1.8 Low Constraint LC-Series

Following the same procedures as for the HC-Series produces a 1T reference size scaled T_0 temperature of $-113\text{ }^{\circ}\text{C}$ for the LC-series. If one standard deviation of measurement error is added or subtracted from the K_{Jc} values, the T_0 temperature ranges from -117 to $-110\text{ }^{\circ}\text{C}$ due to measurement uncertainty. The method uncertainty shifts the results upwards an additional $\sim 7\text{ }^{\circ}\text{C}$. The Master Curve and toughness values are presented below in Table 9 and Figure 45.

Table 9 LC-Series results

| LEGEND | LC1 | LC2 | LC3 | LC4 | LC5 | LC6 | LC7 | LC8 | LC9 | LC10 | LC11 |
|--------------------------------------|--------|--------|--------|--------|--------|--------|--------|--------|--------|--------|--------|
| T [$^{\circ}\text{C}$] | -85,36 | -85,63 | -86,08 | -86,68 | -86,02 | -86,46 | -86,54 | -85,12 | -87,32 | -85,60 | -85,49 |
| K_{Jc} [MPa $\sqrt{\text{m}}$] | 204,81 | 205,44 | 190,21 | 142,51 | 133,90 | 129,16 | 232,25 | 200,01 | 113,10 | 98,05 | 211,64 |
| K_{Jc} 1T [MPa $\sqrt{\text{m}}$] | 166,28 | 166,81 | 154,77 | 117,00 | 110,17 | 106,42 | 188,06 | 162,52 | 93,73 | 81,80 | 171,76 |

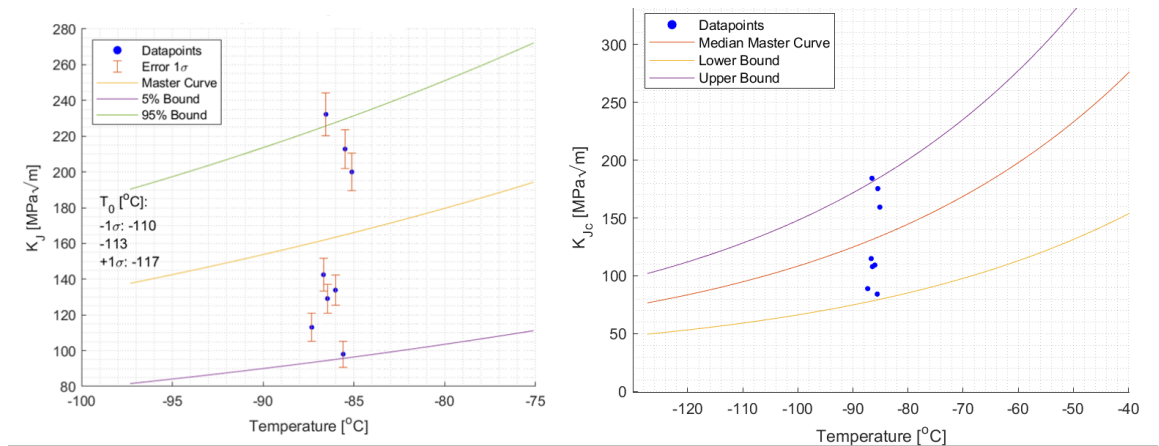


Figure 45 LC-Series Master Curve for all non-calibration specimens.

If the results are observed there is a cluster of three high toughness samples and five lower strength specimens. The high toughness specimens are highlighted with yellow in Table 9. A suspicious gap in the data distribution exists between these groups and if the analysis is done excluding the three highest toughness values, the following master curve with a

1T reference size scaled T_0 temperature of $-98\text{ }^\circ\text{C}$ is produced, Figure 46. If one standard deviation of measurement error is added or subtracted from the K_{Jc} values, the T_0 range due to measurement uncertainty is from -102 to $-93\text{ }^\circ\text{C}$. The method uncertainty shifts the results upwards an additional $\sim 9\text{ }^\circ\text{C}$. The five remaining samples are not enough to satisfy the minimum data requirements for the master curve, the temperature would be lower if a K_{Jc} limit value for the 3 tougher specimens was substituted in addition, but no rigorous method assessing the limit value for these conditions was found. The resulting curve is presented in Figure 46.

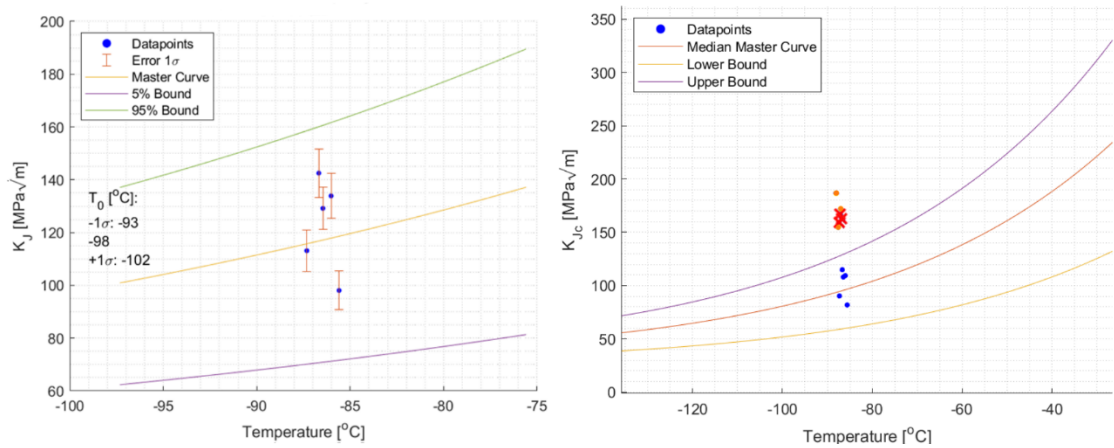


Figure 46 Lower toughness cluster Master Curve, censored calibration (LC1-3) values are presented with red crosses and other censored values (LC7, LC8, and LC11) are orange.

When plotting the probabilities for failure (17) at each K_{Jc} value and corresponding T_0 temperature (-54 for HC and -98 for LC) the following distribution is obtained, Figure 47

| | | | | | | | | | | | |
|--------------|---------------|---------------|---------------|-------------|--------------|--------------|--------------|--------------|--------------|------------|----------------|
| LC-11 (1) | HC-11 0.80 | LC-9 0.60 | HC-9 0.60 | LC-7 (1) | HC-7 (-) | LC-5 0.87 | HC-5 0.79 | LC-3 (1) | HC-3 0.41 | LC1 (1) | HC-1 (0.97) |
| LC-12 (-) | HC-12 0.32 | LC-10 0.37 | HC-10 0.18 | LC-8 (1) | HC-8 0.88 | LC-6 0.82 | HC-6 0.64 | LC-4 0.94 | HC-4 0.48 | LC2 (1) | HC-2 (0.28) |

Figure 47 Probability for failure for the loads each specimen failed at, censored sample values are within parentheses, the location of the specimens matches their positions in the initial material piece viewed from the long transverse direction.

6.1.9 Abaqus model results

The Abaqus CMOD-Force graph overlain with experimental results is presented below in Figure 48. HC1 and LC1 graphs are used in the illustrations, but almost all the CMOD-Force graphs overlap with a similar margin. Additional samples are presented in Figure 49.

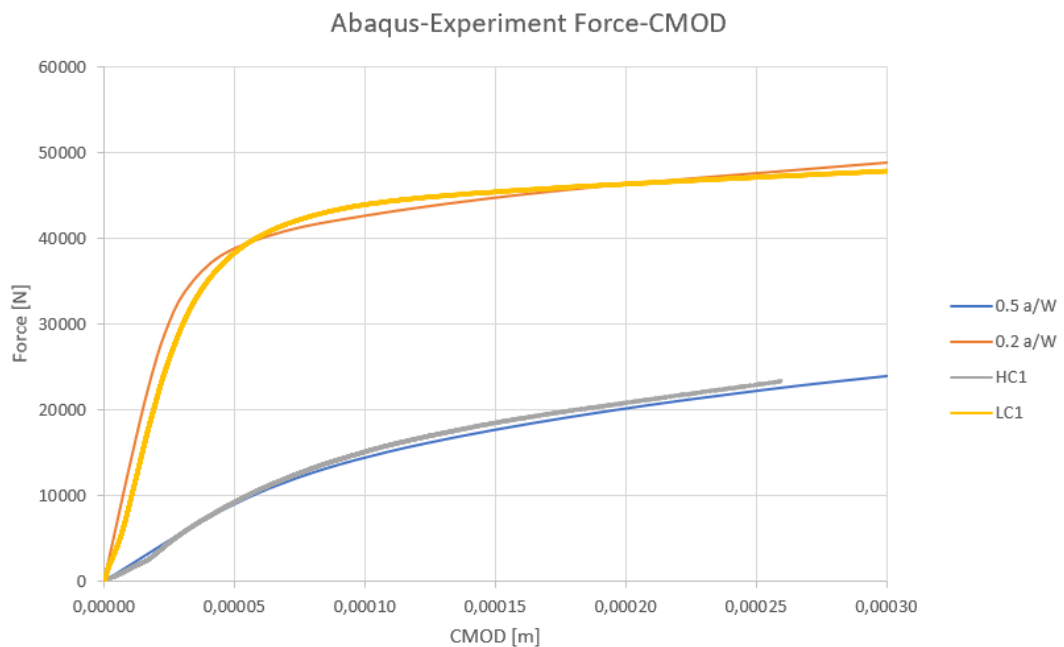


Figure 48 Agreement between the Abaqus model and experimental results.

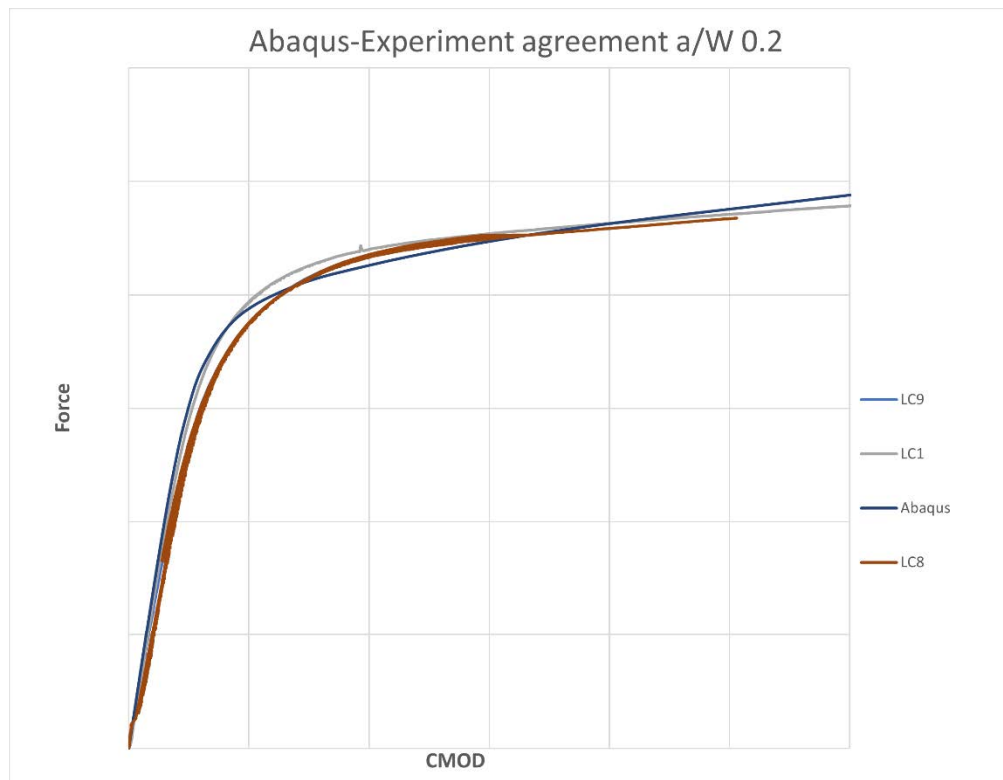


Figure 49 Overlap between CMOD-Force graphs of different LC samples and the Abaqus model.

The S_{22} stress field in the X direction (X indicated in Figure 26) in front of the crack tip produces different gradients for the stress intensity depending on the geometry and load. The HC, LC, and C(T) geometries S_{22} stress-J graphs at the distance normalized by formula (37) are shown below in Figure 50. The development of S_{22} stress in front of the crack tip for the different modelled geometries at a constant J value (experiment result average) is presented in Figure 51. A similar comparison for the same geometries at constant J and r values are presented in Figure 52 and Figure 53.

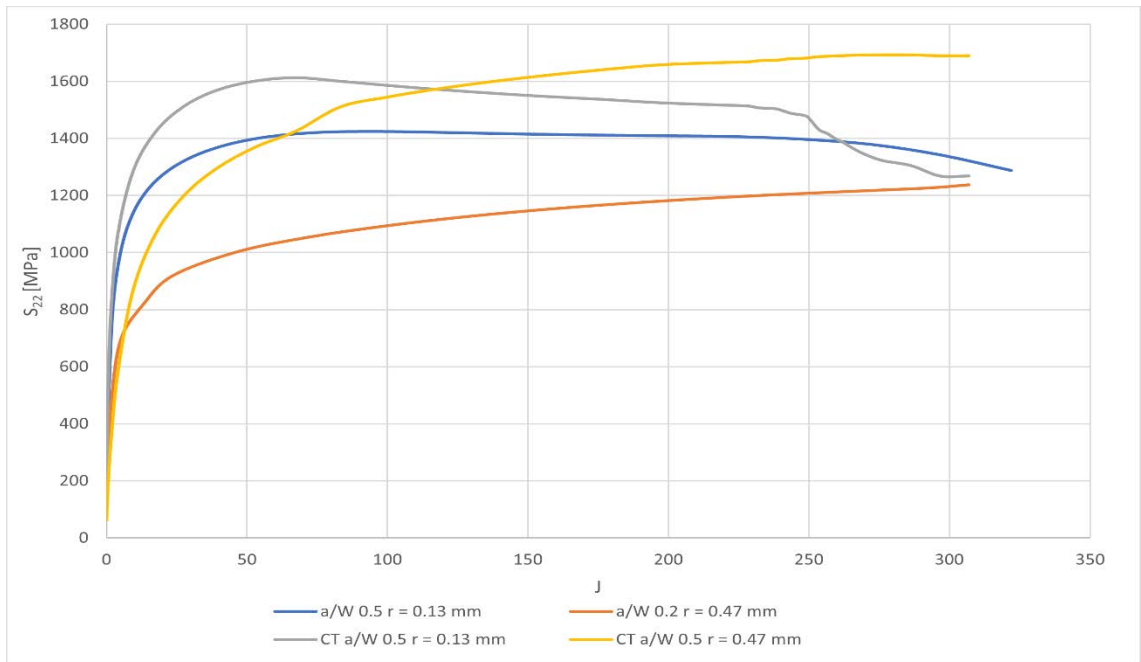


Figure 50 Stress-J graph at normalized radius corresponding to the experiment average values.

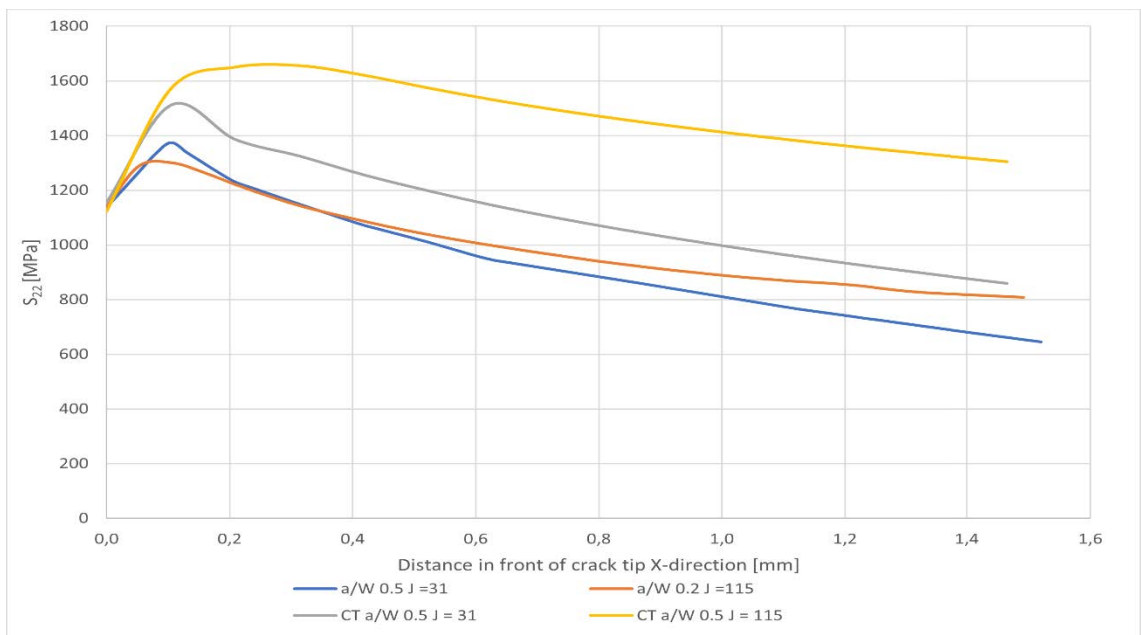


Figure 51 Stress-Radius graph at the J- values corresponding to the experiment average values.

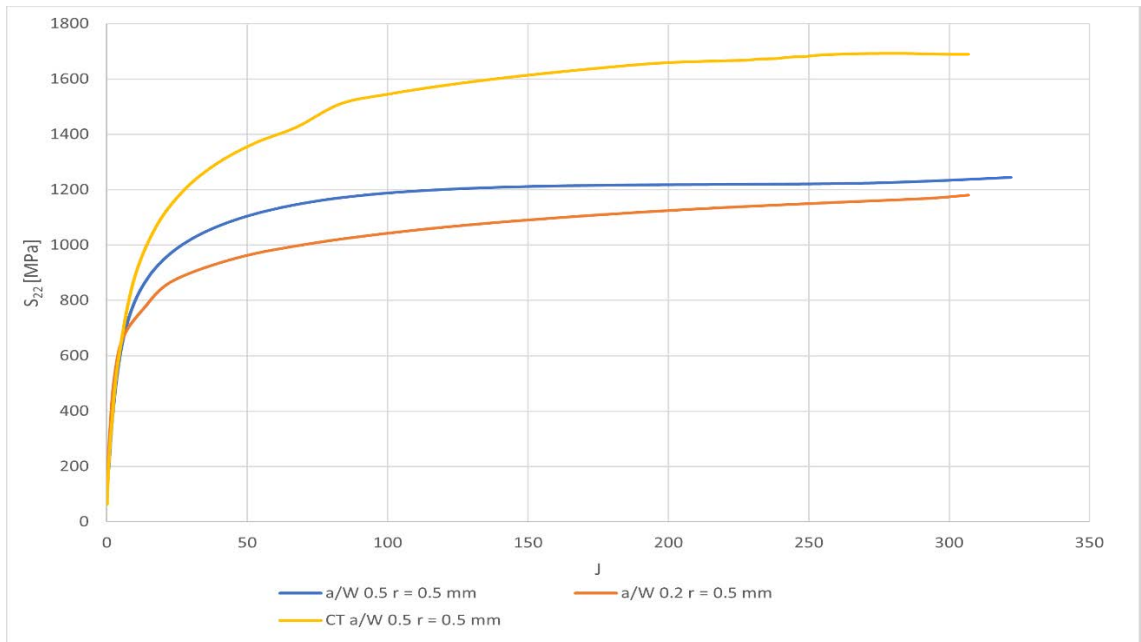


Figure 52 S_{22} stress development at a constant distance 0.5 mm in front of the crack.

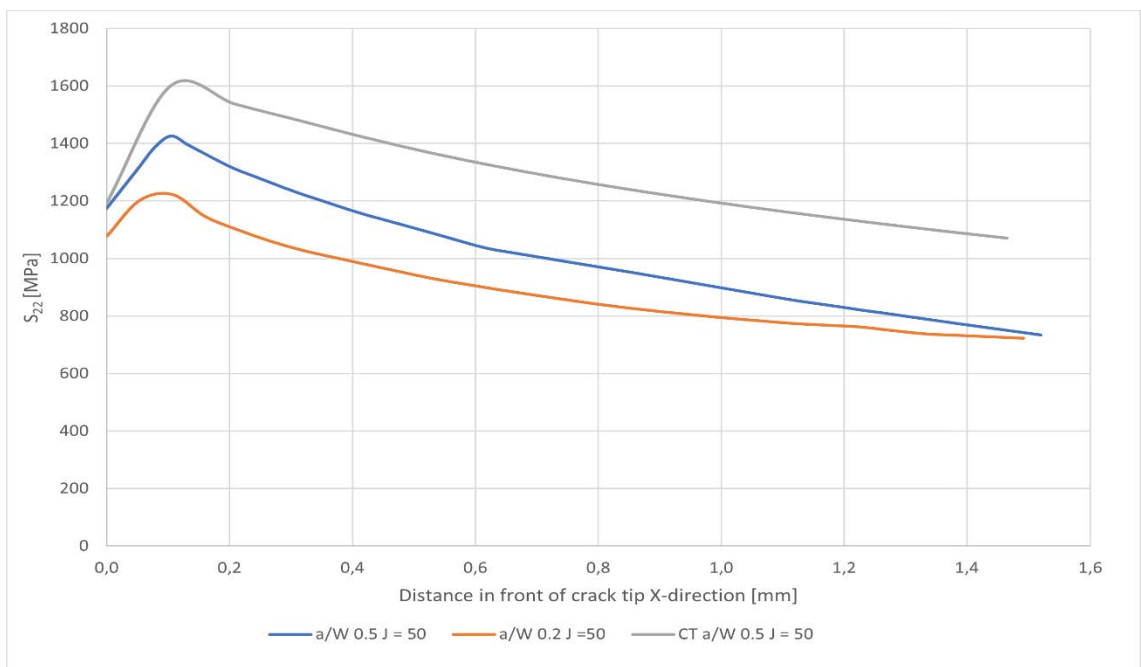


Figure 53 S_{22} stress development in front of the crack tip at a constant J .

When the distance is normalized through the formulas presented in 3.2.2 the correct values can be picked from the Abaqus model outputs for the Q-parameter calculations using the method described in 5.6. The Q-Parameters were assessed using the HRR field as reference (1626 MPa) and their evolution over J-integral is presented below, Figure 54. From the graph it can be seen that the Q-parameter tends towards negative infinity as J approaches zero. This is assumed to be caused by the crack tip blunting (Anderson, 2005 p. 114). In fact, the results, although scaled differently, are similar in shape when compared to the blunted crack tip FEM-models compiled by Wallin (2011 p. 19-20).

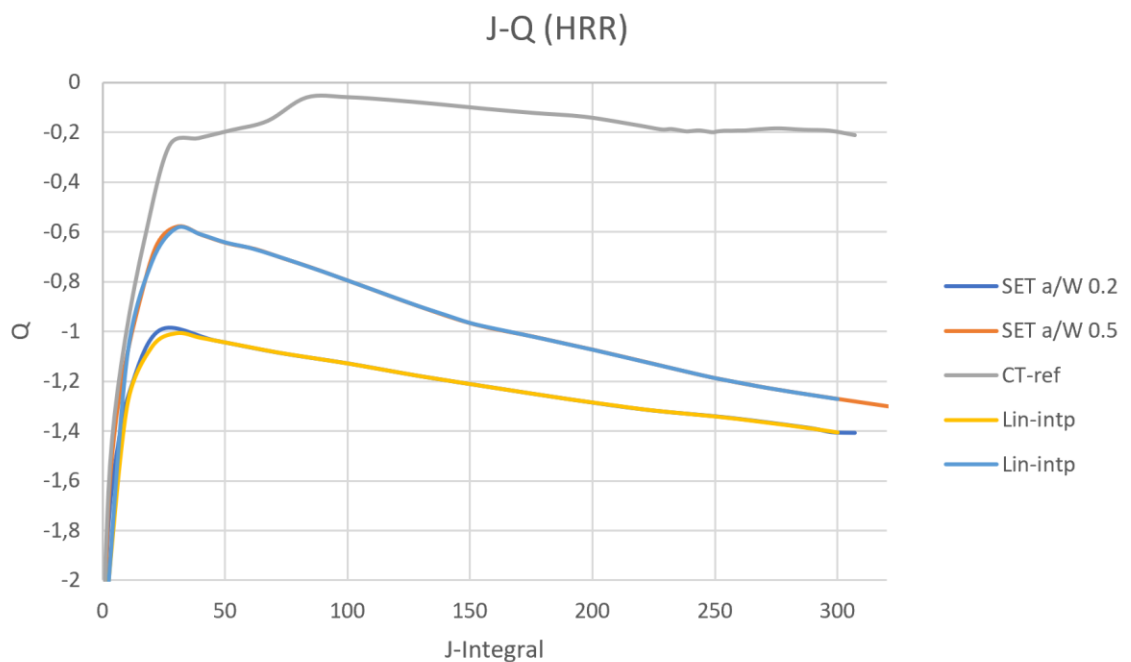


Figure 54 HRR reference Q-parameter as a function of J-integral for the different models.

Using formula (74) the Q-parameter can be correlated with a shift in the T_0 temperature for the chosen J integral value, Figure 55. For the average and median J values for both of the geometries, the model predicted T_0 difference is presented in Table 10. In addition,

a comparison result based on the T-stress calculated through formulas (34) and (35) is included in the same table.

Table 10 T₀ Temperature shift from Q-constraint

| Legend | J _c | | Q-T ₀ shift | | Distance | Q | Qref | T-stress T ₀ shift |
|------------|----------------|------|------------------------|-----|----------|-------|-------|----------------------------------|
| | Avg | Med | Avg | Med | r [mm] | - | - | |
| LC | 114,6 | 81,7 | -43 | -41 | 0,47 | -1,15 | -0,07 | -21,6 |
| HC | 30,9 | 31,4 | -14 | -14 | 0,13 | -0,59 | -0,25 | -5,5 |
| Difference | 83,7 | 50,3 | -29 | -27 | - | - | - | -16,1 |

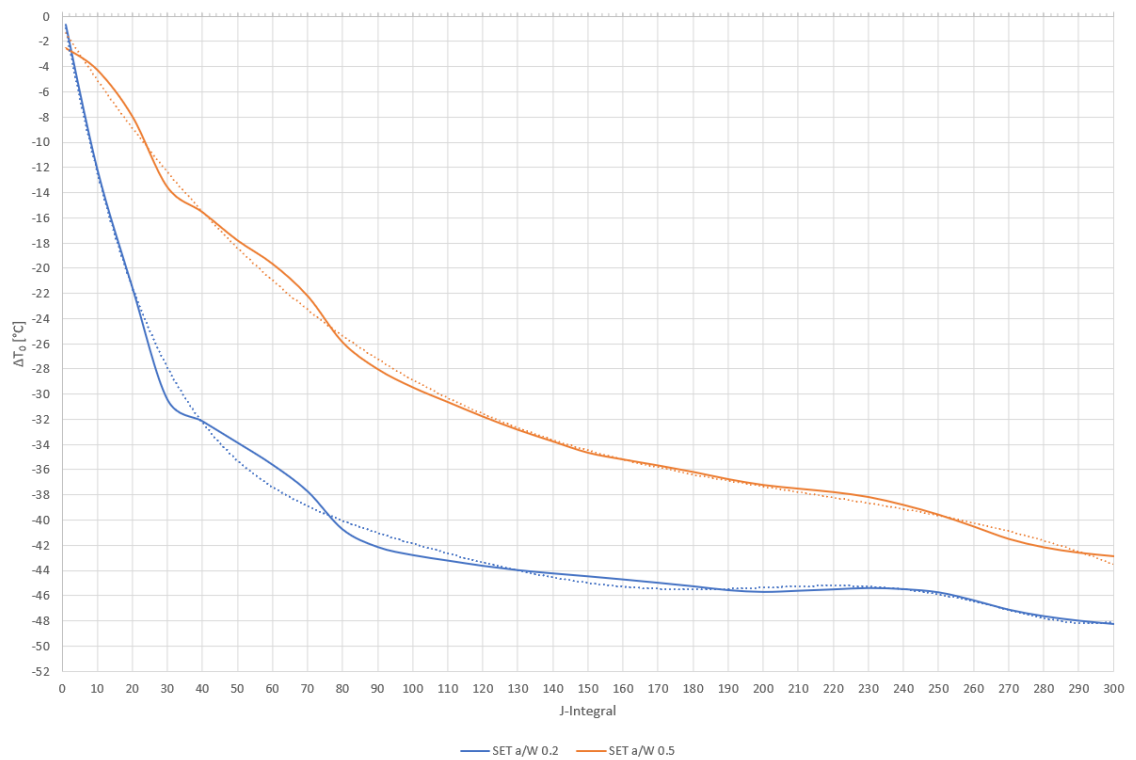


Figure 55 Shift in T₀ temperature for HC and LC specimens for different J values.

6.2 Comparison to previous results

When the new results are compared to previous results, Table 11, the T_0 values of -54 °C for HC and -98 °C or the 5 lower toughness LC samples go on both sides of the previous estimation ranges. The datapoints and Master Curve for the tests combined by Lindqvist and Peltonen (2021) are compared to the thesis results in Figure 56

Table 11 Comparison T_0 temperatures for the JRQ material

| Source | Specimen | T_0 [°C] | σ [°C] |
|-------------------------------|----------------------|------------|---------------|
| Lindqvist and Peltonen (2021) | 15x30 SE(B) a/W 0.5, | -79 | 5,7 |
| | 5x10 SE(B) a/W 0.5, | -86 | 7 |
| Thesis | SE(N)T a/w 0.5 | -54 | 8,5 |
| | SE(N)T a/w 0.2 | -98 | 5 |
| (Brumovsky et al., 2001) | 10x10 CVN | -71 | ± 10 |
| Wallin (1995) | C(T) 4T | -35* | - |
| | C(T) 1T | -54 | - |
| | CVN | -57 | - |

*Contains inhomogeneities

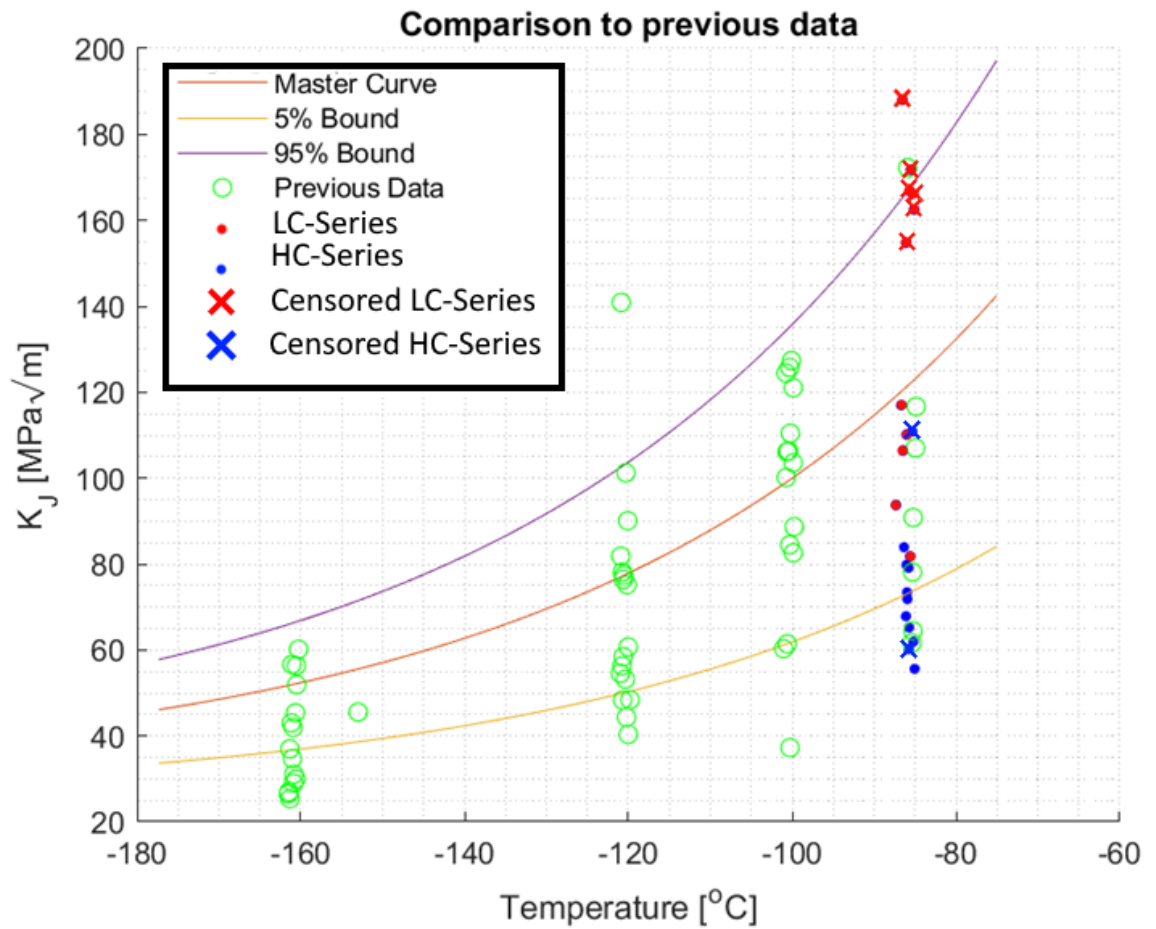


Figure 56 All measurement points compared the previous results for the same material from the study by Lindqvist and Peltonen (2021).

The constraint behavior of the Q-parameter as a function of load can be compared to the results by Moattari and Sattari-Far (2017) which are based on similar a/W SET specimens in 1T size. Moattari and Sattari-Fari's material is different with a lower yield strength range (350 –480 MPa vs JRG 488 –560 MPa), Figure 57.

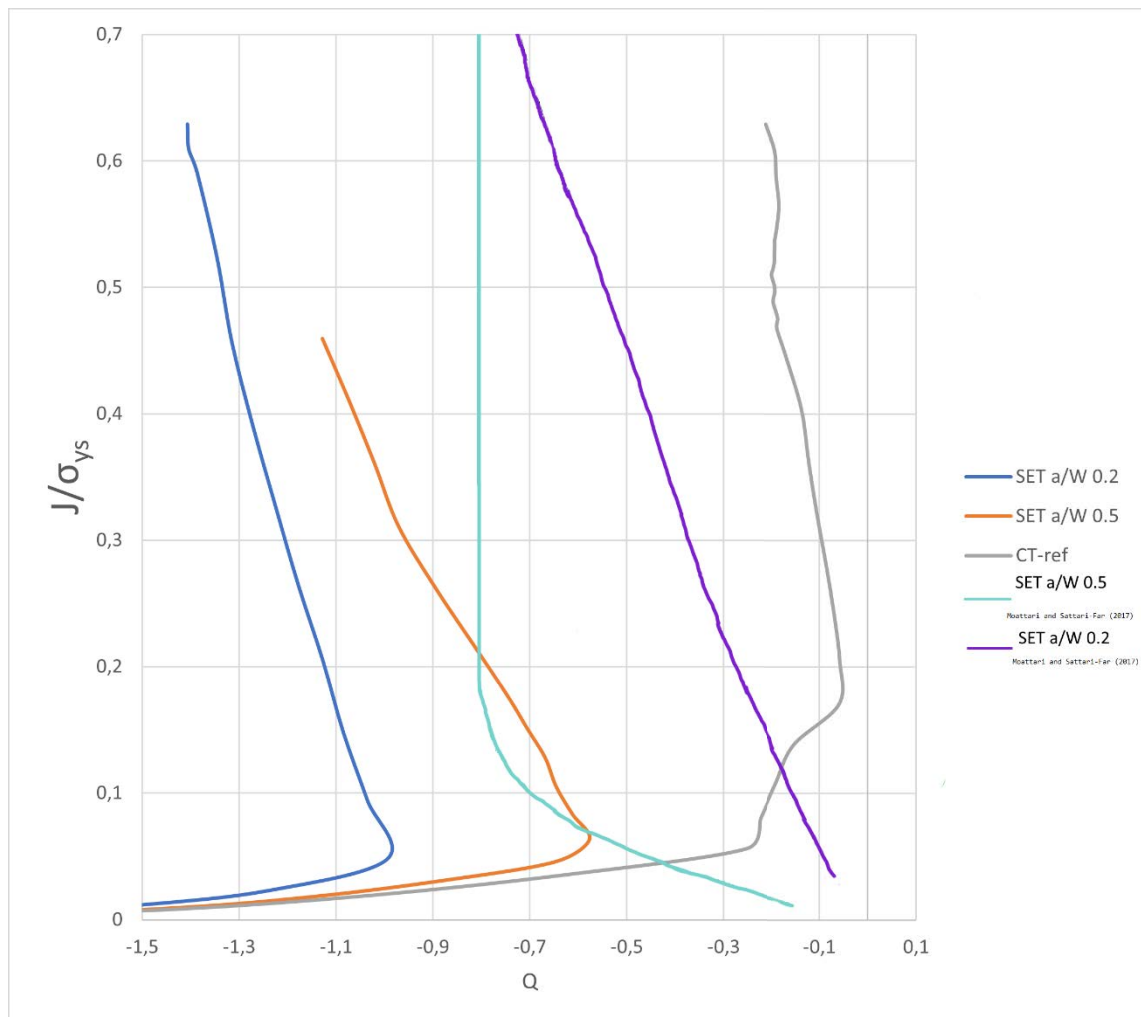


Figure 57 Q-parameter development over normalized J values for SET specimens.

6.3 Discussion

A pre-requisite for the Master Curve functionality is homogeneity on a macroscopic scale, as the cumulative probability distribution functions depend on Poisson distributed faults. Based on the HV10 measurements there should not be any property gradients. A two-way analysis of variance (ANOVA) was conducted, Table 12, to determine if the measurement location had a statistically significant effect on the hardness, but the F values were far from disproving the hypothesis that there is statistically significant difference in the mean hardness values over the geometry for both rolling and short transverse directions. Furthermore, their corresponding p-values were 0.48 and 0.55. This indicates that no statistically significant hardness gradient exists in the chosen sample piece and that no

extreme deviation in hardness was present. As the hardness measurements conform with previous experiments, the tensile strength values are assumed to be applicable as well.

Table 12 ANOVA on the hardness variation over thickness and width

| ANOVA | | | |
|----------------------------|--|----------|----------------|
| Source of Variation | F crit to disprove the hypothesis | F | P-value |
| Thickness direction | 2,92 | 0,84 | 0,48 |
| Width direction | 2,16 | 0,89 | 0,55 |

Only the short transverse direction should affect the material properties, and the samples are removed as pairs, so that there is a sample from the two available thicknesses. The other material variation should be minimal as the cracks are from the same lengthwise spot and the width is taken into account by the variation of sample type removal order.

While the mechanical properties might not have a gradient, the segregations and other inclusions could be unevenly distributed. The higher precipitation density of the ghost lines indicates an uneven distribution of alloying elements at the microscopic scale. The exact effects on mechanical properties these regions have are unknown, but one can assume they exist, and increase the brittleness, based on the results reported by Kantidis et al., (1994) and Yahya et al., (1998). Furthermore, the presence of lath structures near the ghost lines could be the result of higher hardenability due to increased alloying element concentrations. The tempering history combined with the “dirtier” melts of the production era raise the question of tempering embrittlement and its effects on fracture toughness. The phosphorus content is relatively high and there are elements such as chromium and nickel present that tend to form carbides at the grain boundaries. Even so, fractographical analysis did not reveal intergranular fracture facets indicating weakened boundaries, and SEM analysis did not highlight precipitation to the grain boundaries. The molybdenum content should also retard carbon diffusion preventing tempering embrittlement (Hwang et al., 2011). Based on this, tempering embrittlement is ruled out.

To determine if the ghost lines, and their effects, are evenly distributed, their range is evaluated through the use of inverse binomial distribution. A photo editing software is used to increase the contrast of the sample button image, which highlights the ghost lines, Figure 58. The highlighted lines can be selected, and their area is compared to the total sample area. From this, and an assumption that the lines are generally evenly distributed, a probability can be assigned for the chance of selecting an area with the same distribution of base material and ghost line regions.

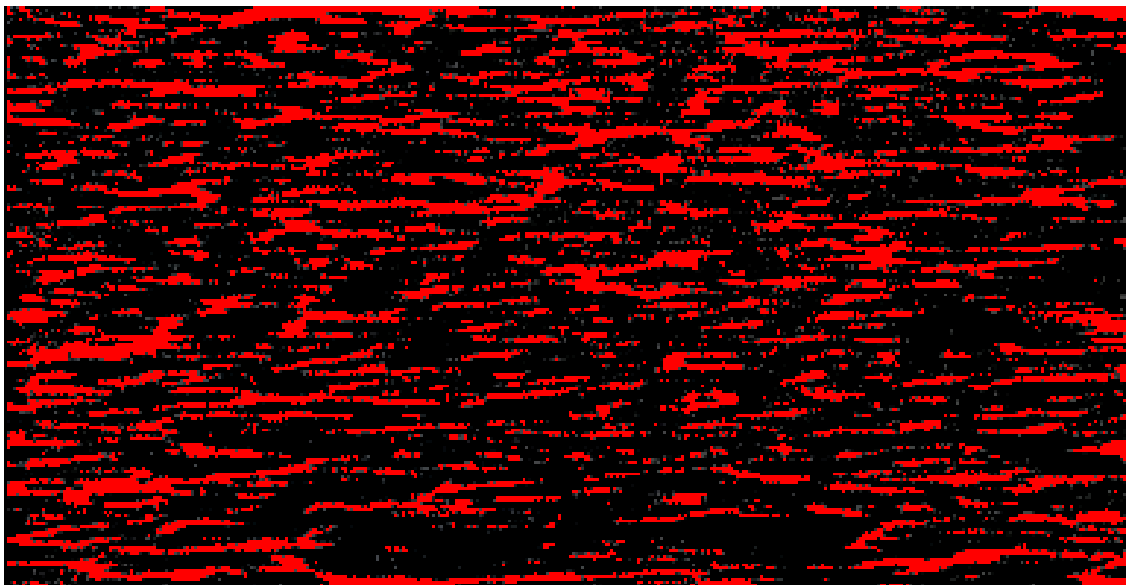


Figure 58 Base material and Ghost line regions (Red) highlighted for distribution ratio determination.

The ratio of ghost line to base material is 0.26 which is rounded to one fourth. The average size for the line is set at 100 μm and an inverse binomial distribution graph is formulated to illustrate an answer to the question: “How large a sample size is needed for the

distribution of base material and ghost lines to converge given a 95% confidence interval?”, Figure 59.

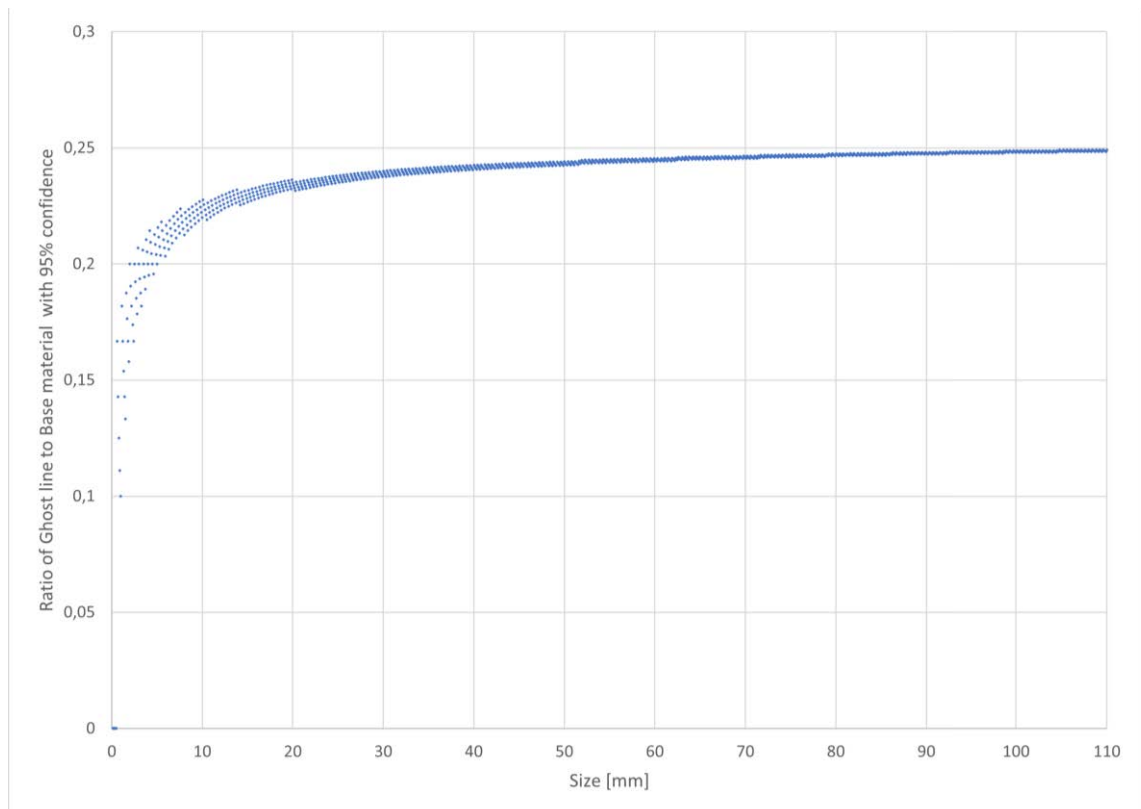


Figure 59 Sample size and the expected ratio of base material to line regions with 95% confidence.

The 10 mm sample size has not reached convergence, which would require a sample size of ~10 cm after which any increase would not result in meaningful differences between ghost line and base material ratios. The ratio for 10 mm samples is still quite close at ~0.22 so the uneven effect of ghost lines should not be large due to their uneven distribution between specimens.

When the fracture probability of Figure 47 is observed, there could be a weaker region around locations 9 and 10, but there is also local variation, so any toughness gradient in the material is inconclusive. When the Master Curve graphs are observed the HC-series has a small spread compared to the previous results presented in Figure 56. If the high

toughness values are omitted from the LC-series, it too has a tight distribution. The tougher values introduce a bimodal spread where there are no values in between the two clusters which should be unlikely. Wallin (2011) states that omitting results from the statistical distribution will skew the expected results, as extreme values are ignored. However, the presence of bimodal distribution due to material inhomogeneities should be found in both specimen types, which is not the case. From this it can be deduced that the bimodal distribution has more to do with the method, measuring capacity, and fracture mechanism rather than material inhomogeneities related to crack initiation sites.

The largest method related unreliability is speculated to result from the clamping and the positioning of the specimen within them. Even though the clamps were exactly 10W away from each other, it still allows the possibility for the sample to be placed unsymmetrically, so that the crack is closer to one clamp than the other, while the distance between clamps is the desired 10W. There is also the problem to misalign the sample in the rotational direction allowed by the clamps. The highest placement related uncertainty comes from the horizontal misalignment of the specimen. If the specimen ligament centerline is skewed to either side of the machine load line, a significant moment will arise, Figure 60. The clamped surfaces did not show any slippage due to rotation, nor was there any visible twisting observed during the tests. Even so, the load line alignment was done based on markings on the clamps which were difficult to locate when the cooled chamber had condensed frost covering its surfaces.

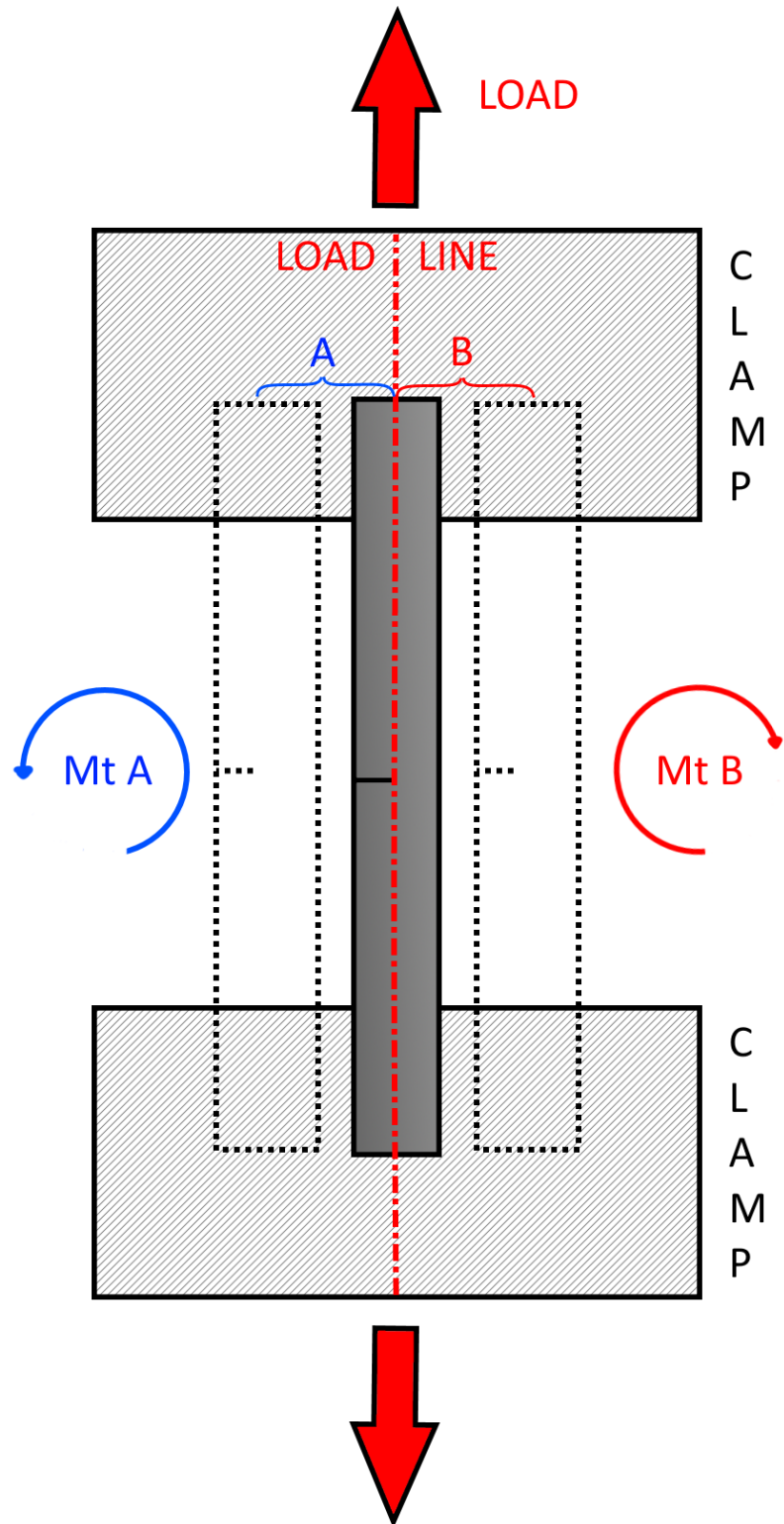


Figure 60 Arising moment forces due to the misalignment in relation to the load line (red).

The pre-crack estimation ($a_{0\text{est}}$) is ordinarily done with the unloading compliance method elastic rebound gradient, but this was not possible with the equipment used in this thesis. The method is affected by the machine flex and the stiffness of the test system can be adjusted based on the unloading compliance results. If the C_θ gradient is used as a basis of estimation, the crack sizes would require E adjustments beyond the allowable 10% limit. Since there is no crack growth, the estimated crack length matches the post experiment measurements and if it is substituted, the E which would produce such crack estimates can be calculated (E machine). The different values are presented in Appendix 6, but were not used in the thesis calculations, instead the KTH value of 213 GPa was used.

If the CMOD values are compared to the tensile machine displacement there seems to be two regions in the graph they form. One where the slope is steep and the CMOD values increase slowly compared to the displacement, but after a curved section the CMOD values increase without as much machine displacement, Figure 61

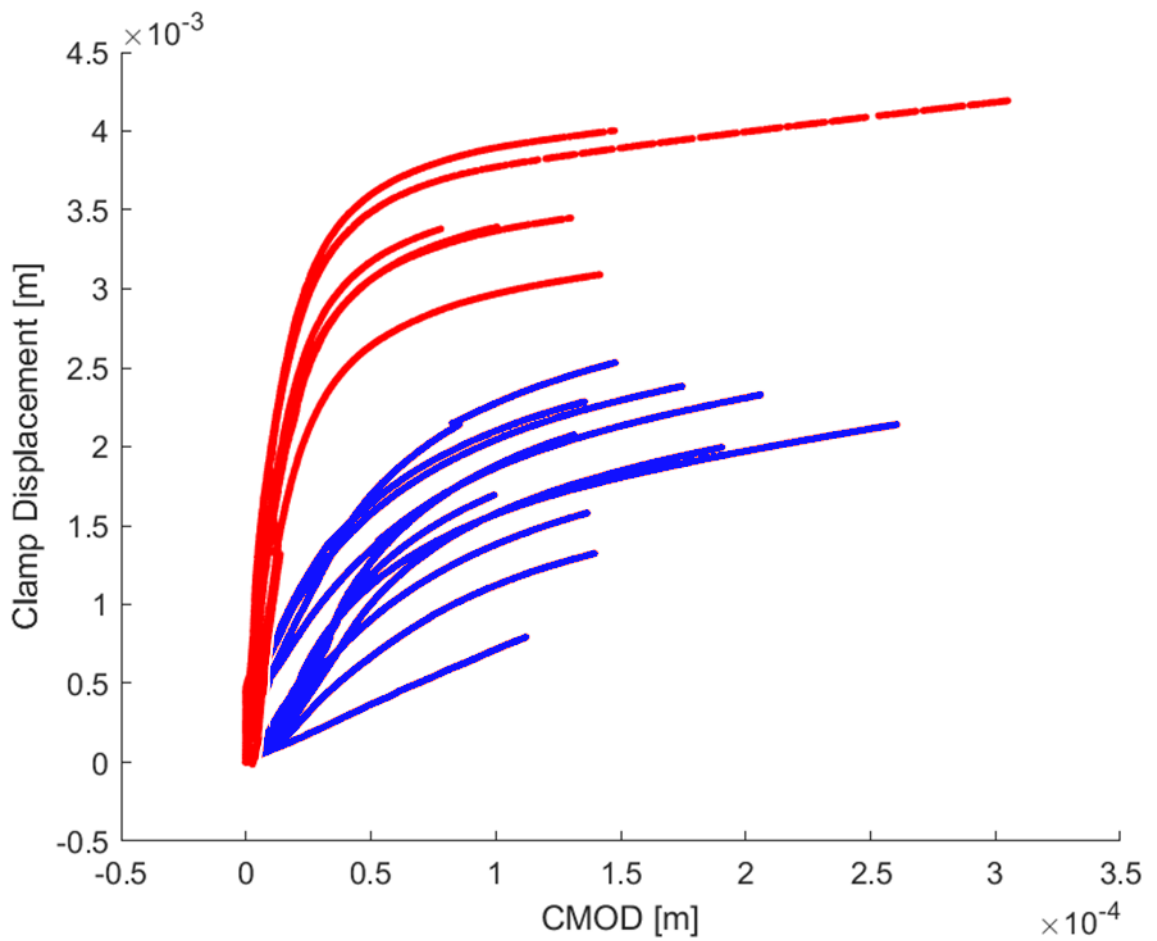


Figure 61 CMOD machine displacement, corrected for elastic elongation, HC-series in blue, LC-series in red.

The deviation could be due to multiple reasons such as slip, plasticity, crack growth, rotation, or a combination of them. Since no traces of growth, slip, or plasticity were found, the effect of rotation cannot be excluded. As is, the methods used in the thesis do not account for the machine rotation effecting the toughness results and no correction solutions were found from literature, and if they existed, they would likely be set-up specific.

The sample plasticity was estimated using the plasticity limits retrieved from the work of Kanninen and Popelar (1985), Table 13, but their suitability for the thesis evaluation is unknown. Only the three high toughness specimens (LC7, LC8, and LC11) exceed the

plasticity load limit. What is particularly striking, is the fact that for these three specimens the maximum stress exceeds 740 MPa when the tested ultimate tensile stress was around 730 MPa. What allows for such an increase in strength in a notched specimen is unknown but could be the result of true stress being higher than the one reported by KTH. As with the rotation, the effect of plasticity was not concisely discovered in the thesis examination.

Table 13 Load limit results (Kanninen and Popelar, 1985)

| LEGEND | Force [N] | Stress [MPa] | Plasticity lim P- σ | Plasticity lim P- ϵ |
|--------|-----------|--------------|----------------------------|------------------------------|
| LC1 | 47950 | 714 | 50292 | 37054 |
| LC2 | 47956 | 726 | 49797 | 36689 |
| LC3 | 47001 | 716 | 48505 | 35737 |
| LC4 | 47536 | 728 | 49430 | 36419 |
| LC5 | 45272 | 689 | 47952 | 35330 |
| LC6 | 46830 | 699 | 50013 | 36848 |
| LC7 | 49041 | 781 | 46627 | 34353 |
| LC8 | 47901 | 757 | 46762 | 34453 |
| LC9 | 43886 | 697 | 44964 | 33128 |
| LC10 | 44805 | 687 | 48622 | 35823 |
| LC11 | 48872 | 745 | 49001 | 36103 |
| HC1 | 23329 | 588 | 15117 | 11138 |
| HC2 | 14815 | 390 | 13440 | 9902 |
| HC3 | 16843 | 447 | 13192 | 9720 |
| HC4 | 17513 | 464 | 13402 | 9874 |
| HC5 | 19556 | 503 | 13945 | 10274 |
| HC6 | 19418 | 511 | 13565 | 9995 |
| HC8 | 19942 | 518 | 13570 | 9998 |
| HC9 | 18315 | 477 | 13814 | 10178 |
| HC10 | 16628 | 416 | 15200 | 11199 |
| HC11 | 19178 | 502 | 13540 | 9976 |
| HC12 | 17075 | 448 | 13578 | 10004 |

Possibly the biggest fault of the uncertainty analysis is, that it evaluates the sensitivities of the calculation formulas, but reveals nothing of their actual suitability to the test procedure. The GUM method was used for the propagation of uncertainty estimation, but the formula, which was evaluated omitted some parameters. The calculations it employs do not take into account procedural sources for uncertainty, such as the clamping of the sample. The effect of clamping could be evaluated with large enough datasets for the

same test setup, but comparison between laboratories would be difficult and the number of specimens needed to be tested would be impractical.

The side groove depth was omitted from the final uncertainty calculations to reduce their dimensionality, but the sensitivity analysis highlighted their significance on a local scale. When the larger ranges from the experimental are evaluated, the Sobol indices reflect the uncertainty results obtained with the partial derivatives method and confirms the plastic area as the most significant contributor to the overall toughness result in the test range and variance. The width and thickness are the second most important, possibly due to the normalization of many formulas over the width values. An additional difference between the global sensitivity and propagation of uncertainty can be seen in the second order term significance. It is almost zero for the Sobol's indices while having a larger effect on the partial derivatives method. The reason for the differences between the two methods are most likely caused by the different number of parameters and the proportion of uncertainty which is combined when fewer parameters are used. Another significant omission is the missing covariance analysis, which was deemed beyond the thesis scope.

The accuracy of the FEM model is not evaluated to any high degree, rather convergence in results while changing parameters was used to ensure the model was as accurate as reasonably possible. When the Q-parameter is considered, there is a gradient of over 100 MPa per 0.1 mm when moving in the X-direction from the crack tip. As a result, a small error in the normalized radius can result in relatively significant changes (5% - 10 %, 2-4 °C) in the end estimate. Since the model is only used as a reference between the two specimen types, any estimation errors are assumed to affect the results equally.

One of the biggest challenges for the thesis results, is the hidden effect of many uncontrolled or unquantified parameters. When compared to previous, results the difference between them and the current results cannot be parsed into the individual factors behind it. For example, the SE(N)T specimen has a different constraint to the previous SEB specimens, Figure 56. However, other factors such as the sample orientation and different profile also effect their toughness results, but their exact degree of the overall difference cannot be deduced. When the constraint is compared between the thesis experiments where the procedure and material is more identical, the effect of

each controlled parameter can be evaluated more precisely. The difference in the T_0 temperature shift between the FEM models is 29 °C and 44 °C for the experimental results. The uncertainty in the experimental results allows for this difference, but additional factors besides constraint likely explain parts of the deviation. Rotation is a likely candidate to explain the difference as the HC series samples are less stiff due to their smaller ligament. When the constraint values are compared to those presented by Moattari and Sattari-Far (2017), Figure 57, the constraint for the thesis samples is higher, but the a/W 0.2 samples seem to follow a similar load- Q sensitivity (gradient). Comparison between two FEM- models has the additional benefit of having no uncontrolled effects from the surroundings.

The thesis experimental results highlight the effect, which constraint has on the fracture toughness. The HC-series toughness is lower than a/W 0.5 SEB specimens which are expected to be more conservative. The HC-series toughness is closer to the C(T) series results which is considered the highest constraint test configuration. No explanation to the brittleness was found from the fracture surfaces or material analysis, and the tight spread of the results would indicate that the material is homogenous. The LC-series on the other hand is tougher than the comparison results. What causes this large contrast in toughness is unknown, but the SE(N)T specimens in the thesis test configuration seem sensitive to crack length with regards to constraint and that constraint effects are indeed present at the specimen scales. It should be noted, that increasing the crack length also reduces the stiffness of the tensile setup, and it could be concluded that the toughness values are sensitive to the test setup stiffness.

7 CONCLUSION

This thesis explored the fracture toughness of an ASTM A533B Class 1 pressure vessel steel from the IAEA correlation monitoring material melt designated JRQ and the effect changing constraint has on it. Through a literature review, important theory relating to fracture toughness determination was evaluated. A miniature SE(N)T type specimen was designed for the available test apparatus based on the examined standards. It represents a less conservative method compared to bending type specimens more commonly tested as it has a lower constraint due to its tensile loading producing less moment forces.

The specimens had a 10 mm x 10 mm square cross section and a T-L orientation. The effect of constraint on the specimen was varied in the experimentation by altering the a/W ratio, 0.2 for low, and 0.5 for high constraint series. A complementary FEM analysis was conducted on Abaqus CAE and it was used to calculate Q-parameters with a HRR reference field. A Ramberg-Osgood material model derived from KTH tensile tests was used for the Abaqus model with a strain hardening exponent of 9 and yield strength of 488 MPa.

The sample material was characterized through optical and electron microscopy and previous observations. The mechanical properties were verified using HV 10 measurements which showed no statistically significant differences based on sample location. The sample detachment was also alternated to account for material inhomogeneities. The microstructure was bainitic with a grain size between 20 and 45 μm , an average hardness of 195 HV10 and a yield strength of 488 –560 MPa. Inclusions identified as aluminum oxide and manganese sulfide were also found.

The fracture toughness was evaluated using the Master curve method and the T_0 transition temperature. In total 11 low and 12 high constraint specimens were tested at -85 °C. Three specimens from the low and two from the high constraint series were used for procedure calibration.

The T_0 temperature was found to be $-54\text{ }^\circ\text{C}$, $\sigma\ 8,5\text{ }^\circ\text{C}$ for the high constraint series with a Q-parameter of -0.59 which correlates to a $-14\text{ }^\circ\text{C}$ shift in the T_0 temperature. A shift of $-5.5\text{ }^\circ\text{C}$ is predicted using T-stress as the constraint parameter. The spread of the toughness results was small.

The low constraint series exhibited a bimodal distribution with results in two clusters, five in the high and six in the low cluster. If all the samples excluding calibration specimens are used to derive the T_0 temperature, it is $-113\text{ }^\circ\text{C}$, $\sigma\ 4\text{ }^\circ\text{C}$. If the three tougher samples are censored in addition, the T_0 temperature becomes $-98\text{ }^\circ\text{C}$, $\sigma\ 5\text{ }^\circ\text{C}$. The Q-parameter is -1.15 which correlates to a $-43\text{ }^\circ\text{C}$ shift in the T_0 temperature. A shift of $-21.6\text{ }^\circ\text{C}$ is predicted using T-stress as the constraint parameter. However, the five remaining samples are not enough to derive a reliable Master Curve distribution from.

The uncertainty of the results was estimated using a partial derivatives method complimented by a global sensitivity analysis using Sobol's indices. The most significant factor for fracture toughness was determined to be the plastic area under the CMOD-Force graph used in J-integral calculations.

The Abaqus predicted T_0 difference between the series was $-29\text{ }^\circ\text{C}$ while the measured was $-44\text{ }^\circ\text{C}$. The difference is within the uncertainty margins, but unaccounted for rotation in the tensile test machine is presumed to have affected the results.

Compared to previous toughness results, the low constraint series had a very low T_0 temperature while the high constraint series was quite brittle. Based on these results, the SE(N)T geometry seems to be sensitive to constraint changes at the miniature scale

8 REFERENCES

- Anderson, T. L. (2005). *Fracture Mechanics - Fundamentals and Applications* (third). CRC Press.
- Anderson, T. L. (2017). *Fracture Mechanics - Fundamentals and Applications* (fourth). CRC Press.
- Argon, A. S., Im, J., & Safoglu, R. (1975). Cavity Formation from Inclusions in Ductile Fracture. *Metallurgical Transactions, A6*, 825–837.
- ASM Handbook Committee. (1999). *ASM Handbook - Volume 12 - Fractography* (Vol. 12). ASM international.
- ASTM International. (2020). *E1820-20b Standard Test Method for Measurement of Fracture Toughness*. ASTM International.
- ASTM International. (2021). *E1921-21 Standard Test Method for Determination of Reference Temperature, T_0 , for Ferritic Steels in the Transition Range*. ASTM International.
- ASTM International. (2022). *E399-22 Standard Test Method for Linear-Elastic Plane-Strain Fracture Toughness of Metallic Materials*. ASTM International.
- Boåsen, M. (2021). *Dragprovning av ASTM A533B*.
- British Standards Institution. (2014). *BS 8571:2014 Method of test for determination of fracture toughness in metallic materials using single edge notched tension (SENT) specimens*. BSI Standards Limited.
- Brooks, C. R., & Choudhury, A. (1993). *Metallurgical Failure Analysis* (Robert. W. Hauserman, Ed.). McGraw-Hill.

- Brumovsky, M., Davies, L. M., Kryukov, A., Lyssakov, V. N., & Nanstad, R. K. (2001). *Reference manual on the IAEA - JRQ correlation monitor steel - for irradiation damage studies IAEA-TECDOC-1230*.
- Chastaing, G., Gamboa, F., & Prieur, C. (2012). Generalized Hoeffding-Sobol Decomposition for Dependent Variables - Application to Sensitivity Analysis. *Electronic Journal of Statistics*, 0, 2420–2448.
- Dally, J. W. (2008). 11. Statistical Analysis of Experimental Data. In W. N. Jr. Sharpe (Ed.), *Springer Handbook - of Experimental Solid Mechanics* (pp. 259–280). Springer.
- Dassault Systemes SIMULIA Corp. 2022. Abaqus CAE. [Computer Program]. Johnston (RI): Dassault Systemes SIMULIA Corp.
- Dodds, R. H., Shih, C. F., & Anderson, T. L. (1993). *Continuum and Micromechanics Treatment of Constraint in Fracture*.
- Goods, S. H., & Brown L, M. (1979). The nucleation of Cavities by Plastic Deformation. *Acta Metallurgica*, 27, 1–15.
- Griffith, A. A. (1921). The phenomena of rupture and flow in solids. *Philosophical Transactions of the Royal Society of London. Series A*, 221(582–593), 163–198.
- HBK. (n.d.). *How to Select the Right Adhesive for your Strain Gauge Installation*. Retrieved May 11, 2022, from <https://www.hbm.com/en/4314/selecting-adhesives-for-strain-gauge-installation/>
- Herman, J., & Usher, W. (2017). An open-source Python library for sensitivity analysis. In *Journal of Open Source Software* (Vol. 2, Issue 9).
- Hertzberg, R. (1976). *Deformation and Fracture Mechanics of Engineering Materials*. John Wiley & Sons.

- Hwang, B., Suh, D.-W. & Kim, S.-J., 2011. Austenizing temperature and hardenability of low-carbon boron steels. *Scripta Materialia*, 64(12), pp.- 11181120.
- Ikonen, K., & Kantola, K. (1991). Johdatus Murtumismekaniikkaan. In *Murtumismekaniikka 804* (second). Otatiето. pp. 14–19).
- Inagawa, T., Usher, W., & Herman, J. (2022). Toward SALib 2.0: Advancing the accessibility and interpretability of global sensitivity analyses. In *Socio-Environmental Systems Modelling* (Vol. 4, p. 18155).
- Kanninen, M. F., & Popelar, C. H., (1985). *Advanced Fracture Mechanics*. Oxford University Press.
- Kantidis, E., Marini, B., & Pneau, A. (1994). A CRITERION FOR INTERGRANULAR BRITTLE FRAC(T)URE OF A LOW ALLOY STEEL. *Fatigue and Fracture of Engineering Materials and Structures*, 17(6), 619–633.
- Kaufmann, D. (2011). *Size Effects on the Plastic Deformation of the BCC-Metals Ta and Fe*. Karlsruhe Institute of technology.
- Krishnaswamy, R.-C. (2008). 5. Fracture Mechanics. In W. N. Jr. Sharpe (Ed.), *Springer Handbook - of Experimental Solid Mechanics*. Springer. (pp. 125–158).
- Lindqvist, S., & Boåsen, M. (2019). *Constraint and fracture toughness*.
- Lindqvist, S., & Kuutti, J. (2022). Sensitivity of the Master Curve reference temperature T_0 to the crack front curvature. *Theoretical and Applied Fracture Mechanics*, 122, 1–22.
- Lindqvist, S., & Peltonen, V. (2021). *NKS: Fracture toughness behaviour in the ductile-to-brittle transition region - small and large specimens and shallow and long cracks*.
- MATLAB. 2022. MATLAB R2022b. [Computer Program]. Natick (MA): MathWorks

- Moattari, M., & Sattari-Far, I. (2017). Modification of fracture toughness Master Curve considering the crack- tip Q-constraint. *Theoretical and Applied Fracture Mechanics* 90, 43–52.
- Newton, I. (2016). *The Principia: The Authoritative Translation: Mathematical Principles of Natural Philosophy* (Bernard. I. Cohen & A. Whitman, Eds.). University of California Press.
- O’Dowd, N. P., & Shih, C. F. (1991). Family of crack-tip fields characterized by a triaxiality parameter—I. Structure of fields. *Journal of Mechanics and Physics of Solids*, 39(8), 989–1015.
- O’Dowd, N. P., & Shih, C. F. (1992). Family of crack-tip fields characterized by a triaxiality parameter-II. Fracture applications. *Journal of Mechanics and Physics of Solids*, 40(5), 939–963.
- Paavola, J.-M., Kinnunen, A., Tanhua, I., & Rautiainen, T. (2021). *Ilmasto- ja energiastrategian sukupuolivaikutusten arviointi*. <http://urn.fi/URN:ISBN:978-952-327-887-5>
- Paloneva, M., & Takamäki, S. (2021). *Summary of sectoral low-carbon roadmaps*. https://julkaisut.valtioneuvosto.fi/bitstream/handle/10024/162851/TEM_2021_9.pdf?sequence=1&isAllowed=y
- Panico, M., Tang, H., Fairchild, D. P., & Cheng, W. (2017). ExxonMobil SENT test method and application to Strain-Based Design. *International Journal of Pressure Vessels and Piping*, 156, 17–22.
- Park, D.-Y., Tyson, William. R., & Gravel, J.-P. (2017). CANMET SENT test method, updates and applications. *International Journal of Pressure Vessels and Piping*, 156, 8–16.
- Petrangeli, G. (2020). *Nuclear Safety* (second). Butterworth-Heinemann.

- Rice, J. R., (1968) A Path Independent Integral and the Approximate Analysis of Strain Concentration by Notches and Cracks. *Journal of Applied Mechanics*, 35(2), 379-388.
- Rice, J. R., Rosengren, G. F., (1968) Plane Strain Deformation Near a Crack Tip in a Power-Law Hardening Material. *Journal of Applied Mechanics*, 16(1), 112.
- Rohrer, G. S. (2001). Metallic Bonding. In *Structure and Bonding in Crystalline Materials*. Cambridge University Press. (pp. 326–362).
- Ruggieri, C. (2012). Further results in J and C(T)OD estimation procedures for SE(T) fracture specimens – Part I: Homogeneous materials. *Engineering Fracture Mechanics*, 79, 245–265.
- Ruggieri, C. (2017). Low constraint fracture toughness testing using SE(T) and SE(B) specimens. *International Journal of Pressure Vessels and Piping*, 156, 23–39. <https://doi.org/10.1016/j.ijpvp.2017.07.003>
- Sarzosa, D. F. B., Savioli, R., Ruggieri, C., Jivkov, A., & Beswick, J. (2018). A local approach to assess effects of specimen geometry on cleavage fracture toughness in reactor pressure vessel steels. *American Society of Mechanical Engineers, Pressure Vessels and Piping Division (Publication) PVP*, 6B-2018. <https://doi.org/10.1115/pvp2018-85063>
- Säteilyturvakeskus. (2020). *GUIDE YVL E.4 STRENGTH ANALYSES OF NUCLEAR POWER PLANT PRESSURE EQUIPMENT*. <https://www.stuklex.fi/en/ohje/YVLE-4>
- Shen, C., Wang, C., Wei, X., Li, Y., van der Zwaag, S., & Xu, W. (2019). Physical metallurgy-guided machine learning and artificial intelligent design of ultrahigh-strength stainless steel. *Acta Materialia*, 179, 201–214.

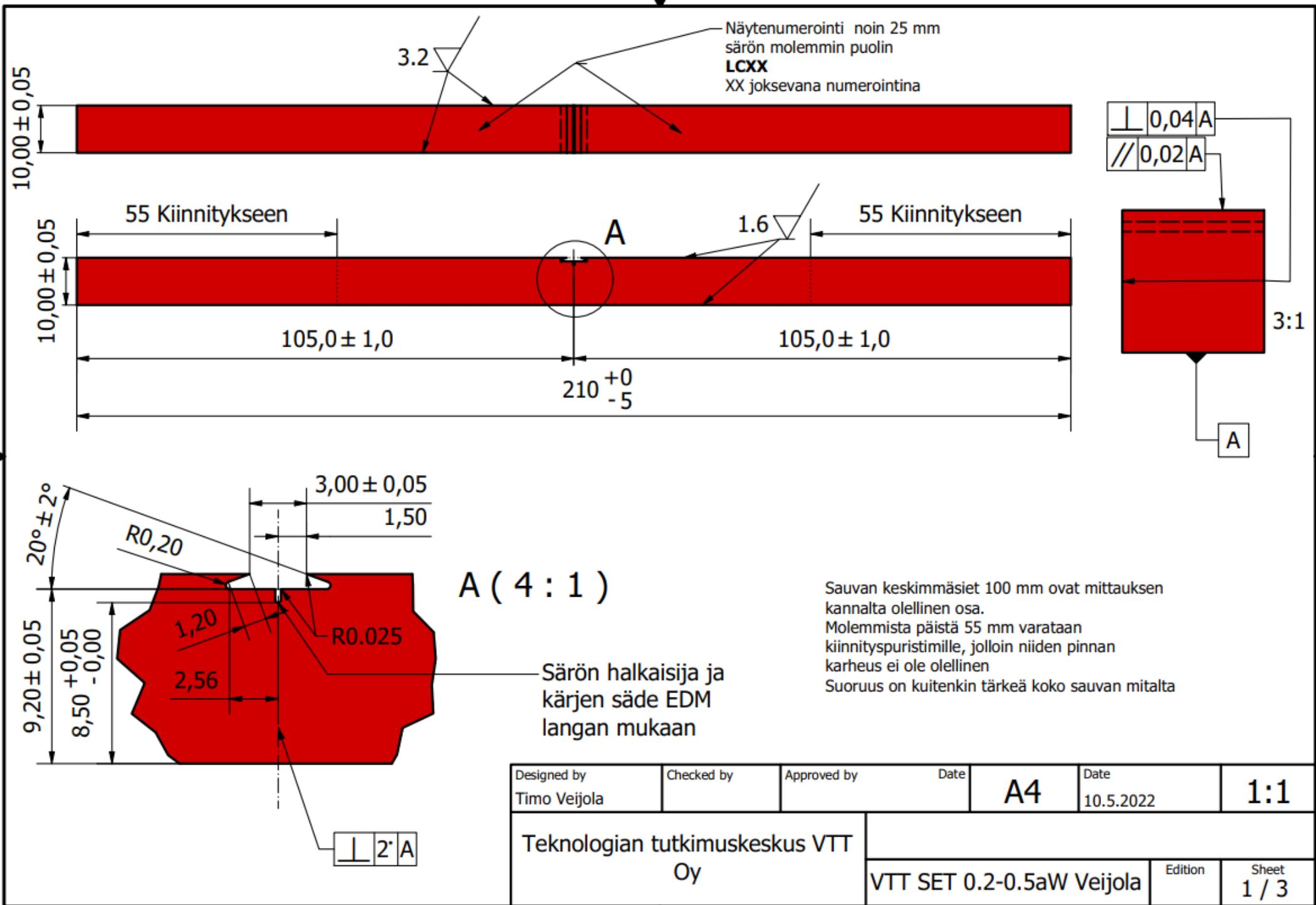
- Tosin, M., Côrtes, A., & Cunha Jr, A. (2020). A Tutorial on Sobol' Global Sensitivity Analysis Applied to Biological Models. In M. A. B. da Silva, N. Carels, M. Trinade dos Santos, & F. J. P. Lopez (Eds.), *Networks in Systems Biology: Applications for Disease Modeling-Computational Biology*. Springer. (Vol. 32, pp. 93–118).
- Työ- ja Elinkeinoministeriö. (2022, March 18). *Ydinlaitoksia ovat ydinvoimalaitokset ja ydinjätehuollon laitokset*. <https://tem.fi/ydinlaitokset-ja-ydinenergiahankeet>
- Uchic, M. D., Dimiduk, D. M., & Florando, J. N. (2004). Sample dimensions influence strength and crystal plasticity. *Science*, 305(5686), 986–989.
- Wallin, K. (2011). *Fracture Toughness of Engineering Materials - Estimation and Application*. EMAS Publishing.
- Wallin, K., Valo, M., Rintamaa, R., Törrönen, K., & Ahlstrand, R. (1995). Descriptive characteristics of different types of test for irradiation embrittlement. In *Nuclear Engineering and Design* (Vol. 159).
- Weeks, T. S. (2017). Measurement techniques and procedures for standardized SE(T) testing of pipeline steel. *International Journal of Pressure Vessels and Piping*, 156, 59–67.
- Working Group 1 of the Joint Committee for Guides in Metrology. (2008a). *Evaluation of measurement data - Guide to the expression of uncertainty in measurement* (pp. 1–120). Joint Committee for Guides in Metrology.
- Working Group 1 of the Joint Committee for Guides in Metrology. (2008b). *Evaluation of measurement data - Supplement 1 to the "Guide to the expression of uncertainty in measurement" - Propagation of distributions using Monte Carlo method* (pp. 1–77). Joint Committee for Guides in Metrology.

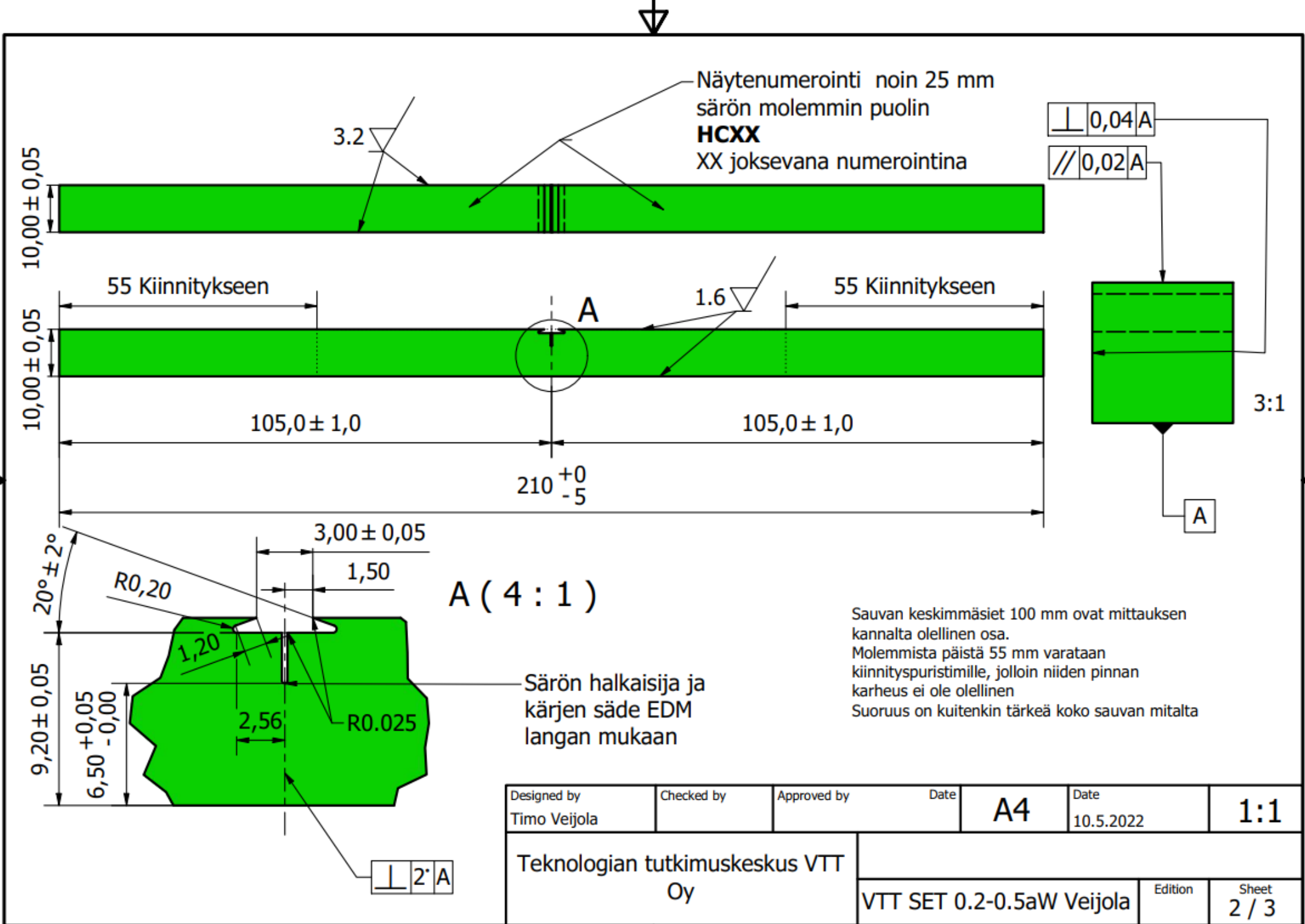
Yahya, O. M. L., Borit, F., Piques, R., & Pineau, A. (1998). Statistical modelling of intergranular brittle fracture in a low alloy steel. *Fatigue and Fracture of Engineering Materials and Structures*, 21(12), 1485–1502.

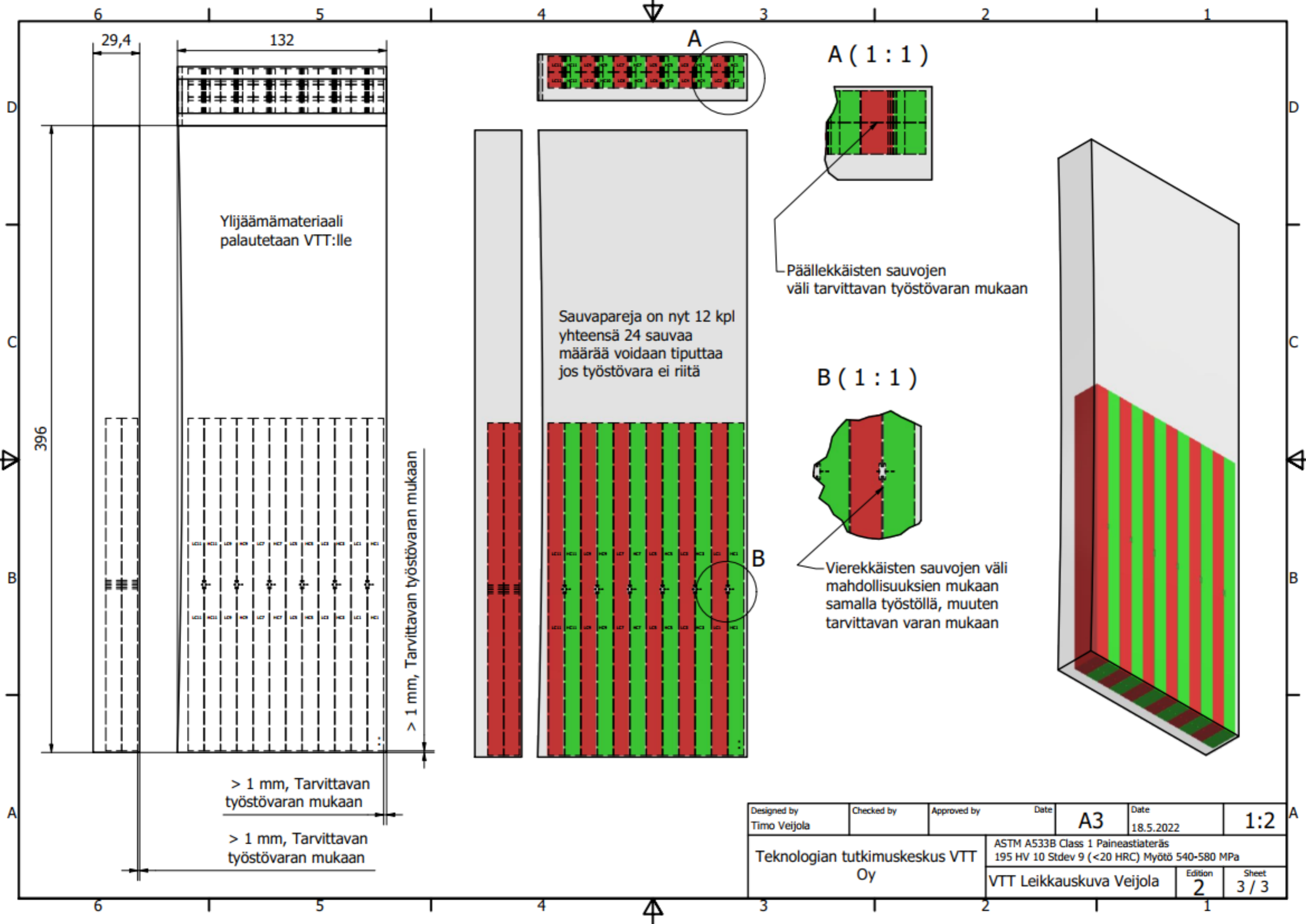
Ydinenergialaki, Pub. L. No. 7 r § (2021).

<https://www.finlex.fi/fi/laki/ajantasa/1987/19870990#L2aP7r>

Appendix 1 Technical drawings and instructions







Ylijäämämateriali palautetaan VTT:lle

Sauvapareja on nyt 12 kpl yhteensä 24 sauvaa määrää voidaan tiputtaa jos työstövara ei riitä

Päällekkäisten sauvojen väli tarvittavan työstövaran mukaan

Vierekkäisten sauvojen väli mahdollisuuksien mukaan samalla työstöllä, muuten tarvittavan varan mukaan

> 1 mm, Tarvittavan työstövaran mukaan

> 1 mm, Tarvittavan työstövaran mukaan

| | | | | | |
|-----------------------------------|------------|-------------|---|-------------------|-----|
| Designed by Timo Veijola | Checked by | Approved by | Date A3 | Date 18.5.2022 | 1:2 |
| Teknologian tutkimuskeskus VTT Oy | | | ASTM A533B Class 1 Paineastiateräs 195 HV 10 Stdev 9 (<20 HRC) Myötö 540-580 MPa | | |
| VTT Leikkauskuva Veijola | | | Edition 2 | Sheet 3 / 3 | |

Appendix 2 MATLAB Code

The full version can be requested from the author

```
% Timon Veijola, Master's thesis measurement data analysis code

clear % clears previous variables
close all % closes all open figures
start_time = datestr(now, 'HH:MM:SS') % Displays the starting time of the run
tic %timer start
%% ////////// DATA FETCHING //////////
%% ////////// STORES //////////
%% ////////// ANALYSIS LOOPS //////////
%% ////////// MODEL PARAMETERS //////////
%% ////////// DATA FILTERING //////////
%% ////////// DATA PROCESSING FOR PLOTTING //////////

    % Picks table columns for graphs
    xx = Results.CMOD; % table2array(Results(:, "CMOD"));
    yy = Results.kN; %table2array(Results(:, "kN"));
    zz = table2array(Results(:, 's'));

    fi = fit(xx,yy, 'poly9'); %, 'Normalize', 'on'); % Fits a curve through the
measurements
    MCFS = coeffvalues(fi); % extract coefficients from the fit function
        p1 = MCFS(1); p2 = MCFS(2); p3 = MCFS(3); p4 = MCFS(4); p5 =
        MCFS(5); p6 = MCFS(6);
        p7 = MCFS(7); p8 = MCFS(8); p9 = MCFS(9); p10 = MCFS(10); %p11 =
MCFS(11); %coefficients from the function

    %scatter(Results2.COD,Results2.kN,'green')fi
    ff = fit(xx,yy, 'poly1'); %fits a linear line through the data for
comparison
%% ////////// FRACTURE MATHEMATICS //////////

    fm = max(Results.kN); %maximum load [N]

    row = find(yy == fm); % location/index of the maximum load

    dm = table2array(Results(row, "CMOD")); % CMOD corresponding to the
maximum load

    str = (fm)/((W-a0)*BN); %max stress [MPa]

    %Ee = str/dm;

    %Geometric factors Many formulas are from ASTM E 1920 section 9, values
for
    %SET specimens from CANMET

    aw = a0/W;%table2array(SETs(k, "Var6")); % Precrack ratio
```

```

faw1 = 1.197-2.133*(aw)+23.886*aw^2-69.051*aw^3+100.462*aw^4-41.397*aw^5
...
-36.137*aw^6+51.215*aw^7-6.607*aw^8-
52.322*aw^9+18.574*aw^10+19.465*aw^11; %geometric factor for SET according to
CANMET

eps = (pi*a0)/(2*W); %variable for geometric factor 2

faw2 = ((0.752+2.02*aw+0.3695*(1-sin(eps))^3)/cos(eps))* ...
((tan(eps)/eps)^0.5);% geometric factor according to The Stress
analysis of cracks handbook (Tada, Irwin, Paris) 1973

K_el = ((fm*0.001*(pi*a0* ...
0.001)^0.5)/(W*(B*BN*10^-6)^0.5))*faw1; %stress intensity factor for
the elastic portion [MPa*m^0.5]
%% ////////// a ESTIMATE AND E CORRECTION//////////
%% ////////// KJC CALCULATION//////////

Je = ((1-v^2)*K_el^2)/E; %elastic J integral

b0 = W-a0; %ligament length

f = matlabFunction(f); %converts the fit function from symbolic

Area = integral(f,min(Results.CMOD),CMODmax); % area under the fit
function

offset =(diff(Results.CMOD)); % Difference between subsequent values of
CMOD

offset(end+1) = 0; %to resize the vector that lost one value

neg_offset = offset < -0.00006; % Limit to remove Clip opening CMODs

offset(neg_offset) = 0; % Changes errors to 0

AreaB = offset.*(Results.kN); % difference * force

AreaBB = sum(AreaB); %LIDL integration/Lower rectangle integration summs
all the "rectangles" formed by force * difference

uAreaB = abs(Area-AreaBB)/Area; % method difference 2
%% ////////// QUASISTATIC LOAD TEST //////////
%% ////////// PLASTIC VARIABLES //////////
%Coefficients for SET specimen calculations

eta = 1-1.089*aw+9.519*aw^2-48.572*aw^3+109.225*aw^4-73.116*aw^5-
77.984*aw^6 ...
+38.487*aw^7+101.401*aw^8+43.306*aw^9-110.770*aw^10;

%n1ld1 = -0.880+15.19*aw-35.44*aw^2+18.644*aw^3+18.399*aw^4-1.273*aw^5-
12.756*aw^6 ...
-12.202*aw^7-4.447*aw^8+5.397*aw^9+14.187*aw^10;

%n1ld2 = 15.19-35.44*2*aw+3*18.644*aw^2+4*18.399*aw^3-1.273*5*aw^4-
12.756*6*aw^5 ...
-12.202*7*aw^6-4.447*8*aw^7+5.397*9*aw^8+14.187*10*aw^9;

```



```

%y1ld = n1ld1-1-(1-aw)*(n1ld2/n1ld1);

Ae = 0.5*C0*(fm)^2; % elastic area

Ap2 = Area-Ae; % Area of the plastic proportion of the CMOD-Curve

Ap3 = Area -(0.5*fm*(CMODmax-(-(Results.kN(find(Results.CMOD ==...
      CMODmax))-kappa*CMODmax)/kappa))); % Alternative calculation method

Jp = ((eta*Ap2)/(BN*b0))*1000; %*(1-((y1ld*a0)/b0))*1000; % J integral
for the plastic part

Jc = Je+Jp; % J integral for the critical load

Kjc = (Jc*(E/(1-v^2)))^0.5; %Kritical stress intensity

KjcT = 20+(Kjc-20)*(B/25.4).^0.25; %Kjc scaled to 1T size

%K0 = (1/(length(SelectFile)))*(KjcT-20)^4; % Single temperature
%calculation variable

Tavg = mean(Results.C([1:(length(Results.kN)-3*cen)])); %Average test
temperature

AAB = (Area-AreaBB)/Area; %Comparison between the 2 integartion methods,
if they are far apart something is wonky in the fit, data or both

%% ////////// STORED VALUES //////////
%% Calculation formula

% KjcT is the Kjc scaled to 1 inch combined into a single formula
respective to all the measured quantities* Some measured quantities are
procesed such as the force CMOD graph that produce the Ap value

Kjc_T = @(a_0,W_,B_,T_,A_p) ( ...
(((1-v^2)*((fm*0.001*(pi*a_0*0.001)^0.5)/(W_*(B_*(BN)*10^
6)^0.5)))*(1.197-2.133*((a_0/W_))+23.886*(a_0/W_)^2-69.051*(a_0/W_)^3 ...
+100.462*(a_0/W_)^4-41.397*(a_0/W_)^5-
36.137*(a_0/W_)^6+51.215*(a_0/W_)^7-6.607*(a_0/W_)^8-
52.322*(a_0/W_)^9+18.574*(a_0/W_)^10 ...
+19.465*(a_0/W_)^11)^2)/((204-T_/16))+ ... %Je
(((1-1.089*(a_0/W_)+9.519*(a_0/W_)^2-
48.572*(a_0/W_)^3+109.225*(a_0/W_)^4-73.116*(a_0/W_)^5-77.984*(a_0/W_)^6 ...
+38.487*(a_0/W_)^7+101.401*(a_0/W_)^8+43.306*(a_0/W_)^9-
110.770*(a_0/W_)^10)*(A_p))/((BN)*(W_-a_0))*1000));% ... %Jp

%val =(Kjc_T(2.089187500000000,9.984000000000000,9.983000000000000, -
144,5.915)); % Validating the formula through comparison to a known result
~116

%% First and second order uncertainty calculations

%Ap = A-0.5*C0*fm^2;

```

```

xi = {'a_0','W_','B_','T_','A_p'}; % variables
ui = [u2,u3,u4,u6,u7_]; % standard uncertainties for each variable

% stores for loop values
h_expr = [];
h_expr2 = [];
h_expr3 = [];
h_expr4 = [];
h_expr5 = [];
hhh = [];
PartialSums = [];

syms f(a_0,W_,B_,T_,A_p) fd(a_0,W_,B_,T_,A_p)

%tic % timer start

for d = (1:5) % creates partial derivatives of the function with respect
to all parameters

    d;

    f(a_0,W_,B_,T_,A_p) = Kjc_T;

    fd(a_0,W_,B_,T_,A_p) = (diff(f,xi(d))); % *ui(k);

    h_expr2 = [h_expr2; fd(a_0,W_,B_,T_,A_p)];

    ucl(a_0,W_,B_,T_,A_p) = (diff(f,xi(d)))^2*ui(d);

    h_expr5 = [h_expr5; ucl(a_0,W_,B_,T_,A_p)];
end

    FirstUc = zeros(1,5);

for q = 1:5 % Variance values for each first order uncertainty component
for validation purposes

    ggg = h_expr5(q);

    kk = symfun(ggg,[a_0,W_,B_,T_,A_p]);

    FirstUc(q) = round(vpa((kk(a0,W,B,T(k-Loopstart+1),Ap2))),5);
end

for l = (1:5) % creates second order partial derivatives of the
function with respect to all parameters

    l;

    f(a_0,W_,B_,T_,A_p) = Kjc_T;

    fd(a_0,W_,B_,T_,A_p) = (diff(f,xi(l),2)); % *ui(k);

    h_expr3 = [h_expr3; fd(a_0,W_,B_,T_,A_p)];
end

a = [1,2,3,4,5]; % vector used for the loop

```

```

    comb = nchoosek(a,2); % creates all the combinations of 2 parameters,
    used for indexing in the loop

    for h = 1:10 % creates the 2 parameter interactions of the standard
    uncertainty formula  $1/2'(f''/xi'xj')^2$ 

        h;
        section1 = 0.5*(h_expr2(comb(h,1))*h_expr2(comb(h,2)))^2;

        h_expr = [h_expr; section1];

    end

    b =
    [2,3,4,5,1,3,4,5,1,2,4,5,1,2,3,5,1,2,3,4;1,1,1,1,2,2,2,2,3,3,3,3,4,4,4,4,5,5,
    5,5]; % matrix used for loop indexing to calculate all the combinations

    for m = 1:20 %creates a higher order term for the standard uncertainty
    (f''/xi')*(f''/xi*(f''/xj'))
        m;
        section2 = h_expr2(b(2,m))*(h_expr2(b(2,m))*h_expr3(b(1,m)));

        h_expr4 = [h_expr4; section2];

    end

    c = [1,1,2,2,3,3,4,4,5,5,6,6,7,7,8,8,9,9,10,10]; % used for adding the
    first section to the correct second sections

    for n = 1:20 % adds the partial functions together, multiplies it with
    the correct u(xi) and u(xj) values and sums them

        n;

        sections = (h_expr(c(n))+h_expr4(n))*ui(b(2,n))*ui(b(1,n));

        hhh = [hhh; sections]; % sum of uncertainties
    end
    %% Second order uncertainty components

    PartialUc = zeros(1,20);

    % the particular xi or xj can be deduced from the b matrix, first row is
    % j from xi[1:5] and second row is xi from xi[1:5] e.g. loop 17 (b(1,17)
    = 1 b(2,17) = 5) would be
    % Ap-a_0 connection

    for o = 1:20

        jjj = hhh(o);

        K = symfun(jjj,[a_0,W_,B_,T_,A_p]);

        PartialUc(o) = round(vpa((K(a0,W,B,T(k-Loopstart+1),Ap2))),5);

    end

```

```

    % sum(PartialUc); % reference value for the higher order variance
components
    %% Total uncerertainty summation
    uc_func2 = sum(hhh([1:20])); % summs all the 30 functions, dont open this
function or its length will crash matlab
    uc_func = sum(h_expr5([1:5]));
    %uc_funcs = simplify(uc_func); turn a 41 000 character function into a 70
000 character function with this simple trick

    x_x = symfun(uc_func2,[a_0,W_,B_,T_,A_p]); % higher order terms

    x_y = symfun(uc_func,[a_0,W_,B_,T_,A_p]); % fist order terms

    STD_uncertainty2 = 1*confLevel*((round(vpa((x_x(a0,W,B,T(k-
Loopstart+1),Ap2))),5)))^0.5 ;% inserts validation values into the function
to give an uncertainty estimate
    STD_uncertainty = 1*confLevel*((round(vpa((x_y(a0,W,B,T(k-
Loopstart+1),Ap2))),5)))^0.5 ;% linear uncertainty

    Uc2std = STD_uncertainty2+STD_uncertainty;% +- ST Devs
    %toc % timer stop
    std(k,1:1) = Uc2std;
    Partials(k,1:20) = PartialUc;
    FirstOrder(k,1:5) = FirstUc;
    fst(k,1:1) = STD_uncertainty;
    snd(k,1:1) = STD_uncertainty2;

    Bet = (1+(a0/b0)^2)^0.5-a0/b0;

    Ms(1,k) = (b0*ys)/J(k);
    Ms(2,k) = 1.455*Bet*b0*ys;
    Ms(3,k) = 1.072*Bet*b0*ys;

    %% ////////// PLOTS //////////
    %% ////////// GRAPH SETTINGS //////////
    %% ////////// MASTER CURVE CALCULATIONS //////////

    syms T0f(T0q) Kjc0f(T0q) Kjc0fmin(T0q) Kjc0fmax(T0q)% symbols used by the
sum functions

    T0ff = @(T0q) roo*(exp(0.019*(Tavg-T0q)))/(11+77*exp(0.019*(Tavg-T0q)));

    Kjc0ff = @(T0q) (((KjcT-20)^4*exp(0.019*(Tavg-
T0q)))/(11+77*exp(0.019*(Tavg-T0q)))^5);

    Kjc0ffmin = @(T0q) (((KjcT-20-std(k))^4*exp(0.019*(Tavg-
T0q)))/(11+77*exp(0.019*(Tavg-T0q)))^5);

    Kjc0ffmax = @(T0q) (((KjcT-20+std(k))^4*exp(0.019*(Tavg-
T0q)))/(11+77*exp(0.019*(Tavg-T0q)))^5);

    T0f(T0q) = T0ff;

    Kjc0f(T0q) = Kjc0ff;

    Kjc0fmin(T0q) = Kjc0ffmin;

```

```

    Kjc0fmax(T0q) = Kjc0ffmax;
%{
    h_exprs = [h_exprs; T0f(T0q)];

    h_exprs2 = [h_exprs2; Kjc0f(T0q)];

    h_exprs3 = [h_exprs3; Kjc0fmin(T0q)];

    h_exprs4 = [h_exprs4; Kjc0fmax(T0q)];
%}

end

%% Sum functins from ASTM E1921 (20)
T0f = sum(h_exprs(1:gg));

Kjc0f = sum(h_exprs2(1:gg));

Kjc0fmin = sum(h_exprs3(1:gg));

Kjc0fmax = sum(h_exprs4(1:gg));

Tq0 = round(vpasolve(T0f == (Kjc0f),T0q,[-200 T_est]),0); % Finds the highest
x that fits the [range]

Tq0min = round(vpasolve(T0f == (Kjc0fmin),T0q,[-200 T_est]),0);

Tq0max = round(vpasolve(T0f == (Kjc0fmax),T0q,[-200 T_est]),0);

mesUcT = 0; %abs(Tq0min-Tq0max)/2;
mesUcT2 = abs(Tq0min-Tq0max);

%% ////////// MASTER CURVE PLOTTING //////////

figure('name','Master Curve')

%Tq0 = round(Tq0+(BetaU/gg+mesUcT^2)^0.5,0);

Tq = num2str(double(Tq0)); %converts the T0 symbolic value to tex/16t
+round((BetaU/gg+mesUcT2^2)^0.5,0)
Tqmin = num2str(double(Tq0min)); %+round((BetaU/gg+mesUcT2^2)^0.5,0)
Tqmax = num2str(double(Tq0max));% +round((BetaU/gg+mesUcT2^2)^0.5,0)

CL = num2str(confLevel);
sigmap = strcat('+',CL,'\sigma: ','');
sigmam = strcat('-',CL,'\sigma: ','');
sigma = strcat(CL,'\sigma');
T0temp = {'T_0 [^oC]:', Tq} ;%,strcat([sigmam, ' ',
Tqmin]),Tq,strcat([sigmap, ' ', Tqmax])); % text for displayin the T0 in the
plot

Tx= T; %table2array(SETs(:, "Var1")); % Picks the temperatures from the excel
file, can also be done with T([1:length(SelectFile)])

scatter(Tx,MasterKjc,sz*2,col,"filled"); % Master curve datapoints
%title('HC Master Curve')

```

```

xlabel('Temperature [°C]');
ylabel('K_J_c [MPa\surdm]')
grid minor

Con = 0; %40*(-0.73+0.65*aw+1.76*aw^2-1.37*aw^3);
Txx = linspace(min(Tx)-50,-20,incr); % X axis values for the plot
Kjcmed = 30 + 70*exp(0.019*(Txx-((Tq0-Con)))); % Kjc med line values
Kjclow = 20 + (log(1/(1-confd)))^0.25 *(11+77*exp(0.019*(Txx-Tq0))); %Kjc
lower bound values
Kjchigh = 20 + (log(1/(confd)))^0.25 *(11+77*exp(0.019*(Txx-Tq0))); %Kjc
higher bound values
hold on;
%errorbar(Tx,MasterKjc,std(Loopstart:Loopend),'LineStyle','none');
%Kjc limit calculations for bend cases

ystr = 0.0093*Txx.^2-0.2023*Txx+474.67;

EEE=204-(Txx/16); %temperature adjusted Young's modulus

limKjc = (((EEE.*ystr)*b0)./(30*(1-v^2))).^0.5; %Kjc limit

hold on

plot(Txx,Kjcmed) % Master Curve
plot(Txx,Kjclow) % Master curve lower confidence limit
plot(Txx,Kjchigh) % Master curve higher confidence limit
%plot(Txx,limKjc) % Kjc limit line

legend('Datapoints','Median Master Curve','Lower Bound','Upper Bound','K_J_c
Limit line M = 30',Location='northwest') %graph legend

%text(-93,90,T0temp) %Text box location and contents (T0temp)max(limKjc)*0.75
vpa(Tq0*-1.25)

```

Appendix 3 Uncertainty variance components

TABLE- 1 First order uncertainty variance components

| First order σ^2 | | | | | |
|------------------------|------|------|------|------|---------|
| Sample | a0 | W | B | T | Ap |
| HC1 | 0,17 | 0,37 | 0,01 | 0,00 | 197,81 |
| HC2 | 0,05 | 0,05 | 0,00 | 0,00 | 298,68 |
| HC3 | 0,06 | 0,08 | 0,00 | 0,00 | 15,81 |
| HC4 | 0,15 | 0,09 | 0,00 | 0,00 | 17,53 |
| HC5 | 0,14 | 0,14 | 0,00 | 0,00 | 24,72 |
| HC6 | 0,05 | 0,12 | 0,00 | 0,00 | 23,91 |
| HC8 | 0,13 | 0,17 | 0,00 | 0,00 | 24,13 |
| HC9 | 0,09 | 0,10 | 0,00 | 0,00 | 26,22 |
| HC10 | 0,06 | 0,04 | 0,00 | 0,00 | 19,45 |
| HC11 | 0,15 | 0,14 | 0,00 | 0,00 | 21,99 |
| HC12 | 0,09 | 0,07 | 0,00 | 0,00 | 21,19 |
| LC1 | 0,22 | 0,63 | 0,00 | 0,00 | 1170,71 |
| LC2 | 0,68 | 0,66 | 0,00 | 0,00 | 692,64 |
| LC3 | 0,58 | 0,51 | 0,00 | 0,00 | 176,45 |
| LC4 | 0,20 | 0,18 | 0,00 | 0,00 | 33,00 |
| LC5 | 0,28 | 0,15 | 0,00 | 0,00 | 29,10 |
| LC6 | 0,08 | 0,13 | 0,00 | 0,00 | 27,30 |
| LC7 | 0,77 | 1,12 | 0,00 | 0,00 | 35,19 |
| LC8 | 0,75 | 0,64 | 0,00 | 0,00 | 31,53 |
| LC9 | 0,28 | 0,10 | 0,00 | 0,00 | 27,24 |
| LC10 | 0,10 | 0,06 | 0,00 | 0,00 | 28,00 |
| LC11 | 0,18 | 0,79 | 0,00 | 0,00 | 33,34 |

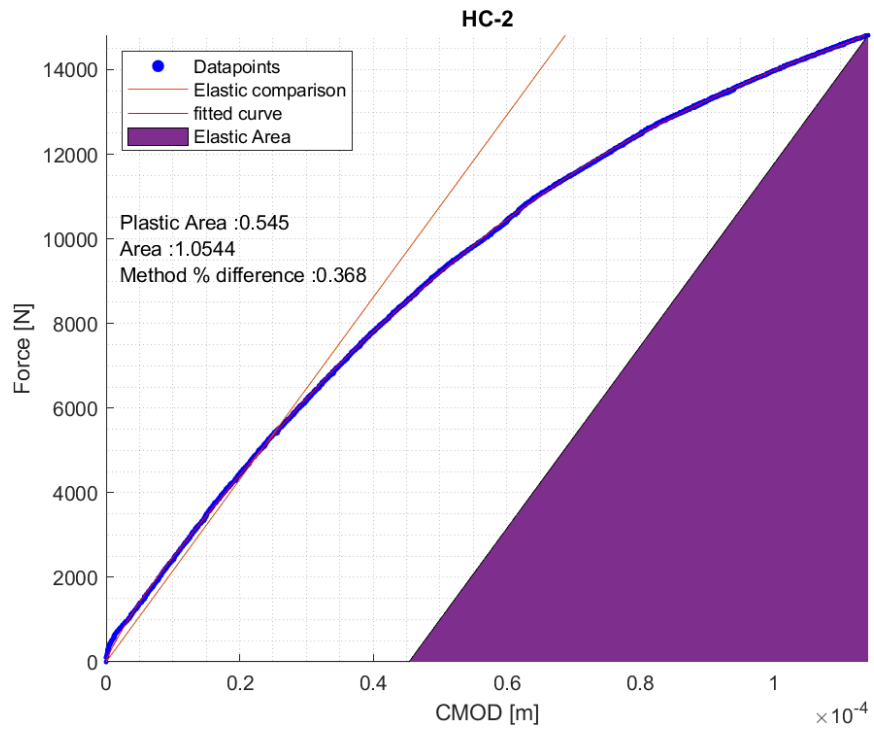
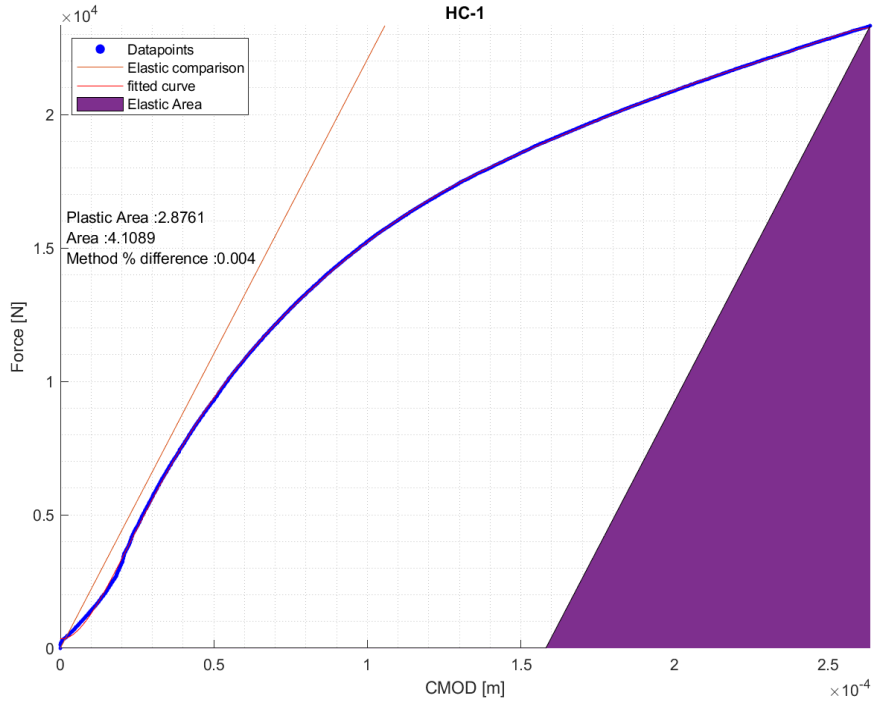
TABLE- 2 Second order uncertainty variance components

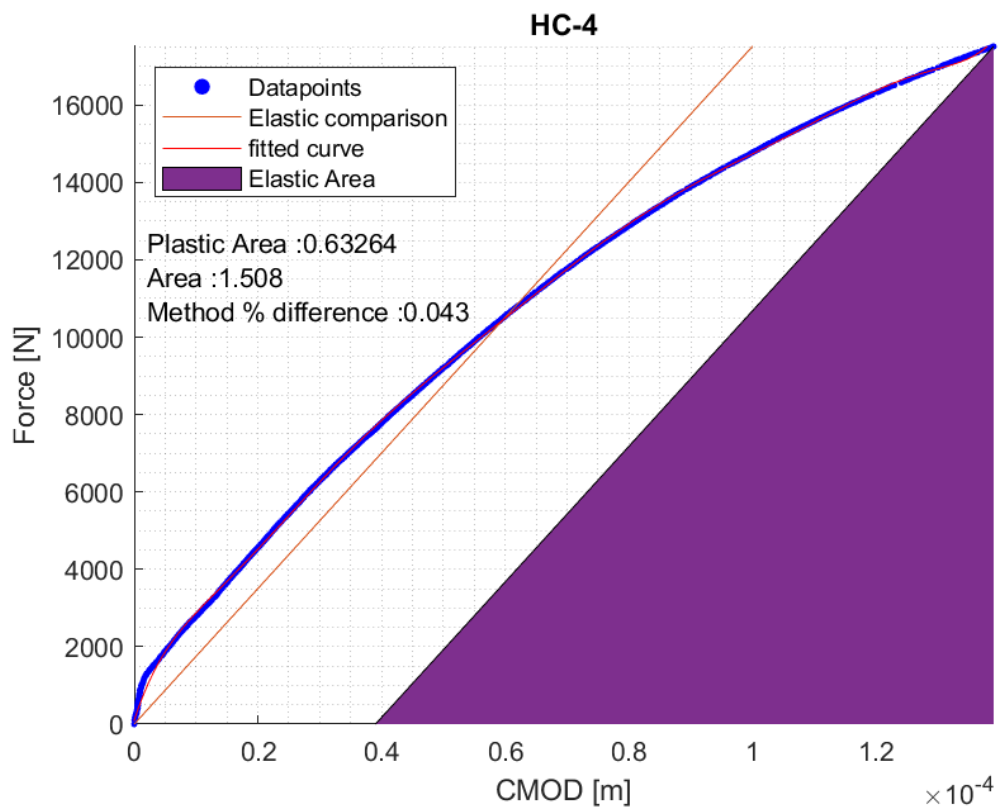
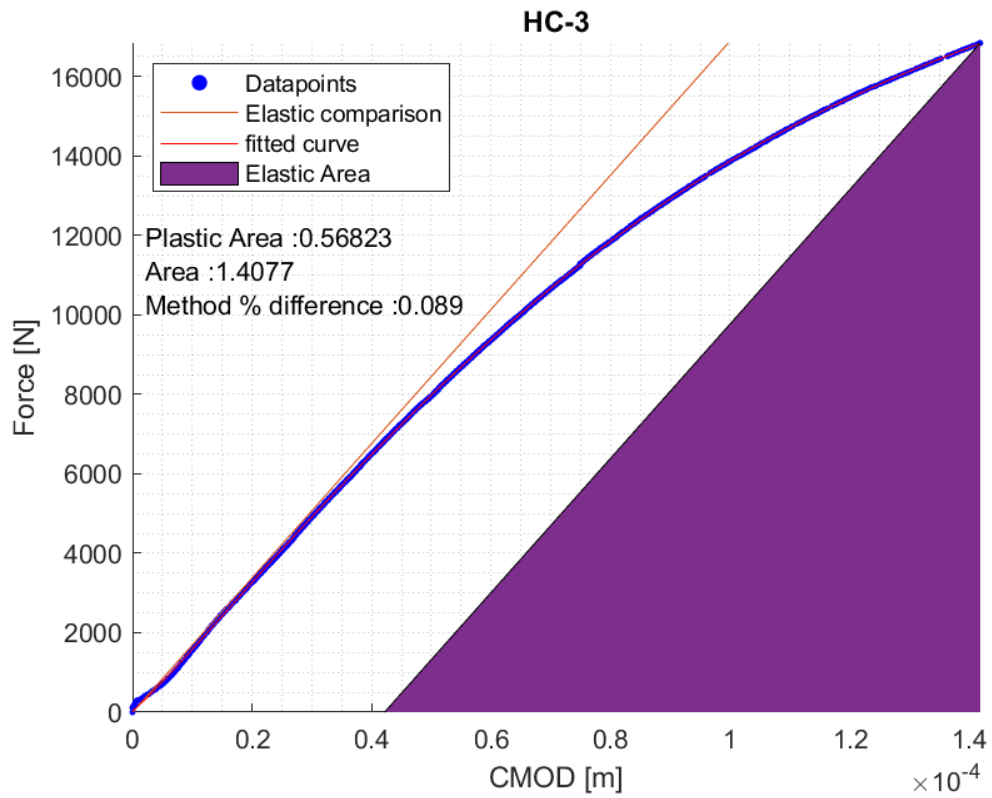
| Second order σ^2 | | | | | | | | | | | | | | | | | | | | |
|-------------------------|------|------|------|-------|------|------|------|--------|------|------|------|------|------|------|------|------|-------|------|------|------|
| | a0-W | a0-B | a0-T | a0-Ap | W-a0 | W-B | W-T | W-Ap | B-a0 | B-W | B-T | B-Ap | T-a0 | T-W | T-B | T-Ap | Ap-a0 | Ap-W | Ap-B | Ap-T |
| HC1 | 0,03 | 0,03 | 0,00 | 0,29 | 0,00 | 0,00 | 0,00 | 41,35 | 0,00 | 0,00 | 0,00 | 0,00 | 0,00 | 0,00 | 0,00 | 0,00 | 1,12 | 2,59 | 0,12 | 0,00 |
| HC2 | 0,00 | 0,00 | 0,00 | 0,03 | 0,00 | 0,00 | 0,00 | 10,23 | 0,00 | 0,00 | 0,00 | 0,00 | 0,00 | 0,00 | 0,00 | 0,00 | 1,33 | 1,42 | 0,08 | 0,00 |
| HC3 | 0,00 | 0,00 | 0,00 | 0,00 | 0,00 | 0,00 | 0,00 | 0,90 | 0,00 | 0,00 | 0,00 | 0,00 | 0,00 | 0,00 | 0,00 | 0,00 | 0,07 | 0,10 | 0,01 | 0,00 |
| HC4 | 0,01 | 0,01 | 0,00 | 0,01 | 0,00 | 0,00 | 0,00 | 1,15 | 0,00 | 0,00 | 0,00 | 0,00 | 0,00 | 0,00 | 0,00 | 0,00 | 0,17 | 0,12 | 0,01 | 0,00 |
| HC5 | 0,01 | 0,01 | 0,00 | 0,02 | 0,00 | 0,00 | 0,00 | 2,40 | 0,00 | 0,00 | 0,00 | 0,00 | 0,00 | 0,00 | 0,00 | 0,00 | 0,19 | 0,22 | 0,01 | 0,00 |
| HC6 | 0,00 | 0,00 | 0,00 | 0,01 | 0,00 | 0,00 | 0,00 | 2,27 | 0,00 | 0,00 | 0,00 | 0,00 | 0,00 | 0,00 | 0,00 | 0,00 | 0,07 | 0,21 | 0,01 | 0,00 |
| HC8 | 0,01 | 0,01 | 0,00 | 0,02 | 0,00 | 0,00 | 0,00 | 2,75 | 0,00 | 0,00 | 0,00 | 0,00 | 0,00 | 0,00 | 0,00 | 0,00 | 0,16 | 0,24 | 0,01 | 0,00 |
| HC9 | 0,00 | 0,00 | 0,00 | 0,01 | 0,00 | 0,00 | 0,00 | 1,95 | 0,00 | 0,00 | 0,00 | 0,00 | 0,00 | 0,00 | 0,00 | 0,00 | 0,14 | 0,20 | 0,01 | 0,00 |
| HC10 | 0,00 | 0,00 | 0,00 | 0,00 | 0,00 | 0,00 | 0,00 | 0,72 | 0,00 | 0,00 | 0,00 | 0,00 | 0,00 | 0,00 | 0,00 | 0,00 | 0,09 | 0,09 | 0,01 | 0,00 |
| HC11 | 0,01 | 0,01 | 0,00 | 0,02 | 0,00 | 0,00 | 0,00 | 2,15 | 0,00 | 0,00 | 0,00 | 0,00 | 0,00 | 0,00 | 0,00 | 0,00 | 0,18 | 0,20 | 0,01 | 0,00 |
| HC12 | 0,00 | 0,00 | 0,00 | 0,01 | 0,00 | 0,00 | 0,00 | 1,15 | 0,00 | 0,00 | 0,00 | 0,00 | 0,00 | 0,00 | 0,00 | 0,00 | 0,14 | 0,13 | 0,01 | 0,00 |
| LC1 | 0,07 | 0,07 | 0,00 | 1,24 | 0,00 | 0,00 | 0,00 | 454,05 | 0,00 | 0,00 | 0,00 | 0,00 | 0,00 | 0,00 | 0,00 | 0,00 | 3,20 | 9,64 | 0,38 | 0,00 |
| LC2 | 0,23 | 0,22 | 0,00 | 2,35 | 0,00 | 0,00 | 0,00 | 280,61 | 0,00 | 0,00 | 0,00 | 0,00 | 0,00 | 0,00 | 0,00 | 0,00 | 5,68 | 5,87 | 0,23 | 0,00 |
| LC3 | 0,15 | 0,15 | 0,00 | 0,53 | 0,00 | 0,00 | 0,00 | 59,30 | 0,00 | 0,00 | 0,00 | 0,00 | 0,00 | 0,00 | 0,00 | 0,00 | 1,47 | 1,38 | 0,06 | 0,00 |
| LC4 | 0,02 | 0,02 | 0,00 | 0,03 | 0,00 | 0,00 | 0,00 | 6,11 | 0,00 | 0,00 | 0,00 | 0,00 | 0,00 | 0,00 | 0,00 | 0,00 | 0,15 | 0,18 | 0,01 | 0,00 |
| LC5 | 0,02 | 0,02 | 0,00 | 0,04 | 0,00 | 0,00 | 0,01 | 4,49 | 0,00 | 0,00 | 0,00 | 0,00 | 0,00 | 0,01 | 0,00 | 0,00 | 0,22 | 0,15 | 0,01 | 0,00 |
| LC6 | 0,01 | 0,00 | 0,00 | 0,01 | 0,00 | 0,00 | 0,01 | 3,95 | 0,00 | 0,00 | 0,00 | 0,00 | 0,00 | 0,01 | 0,00 | 0,00 | 0,06 | 0,13 | 0,01 | 0,00 |
| LC7 | 0,44 | 0,43 | 0,00 | 0,20 | 0,01 | 0,00 | 0,01 | 22,26 | 0,00 | 0,00 | 0,00 | 0,00 | 0,01 | 0,01 | 0,00 | 0,00 | 0,28 | 0,41 | 0,01 | 0,00 |
| LC8 | 0,25 | 0,24 | 0,00 | 0,16 | 0,01 | 0,00 | 0,01 | 13,17 | 0,00 | 0,00 | 0,00 | 0,00 | 0,01 | 0,01 | 0,00 | 0,00 | 0,32 | 0,29 | 0,01 | 0,00 |
| LC9 | 0,01 | 0,01 | 0,00 | 0,04 | 0,00 | 0,00 | 0,00 | 3,48 | 0,00 | 0,00 | 0,00 | 0,00 | 0,00 | 0,00 | 0,00 | 0,00 | 0,26 | 0,13 | 0,01 | 0,00 |
| LC10 | 0,00 | 0,00 | 0,00 | 0,01 | 0,00 | 0,00 | 0,00 | 2,63 | 0,00 | 0,00 | 0,00 | 0,00 | 0,00 | 0,00 | 0,00 | 0,00 | 0,11 | 0,10 | 0,01 | 0,00 |
| LC11 | 0,07 | 0,07 | 0,00 | 0,04 | 0,00 | 0,00 | 0,01 | 15,99 | 0,00 | 0,00 | 0,00 | 0,00 | 0,00 | 0,01 | 0,00 | 0,00 | 0,07 | 0,32 | 0,01 | 0,00 |

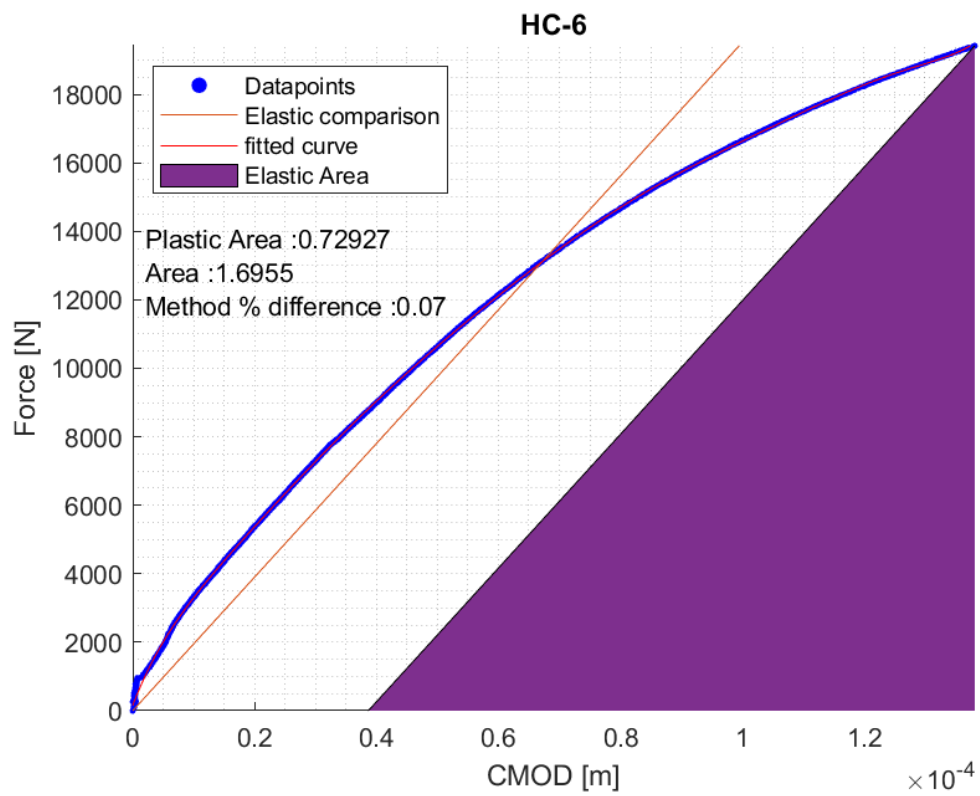
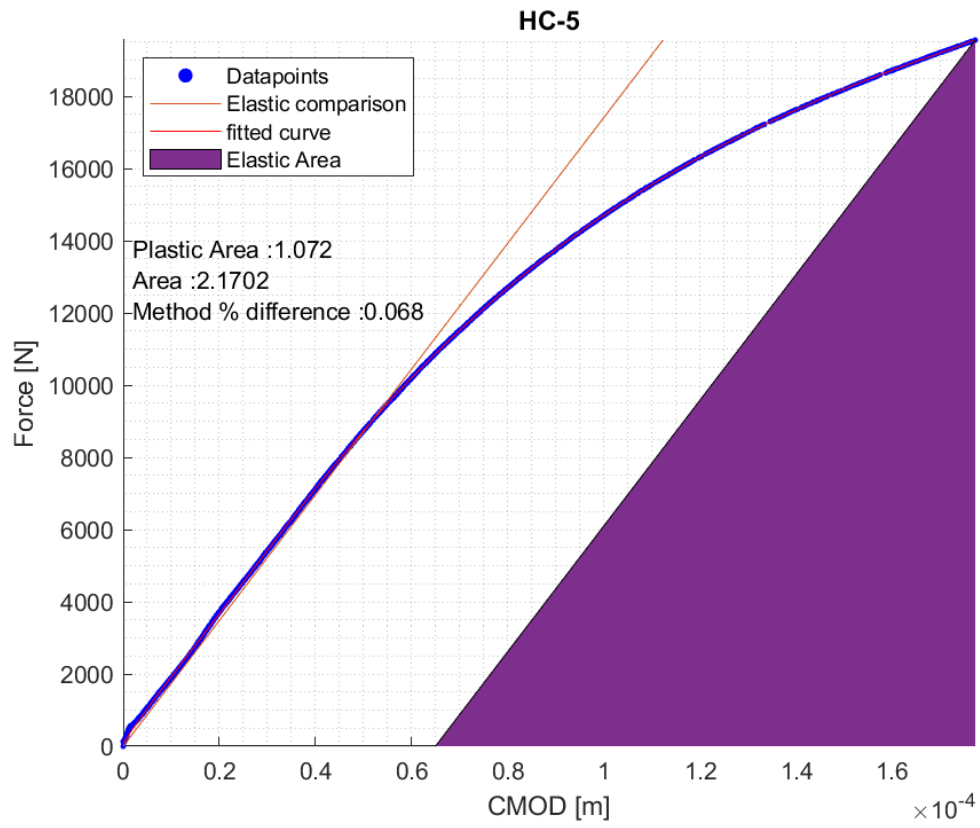
Appendix 4 Python script used for the sensitivity analysis

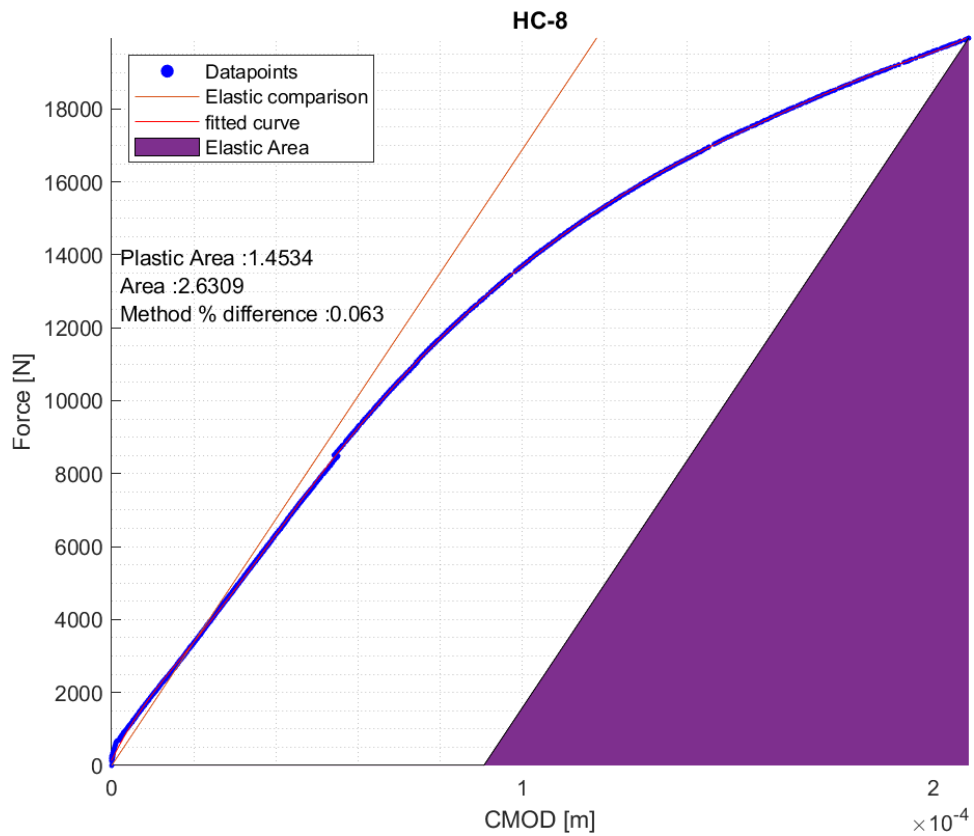
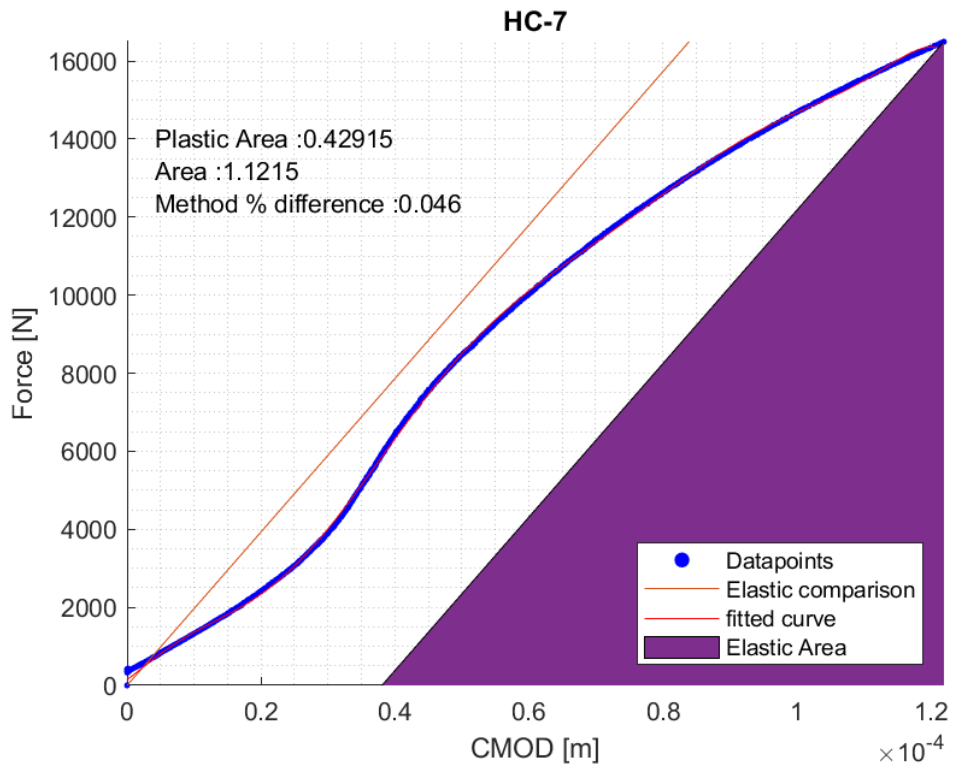
```
# Sensitivity analysis using Sobol's indices based on the work on SALib by (Inigawa, T., Herman.
J., & Usher. W., 2017-2022)
#Import modules and libraries
from cmath import sqrt
from re import T
from SALib.sample import saltelli
from SALib.analyze import sobol
from SALib.test_functions import Ishigami
import numpy as np
import time as tim
#timer
st = tim.time()
# Define the model inputs
problem = {
    'num_vars': 7, #number of variable parameters
    'names': ['a0','W','Ap','B','BN','P','degC'],# list of parameter names and ranges for each
parameter in sequential order
    'bounds': [[1.82, 6.02],
               [8.981, 10.989],
               [0.29,5.71],
               [8.981, 10.989],
               [7.35,9.328],
               [13333,53950],
               [-85,-84.15]]
}
# Generate samples
param_values = saltelli.sample(problem, 2**21) #problem size, powers of 2 recommended, conver-
gence is reached before negative values disappear
m = np.array(param_values)
n = np.hsplit(m,7)
#Define the fracture toughness function
def kjc_function(a0,W,Ap,B,BN,P,degC):
    eta = 1-1.089*(a0/W)+9.519*(a0/W)**2-48.572*(a0/W)**3+109.225*(a0/W)**4-73.116*(a0/W)**5-
77.984*(a0/W)**6+38.487*(a0/W)**7+101.401*(a0/W)**8+43.306*(a0/W)**9-110.770*(a0/W)**10
    f = 1.197-2.133*(a0/W)+23.886*(a0/W)**2-69.051*(a0/W)**3+100.462*(a0/W)**4-41.397*(a0/W)**5-
36.137*(a0/W)**6+51.215*(a0/W)**7-6.607*(a0/W)**8-
52.322*(a0/W)**9+18.574*(a0/W)**10+19.465*(a0/W)**11
    Kjcx = (((eta*(Ap))/(BN*(W-a0)))*1000
+((0.91*((P*(3.14159*a0)**0.5)/(W*((B*BN)**0.5))*f)**2)/((204-(degC/16))*1000))*((204-
(degC/16))/0.91)**0.5
    return Kjcx
Y = np.concatenate((kjc_function(n[0],n[1],n[2],n[3],n[4],n[5],n[6]),None)
print(Y, np.shape(Y),np.shape(param_values))
# Perform analysis
Si = sobol.analyze(problem, Y, print_to_console=True)
# Print the first-order sensitivity indices
print(Si['S1'],Si['ST'])
et = tim.time()
print((et-st)/60) #Prints runtime in minutes
```

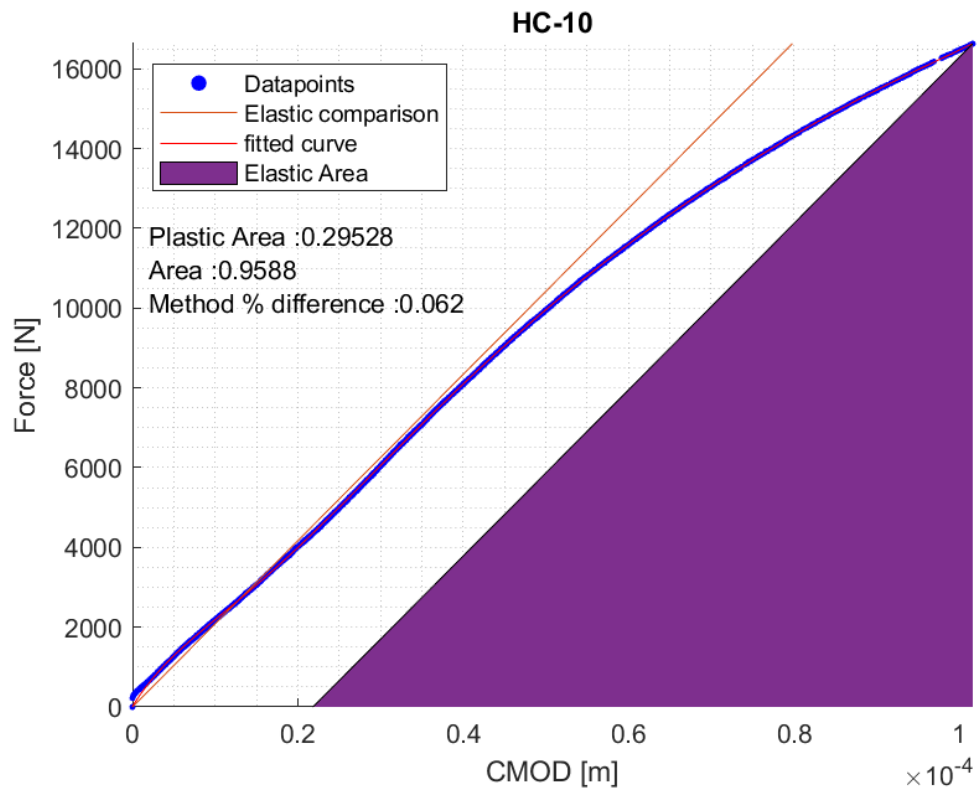
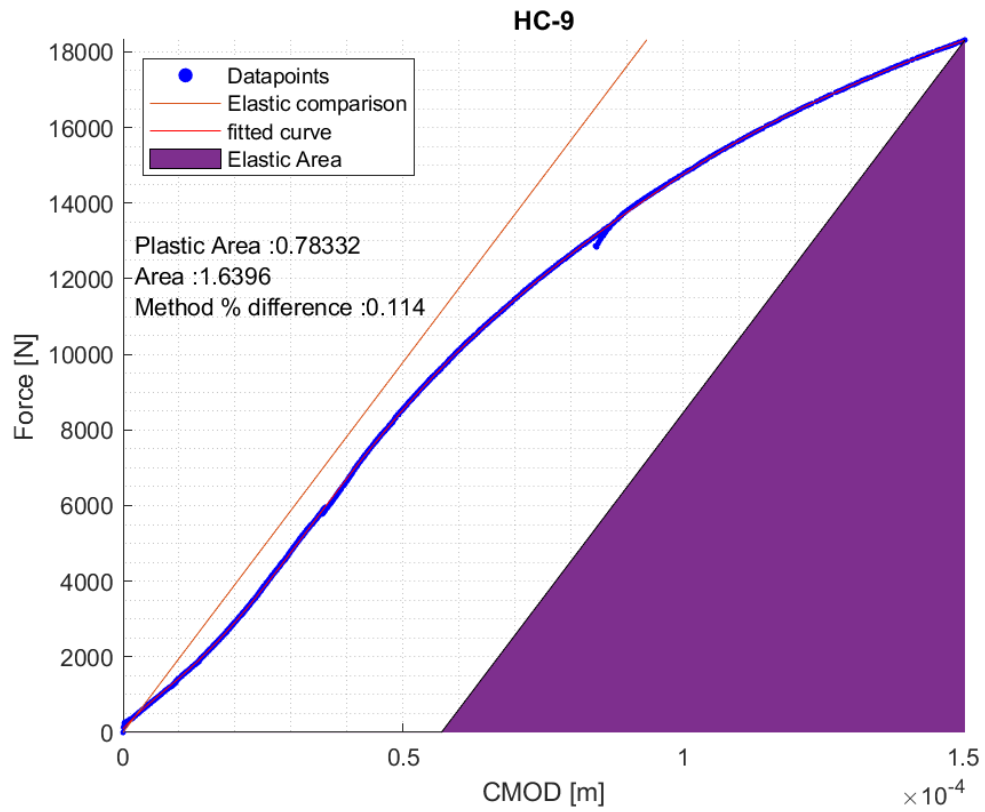
Appendix 5 CMOD-Force graphs for all the samples

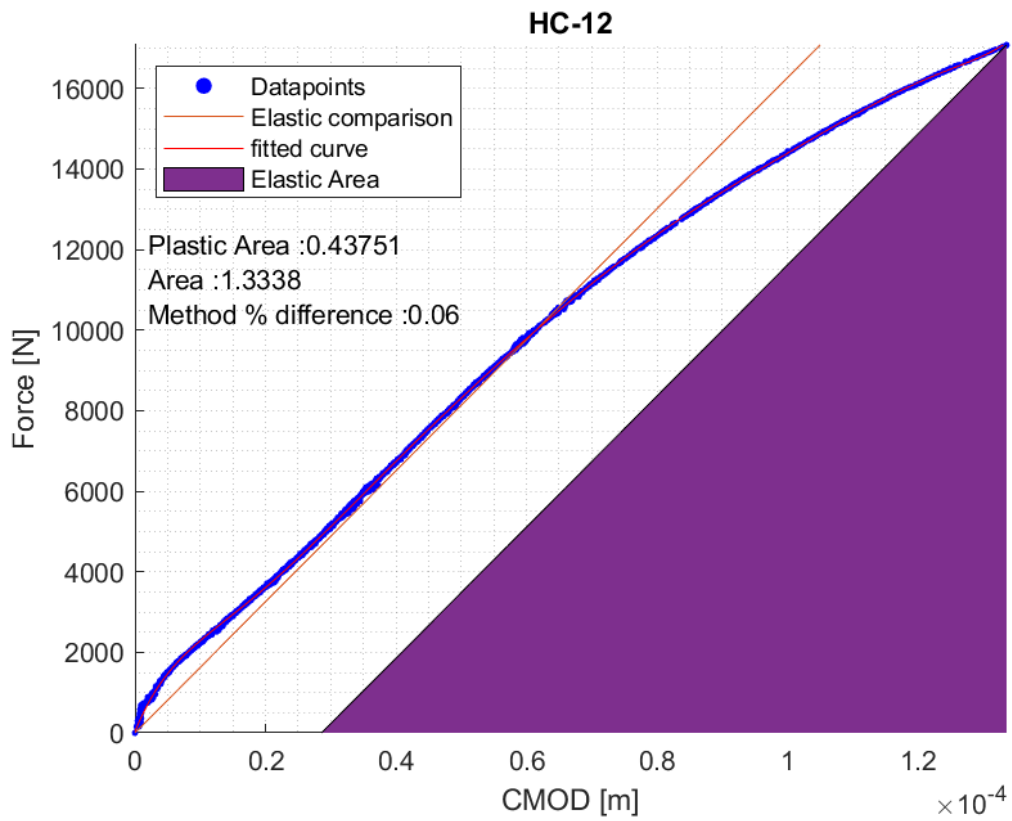
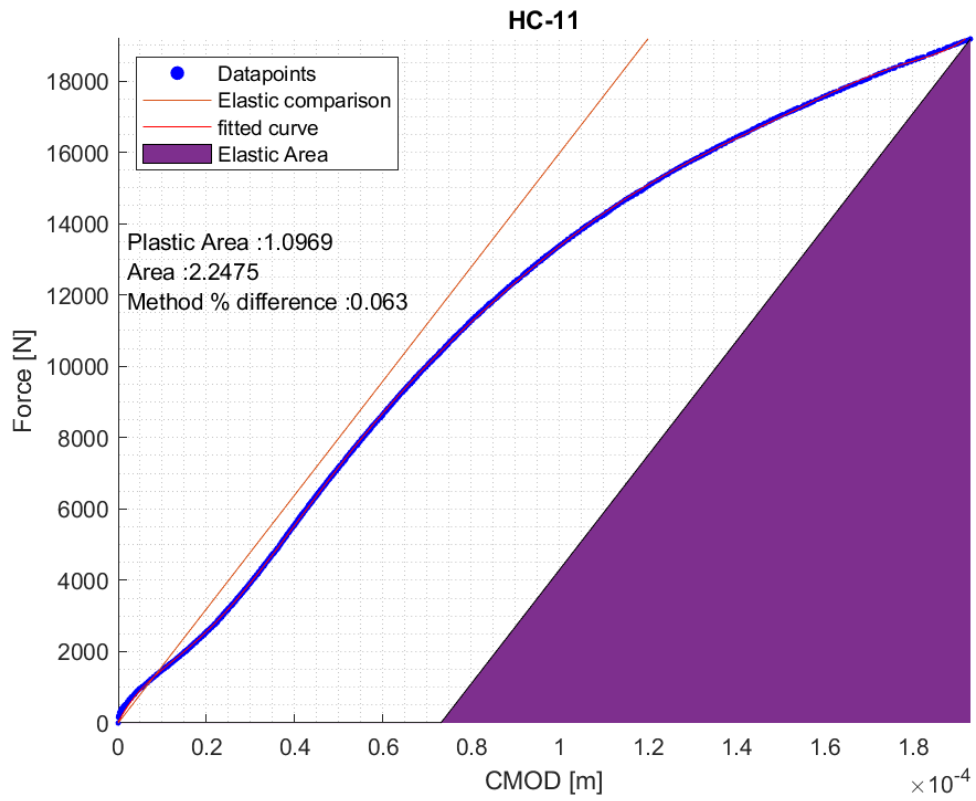


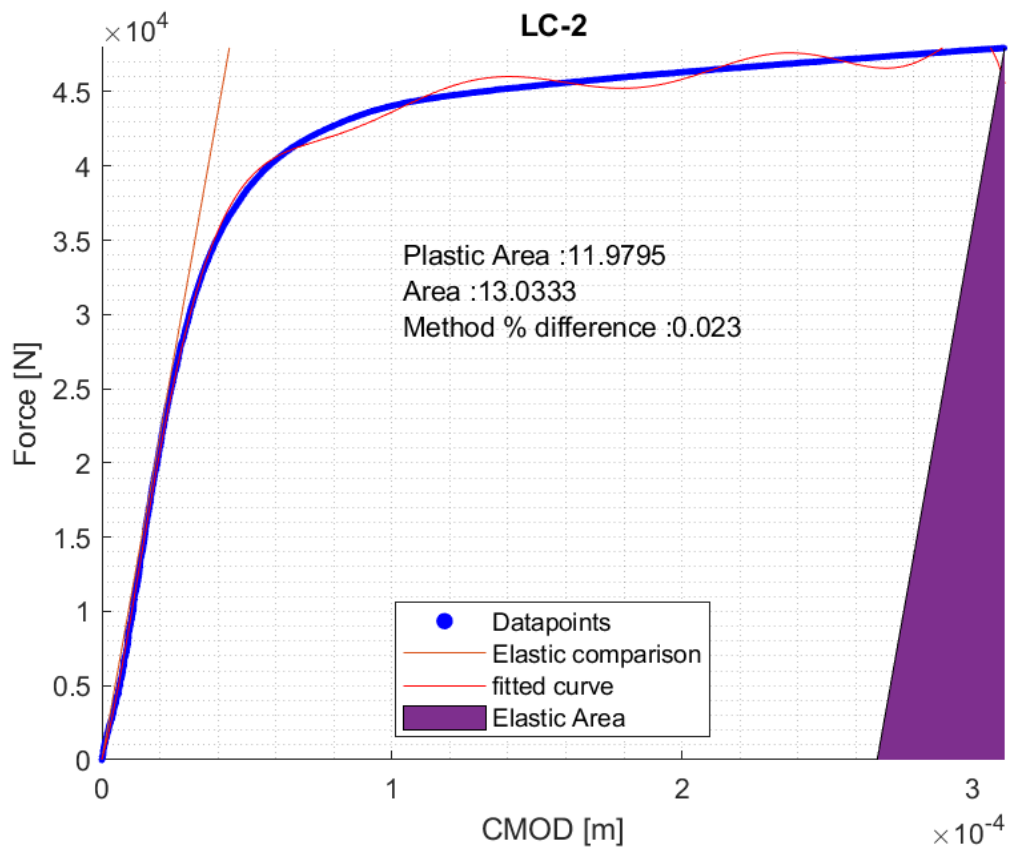
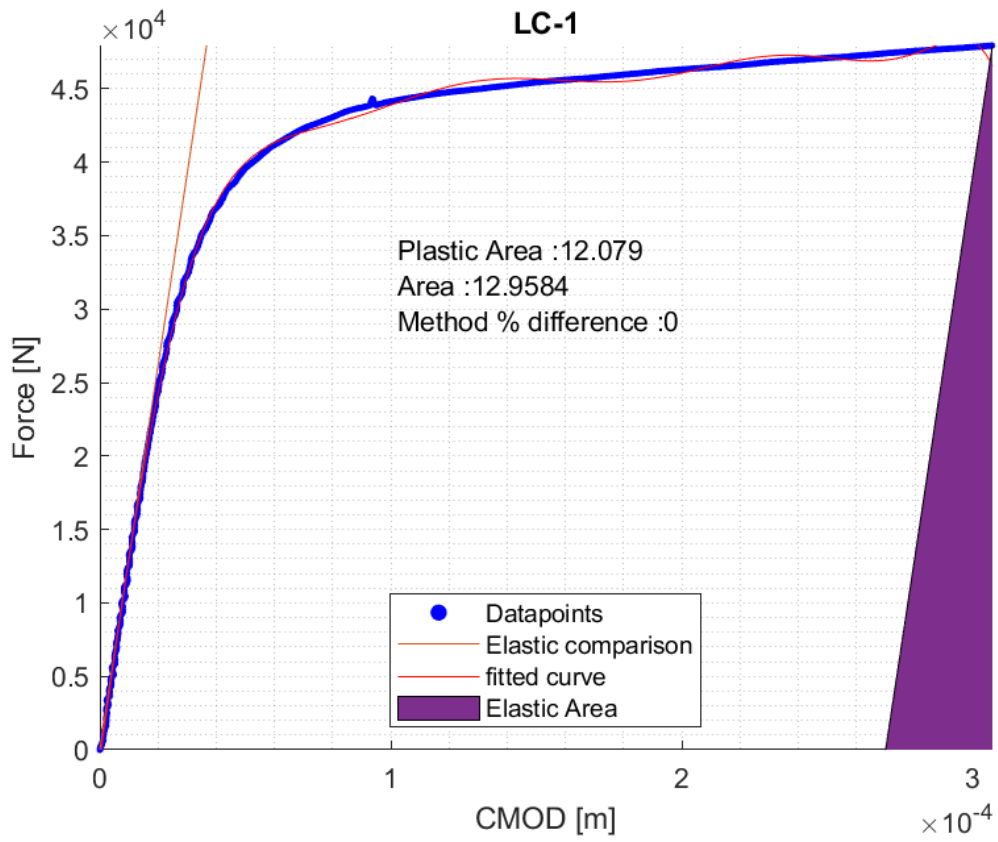


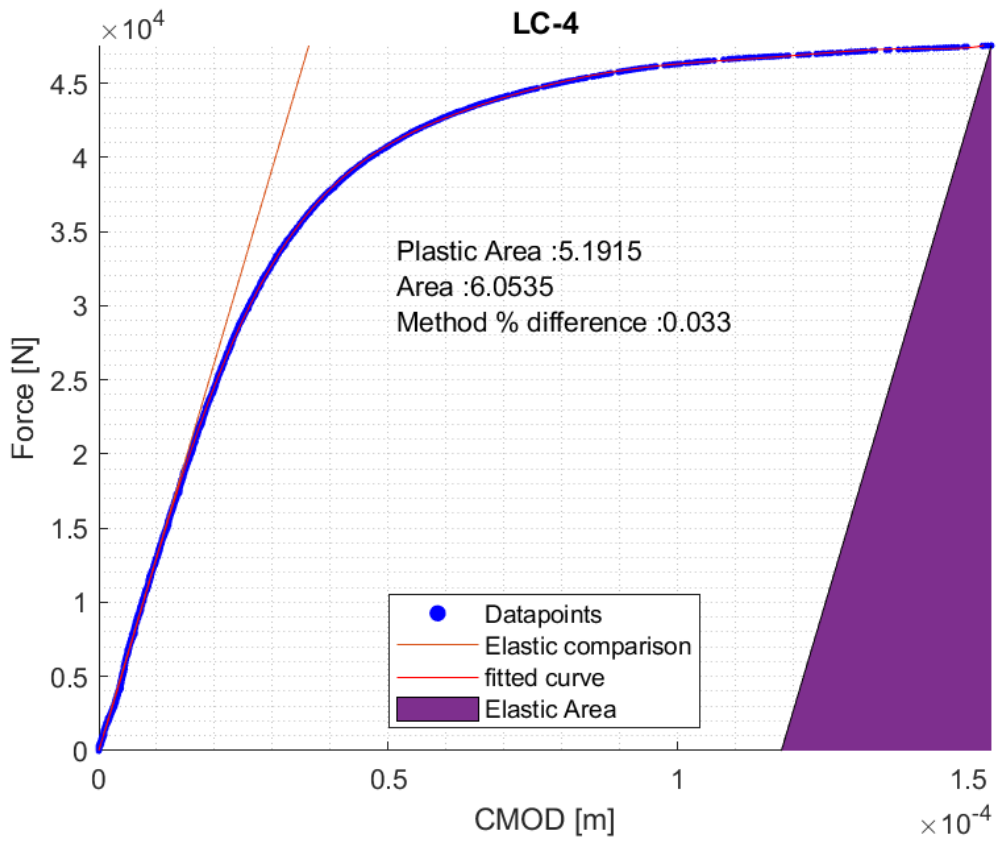
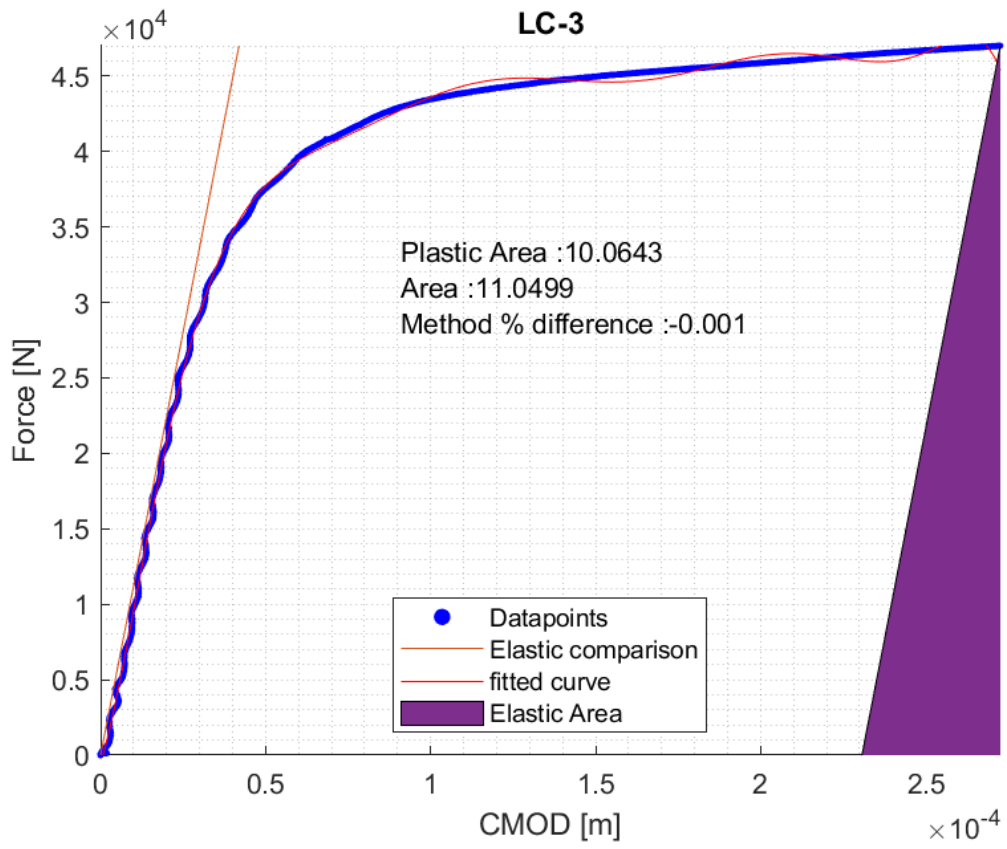


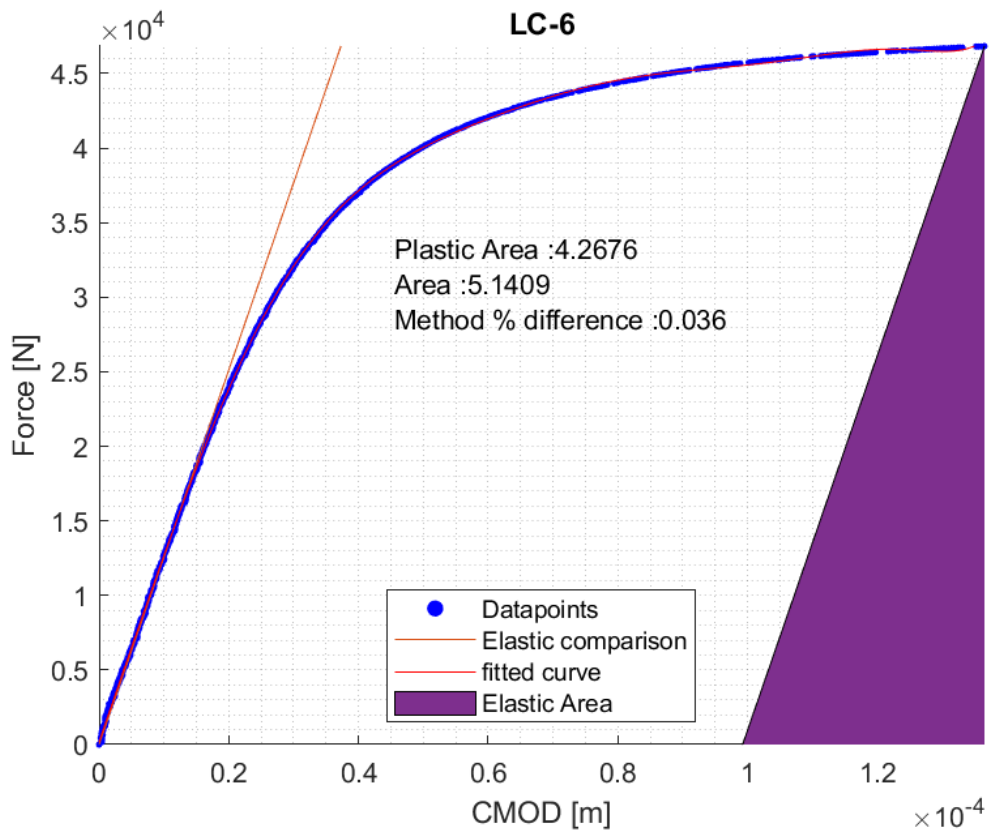
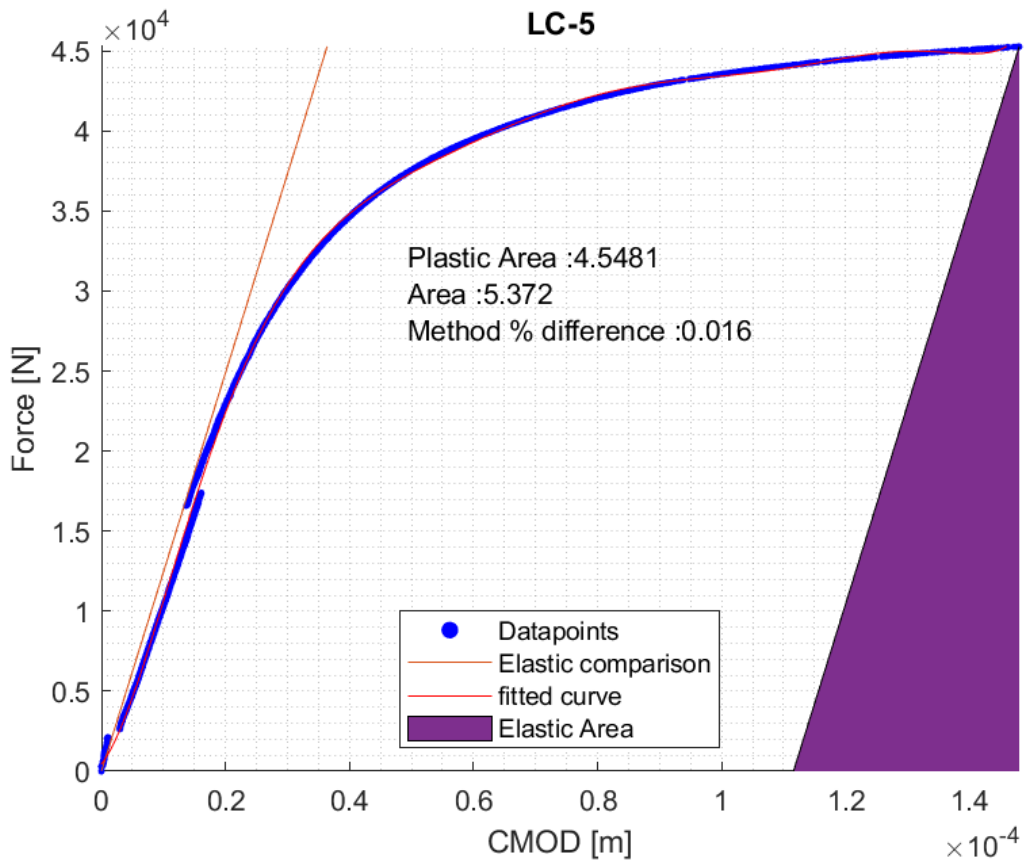


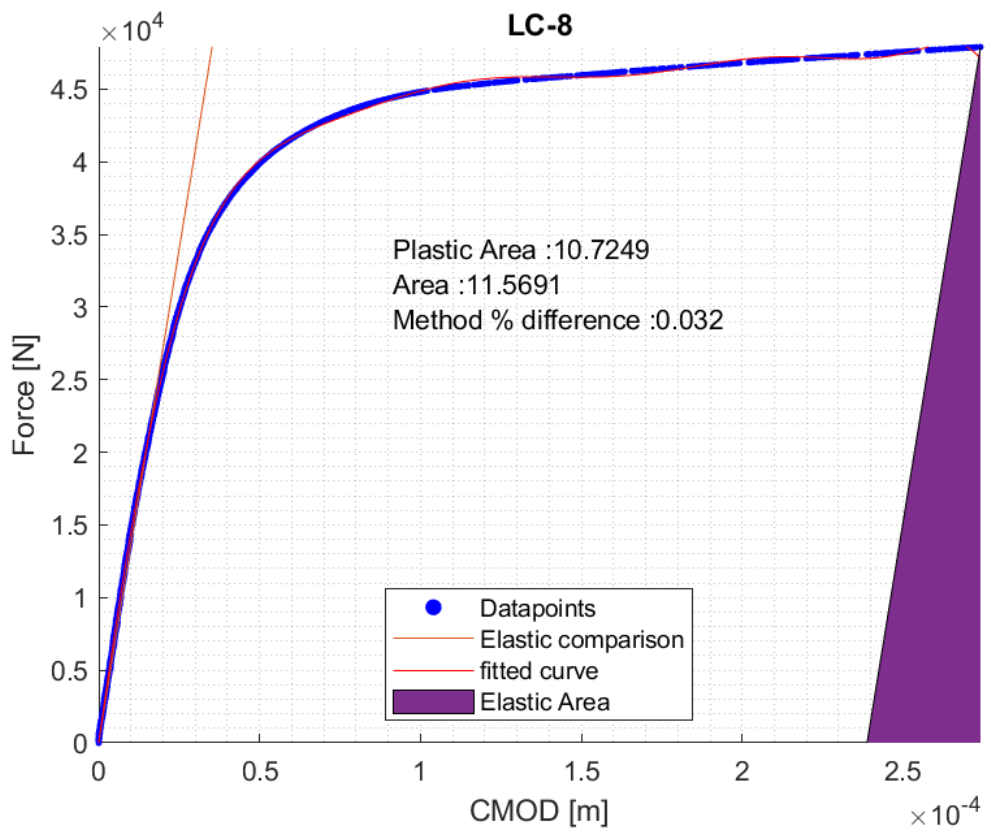
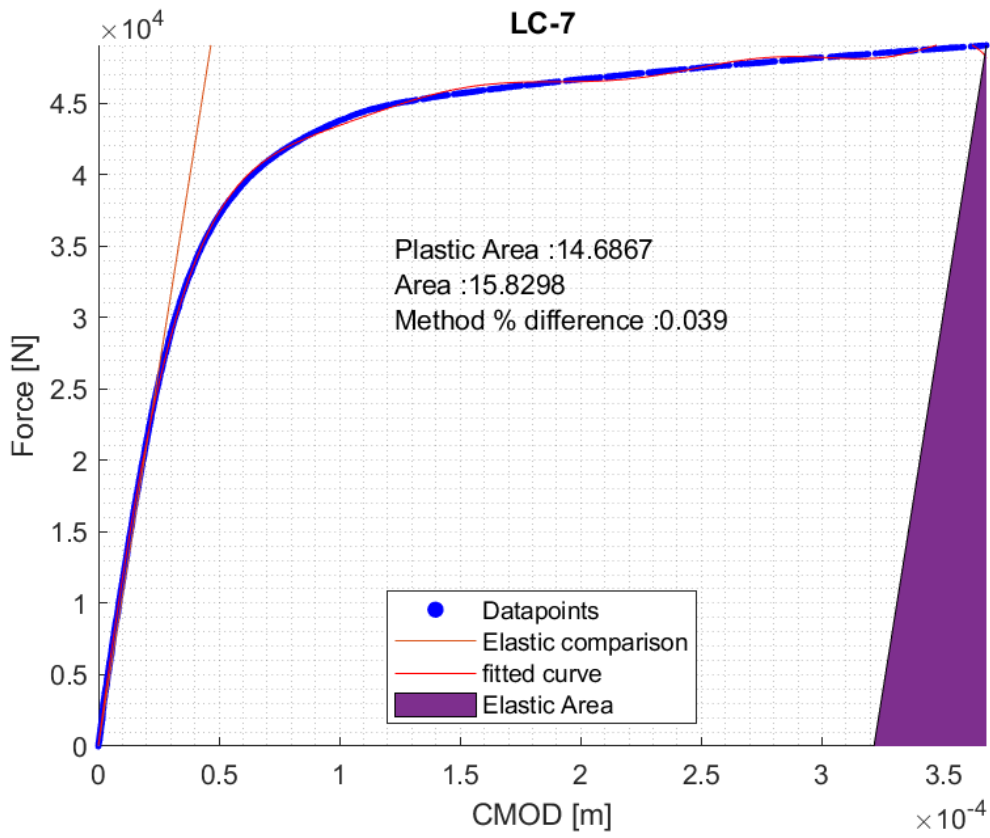


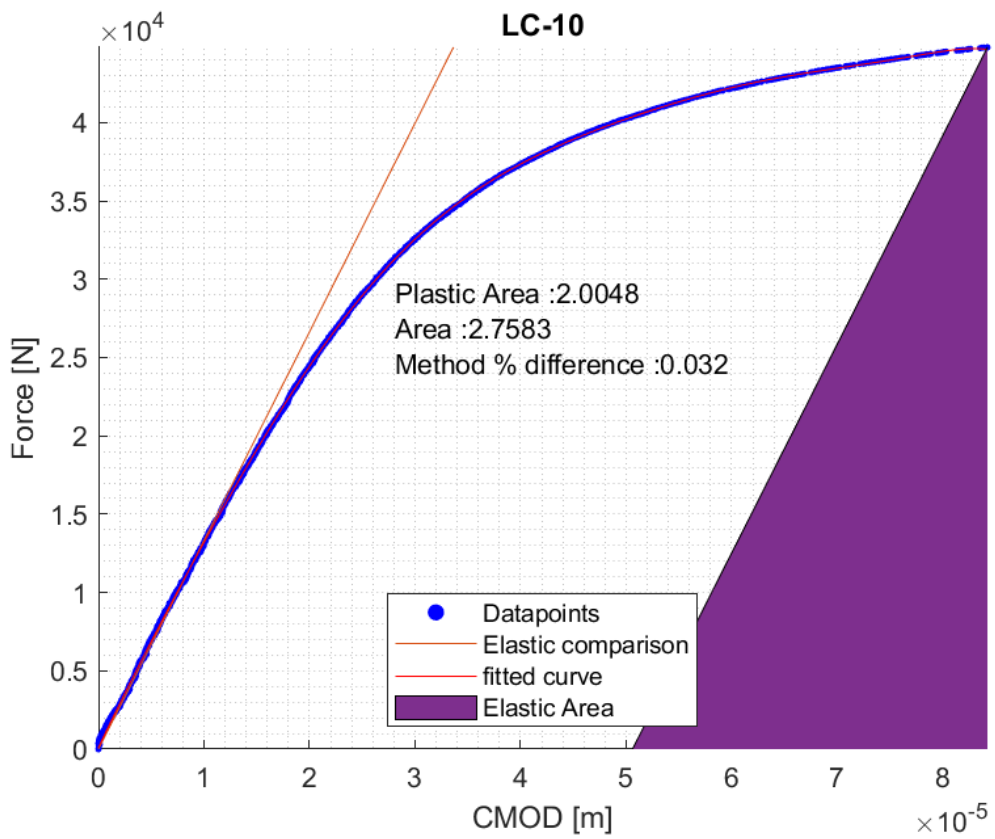
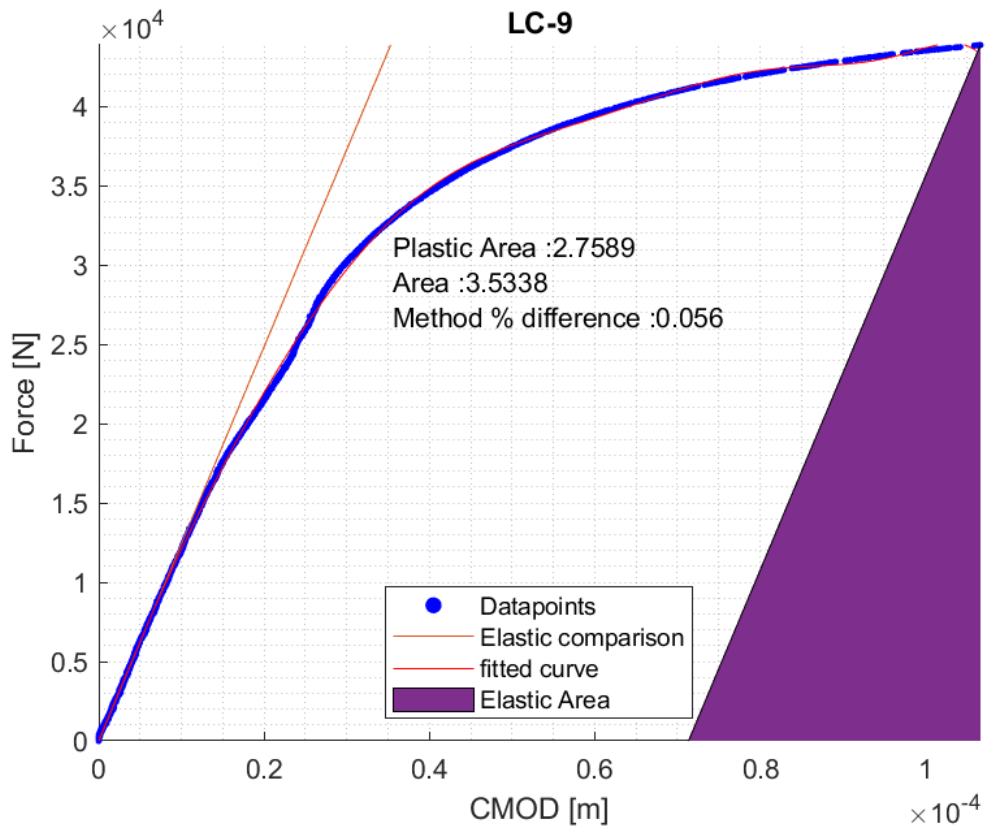


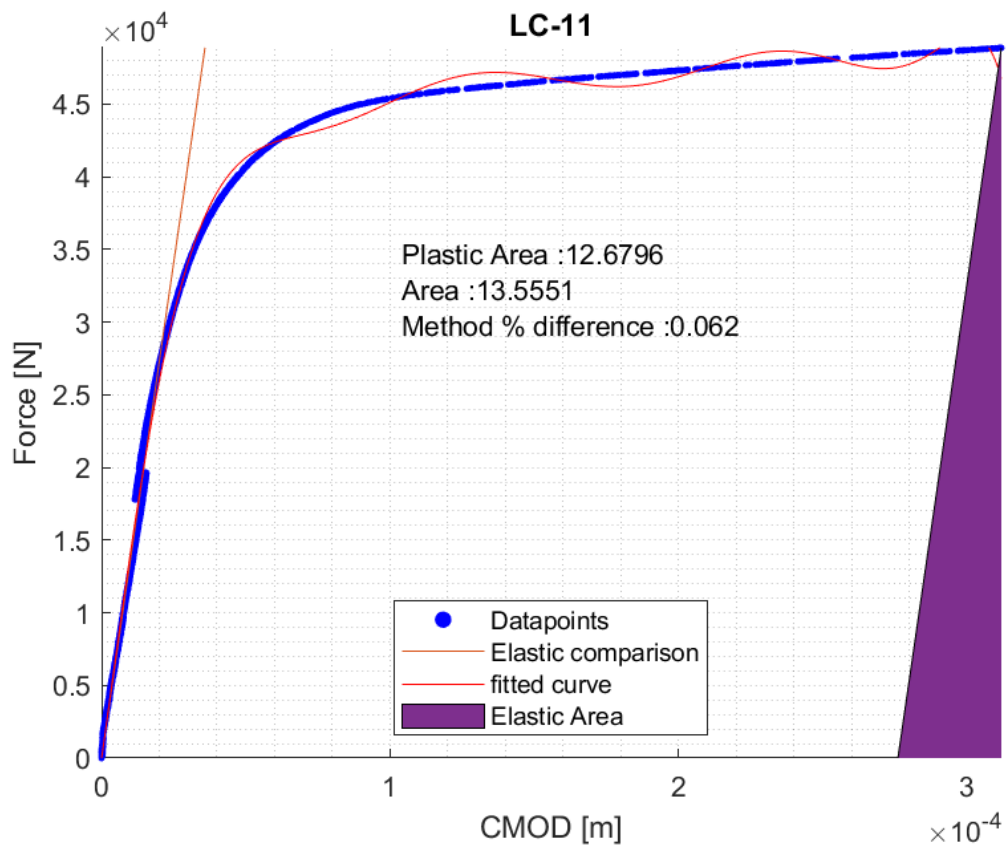












Appendix 6 Calculation values

Table 1. LC-Series Claculation values

| LEGEND | LC1 | LC2 | LC3 | LC4 | LC5 | LC6 | LC7 | LC8 | LC9 | LC10 | LC11 |
|---------------------------|--------|--------|--------|--------|--------|--------|--------|--------|--------|--------|--------|
| a ₀ est [mm] | 2,11 | 2,15 | 2,25 | 2,17 | 2,26 | 2,14 | 2,40 | 2,24 | 2,39 | 2,13 | 2,21 |
| a ₀ meas [mm] | 2,03 | 2,06 | 2,16 | 2,09 | 2,19 | 2,05 | 2,29 | 2,28 | 2,41 | 2,15 | 2,12 |
| E machine [GPa] | 200,83 | 164,83 | 179,90 | 201,84 | 204,60 | 186,93 | 186,08 | 238,59 | 236,10 | 216,24 | 200,54 |
| E [GPa] | 213,00 | 213,00 | 213,00 | 213,00 | 213,00 | 213,00 | 213,00 | 213,00 | 213,00 | 213,00 | 213,00 |
| E adjusted [GPa] | 213,00 | 175,06 | 191,64 | 213,00 | 213,00 | 199,50 | 199,50 | 231,96 | 231,96 | 213,00 | 213,00 |
| Cθ [N/m 10 ⁹] | 0,73 | 0,92 | 0,89 | 0,76 | 0,80 | 0,80 | 0,95 | 0,74 | 0,80 | 0,74 | 0,78 |
| Area [Nm] | 12,96 | 13,03 | 11,05 | 6,05 | 5,37 | 5,14 | 15,83 | 11,57 | 3,53 | 2,76 | 13,56 |
| Area Inc [Nm] | 12,96 | 13,03 | 11,05 | 6,05 | 5,37 | 5,14 | 15,82 | 11,57 | 3,53 | 2,76 | 13,55 |
| Ae [Nm] | 0,84 | 1,05 | 0,99 | 0,86 | 0,82 | 0,87 | 1,14 | 0,84 | 0,77 | 0,74 | 0,93 |
| Ap [Nm] | 12,12 | 11,98 | 10,06 | 5,19 | 4,55 | 4,27 | 14,69 | 10,72 | 2,76 | 2,02 | 12,62 |
| Jc | 179,21 | 180,32 | 154,57 | 86,77 | 76,59 | 71,27 | 230,44 | 170,91 | 54,65 | 41,07 | 191,35 |
| Jp | 166,11 | 166,68 | 140,57 | 73,00 | 63,30 | 58,59 | 213,10 | 154,58 | 39,75 | 28,34 | 176,57 |
| Je | 13,10 | 13,64 | 14,00 | 13,77 | 13,29 | 12,68 | 17,34 | 16,33 | 14,91 | 12,73 | 14,79 |
| Max Force [F] | 47950 | 47956 | 47001 | 47536 | 45272 | 46830 | 49041 | 47901 | 43886 | 44805 | 48872 |
| Stress [MPa] | 714,04 | 725,80 | 716,48 | 727,72 | 688,74 | 698,91 | 780,74 | 757,21 | 697,14 | 687,32 | 745,27 |
| Load Rate [MPaS-1] | 0,01 | 0,02 | 0,03 | 0,23 | 0,24 | 0,23 | 0,27 | 0,28 | 0,28 | 0,25 | 0,17 |
| T [°C] | -85,36 | -85,63 | -86,08 | -86,68 | -86,02 | -86,46 | -86,54 | -85,12 | -87,32 | -85,60 | -85,49 |
| Kjc [MPaVm] | 204,81 | 205,44 | 190,21 | 142,51 | 133,90 | 129,16 | 232,25 | 200,01 | 113,10 | 98,05 | 211,64 |
| Kjc 1T [MPaVm] | 166,28 | 166,81 | 154,77 | 117,00 | 110,17 | 106,42 | 188,06 | 162,52 | 93,73 | 81,80 | 171,76 |
| Q | 2,56 | 2,63 | 1,37 | -0,36 | -0,45 | -0,49 | 6,29 | 2,12 | -0,53 | -0,49 | 3,29 |
| T-stress | -0,54 | -0,53 | -0,52 | -0,53 | -0,52 | -0,53 | -0,50 | -0,51 | -0,49 | -0,52 | -0,53 |
| Q shift | 102,52 | 105,00 | 54,72 | -14,35 | -18,09 | -19,44 | 251,54 | 84,87 | -21,07 | -19,59 | 131,41 |
| T-Stess shift | -21,48 | -21,30 | -20,85 | -21,18 | -20,66 | -21,38 | -20,18 | -20,23 | -19,57 | -20,89 | -21,03 |
| a/W [mm] | 0,20 | 0,21 | 0,22 | 0,21 | 0,22 | 0,21 | 0,23 | 0,23 | 0,24 | 0,22 | 0,21 |
| Plasticity lim P-σ | 50 292 | 49 797 | 48 505 | 49 430 | 47 952 | 50 013 | 46 627 | 46 762 | 44 964 | 48 622 | 49 001 |
| Plasticity lim P-ε | 37 054 | 36 689 | 35 737 | 36 419 | 35 330 | 36 848 | 34 353 | 34 453 | 33 128 | 35 823 | 36 103 |
| M | 283,90 | 115,52 | 219,49 | 239,85 | 133,16 | 322,51 | 227,07 | 99,32 | 178,95 | 222,28 | 140,89 |
| η | 0,92 | 0,92 | 0,92 | 0,92 | 0,91 | 0,92 | 0,91 | 0,91 | 0,91 | 0,92 | 0,92 |
| Cθ [N/m 10 ⁹] | 0,73 | 0,92 | 0,89 | 0,76 | 0,80 | 0,80 | 0,95 | 0,74 | 0,80 | 0,74 | 0,78 |
| KI [MPaVm] | 1,33 | 1,33 | 1,35 | 1,34 | 1,36 | 1,33 | 1,38 | 1,38 | 1,41 | 1,35 | 1,34 |
| Ki 2 [MPaVm] | 1,37 | 1,38 | 1,40 | 1,39 | 1,41 | 1,38 | 1,44 | 1,44 | 1,47 | 1,40 | 1,40 |

Table 2. HC-Series Claculation values

| LEGEND | HC1 | HC2 | HC3 | HC4 | HC5 | HC6 | HC8 | HC9 | HC10 | HC11 | HC12 |
|---------------------------|--------|--------|--------|--------|--------|--------|--------|--------|--------|--------|--------|
| a ₀ est [mm] | 5,46 | 5,54 | 5,73 | 5,71 | 5,61 | 5,68 | 5,69 | 5,65 | 5,44 | 5,69 | 5,68 |
| a ₀ meas [mm] | 5,21 | 5,44 | 5,47 | 5,44 | 5,36 | 5,42 | 5,42 | 5,38 | 5,20 | 5,43 | 5,42 |
| E machine [GPa] | 184,34 | 202,08 | 161,39 | 165,01 | 157,00 | 181,46 | 135,19 | 179,07 | 179,17 | 148,63 | 150,37 |
| E [GPa] | 213,00 | 213,00 | 213,00 | 213,00 | 213,00 | 213,00 | 213,00 | 213,00 | 213,00 | 213,00 | 213,00 |
| E adjusted [GPa] | 209,78 | 213,00 | 184,08 | 189,72 | 178,62 | 207,68 | 155,17 | 205,60 | 203,55 | 169,86 | 171,58 |
| Cθ [N/m 10 ⁹] | 4,53 | 4,64 | 5,92 | 5,71 | 5,74 | 5,13 | 6,85 | 5,09 | 4,63 | 6,26 | 6,18 |
| Area [Nm] | 4,11 | 1,05 | 1,41 | 1,51 | 2,17 | 1,70 | 2,63 | 1,64 | 0,96 | 2,25 | 1,33 |
| Area Inc [Nm] | 4,11 | 1,05 | 1,41 | 1,51 | 2,17 | 1,69 | 2,63 | 1,64 | 0,96 | 2,25 | 1,33 |
| Ae [Nm] | 1,23 | 0,51 | 0,84 | 0,88 | 1,10 | 0,97 | 1,36 | 0,85 | 0,64 | 1,15 | 0,90 |
| Ap [Nm] | 2,88 | 0,55 | 0,57 | 0,63 | 1,07 | 0,73 | 1,27 | 0,79 | 0,32 | 1,10 | 0,43 |
| Jc | 77,66 | 21,39 | 25,41 | 27,66 | 38,34 | 32,69 | 43,35 | 31,21 | 18,03 | 39,00 | 22,77 |
| Jp | 53,53 | 10,27 | 10,74 | 11,99 | 19,94 | 13,76 | 23,64 | 14,76 | 5,91 | 20,60 | 8,17 |
| Je | 24,13 | 11,12 | 14,67 | 15,67 | 18,40 | 18,93 | 19,71 | 16,44 | 12,12 | 18,40 | 14,60 |
| Max Force [F] | 23329 | 14815 | 16843 | 17513 | 19556 | 19418 | 19942 | 18315 | 16628 | 19178 | 17075 |
| Stress [MPa] | 587,71 | 390,45 | 447,31 | 464,42 | 503,19 | 510,75 | 518,03 | 477,32 | 416,21 | 502,40 | 448,34 |
| Load Rate [MPaS-1] | 0,08 | 0,13 | 1,05 | 0,86 | 0,73 | 0,70 | 0,75 | 0,62 | 0,71 | 0,79 | 0,55 |
| T [°C] | -85,33 | -85,76 | -85,74 | -86,11 | -85,80 | -85,97 | -86,34 | -85,94 | -85,05 | -86,04 | -85,19 |
| Kjc [MPaVm] | 134,82 | 70,76 | 77,13 | 80,46 | 94,73 | 87,48 | 100,73 | 85,46 | 64,96 | 95,54 | 73,00 |
| Kjc 1T [MPaVm] | 110,90 | 60,18 | 65,22 | 67,86 | 79,16 | 73,42 | 83,91 | 71,84 | 55,60 | 79,82 | 61,96 |
| Q | -0,44 | -0,33 | -0,37 | -0,39 | -0,47 | -0,44 | -0,50 | -0,42 | -0,29 | -0,48 | -0,34 |
| T-stress | -0,11 | -0,08 | -0,07 | -0,07 | -0,09 | -0,08 | -0,08 | -0,08 | -0,11 | -0,08 | -0,08 |
| Q shift | -17,77 | -13,05 | -14,81 | -15,69 | -18,99 | -17,44 | -20,01 | -16,96 | -11,41 | -19,14 | -13,67 |
| T-Stress shift | -4,26 | -3,02 | -2,83 | -2,99 | -3,41 | -3,12 | -3,12 | -3,31 | -4,32 | -3,09 | -3,12 |
| a/W [mm] | 0,52 | 0,54 | 0,55 | 0,54 | 0,54 | 0,54 | 0,54 | 0,54 | 0,52 | 0,54 | 0,54 |
| Plasticity lim P-σ | 15 117 | 13 440 | 13 192 | 13 402 | 13 945 | 13 565 | 13 570 | 13 814 | 15 200 | 13 540 | 13 578 |
| Plasticity lim P-ε | 11 138 | 9 902 | 9 720 | 9 874 | 10 274 | 9 995 | 9 998 | 10 178 | 11 199 | 9 976 | 10 004 |
| M | 34,38 | 47,51 | 104,61 | 118,73 | 251,26 | 229,64 | 100,47 | 239,42 | 182,34 | 92,25 | 212,98 |
| η | 0,74 | 0,72 | 0,71 | 0,71 | 0,72 | 0,72 | 0,72 | 0,72 | 0,74 | 0,72 | 0,72 |
| Cθ [N/m 10 ⁹] | 4,53 | 4,64 | 5,92 | 5,71 | 5,74 | 5,13 | 6,85 | 5,09 | 4,63 | 6,26 | 6,18 |
| Ki [MPaVm] | 2,29 | 2,40 | 2,42 | 2,40 | 2,36 | 2,39 | 2,39 | 2,37 | 2,28 | 2,39 | 2,39 |
| Ki 2 [MPaVm] | 3,04 | 3,28 | 3,32 | 3,29 | 3,20 | 3,26 | 3,26 | 3,22 | 3,02 | 3,27 | 3,26 |